SUBWAVELENGTH IMAGING USING PLASMONIC LENSES AT TERAHERTZ FREQUENCIES

TANNER HEGGIE
Bachelor of Science, University of Lethbridge, 2012

A Thesis
Submitted to the School of Graduate Studies
of the University of Lethbridge
in Partial Fulfillment of the
Requirements for the Degree

MASTER OF SCIENCE

Department of Physics and Astronomy
University of Lethbridge
LETHBRIDGE, ALBERTA, CANADA

SUBWAVELENGTH IMAGING USING PLASMONIC LENSES AT TERAHERTZ FREQUENCIES

TANNER HEGGIE

Date of Defence: December 17, 2014

Dr. David A. Naylor Supervisor	Professor	Ph.D.
Dr. Adriana Predoi-Cross Thesis Examination Committee Member	Professor	Ph.D.
Dr. Locke D. Spencer Thesis Examination Committee Member	Assistant Professor	Ph.D.
Dr. Saurya Das Chair, Thesis Examination Committee	Professor	Ph.D.

Dedication

For my mother,

Per audacia ad astra.

Abstract

The effects of diffraction at terahertz frequencies limit the spatial resolution of imaging systems. One approach to achieve subwavelength resolution is near-field imaging using a subwavelength aperture, however, the low transmission through subwavelength apertures limits the sensitivity of this approach. Plasmonic lenses in the form of bullseye structures, consisting of a circular subwavelength aperture with concentric periodic corrugations, have demonstrated enhanced transmission and beam confinement. This thesis discusses the design criteria of plasmonic lenses optimized for 325 GHz. Fabrication for optical applications is traditionally achieved by nanolithography. Since the scale of plasmonic structures depends on the wavelength, precision micromilling techniques are well suited for terahertz applications. Theoretical simulations are obtained using a finite-difference time-domain solver and the performance the devices are evaluated using a customized terahertz testbed. The prospect of using plasmonic lenses in a terahertz imaging configuration for the diagnosis of cancer is also discussed.

Acknowledgments

I was first introduced to Dr. David Naylor in 2009 as I completed my second year as an undergraduate student at the University of Lethbridge. I have since worked many years under David's mentorship. His dedication to his work, intuition, and vast know-how has been an inspiration for me. I give credit to the research experience David has provided me for allowing me the opportunity to work with research groups outside of my hometown. When David presented me with the idea for this project, the synergy between theory, simulation, and experiment was irresistible. I am incredibly grateful for his feedback regarding all aspects of my education and work and I undoubtedly feel as though I have grown as a critical thinker.

I'd like to thank the remainder of my committee: including Dr. Locke Spencer for his interesting discussions and encouragement, and Dr. Adriana Predoi-Cross and Dr. David Siminovitch for their support throughout my undergraduate and graduate education.

Special thanks to Evgueni Bordatchev from NRC Automotive and Surface Transportation for micromachining my lenses with painstaking accuracy. Without a means for fabrication, I would not have been able to close the loop between experiment and theory.

The first thesis defence I attended was given by one of David's students. It was here that I first heard the group's unofficial motto: "It takes a family to raise a grad student." Thanks goes to Brad Gom, whose wise-words and IDL knowledge were of incredible help; Geoff Minors, who deciphered my schematics and machined many of the components for the terahertz testbed; Yuan Zhang for her initial bullseye simulations and advice; Matt Sherwood for his Linux support; Greg Tompkins for his support with electronics; Abenezer Fekade for aiding me with optical alignment; Vince Weiler for the bizarre bits-and-pieces

he brought from his home laboratory; and Grace Trimboli, who has been a colleague of mine for many years. Thanks also goes to Gibion Makiwa, whose work ethic and genuine personality I greatly admire. Sherif Abdelazim has become a dear friend throughout my project. I value the discussions we had regarding all aspects of life. His ability to create a light atmosphere, despite the occasional misery we may feel, is to be desired. I must also thank Dylan DeGrâce, who helped with my literature search and initial simulation methodology, as well as Hugh Ramp and Ian Veenendaal. Our memorable evenings in the office were of much moral support.

This project has received support from CMC Microsystems, the Natural Sciences and Engineering Research Council of Canada, and Alberta Innovates Technology Futures. Hardware and software support for this project was provided by Blue Sky Spectroscopy. Particular thanks goes to Sudhakar Gunuganti for his help with the optical design of the terahertz testbed and control software.

Surviving graduate school requires more than academic support. I have been lucky to have the encouragement of my friends throughout my degree. I would like to thank Chris Schultz, Derek Stevenson, Leslie Ohene-Adjei, Dustin Linnington, and all of those who have been a part of 510 for maintaining my sanity with a healthy dose of relaxation. Thank you to Darcy Best for your unwavering friendship, stimulating conversations, enormous LaTeX support, and countless hours of proof reading. As well, I would be amiss to not mention John, who always reminds me to "finish the fight."

Special thanks must be given to my supportive family, particularly my mother. She calls in the troops whenever it is needed. Her strength, commitment, and kindness has shaped who I am today.

Contents

List of Tables

List of Figures

Chapter 1

Introduction and Motivation

Terahertz (THz) radiation lies in the gap between microwaves and the near-infrared that includes frequencies from 300 GHz to 10 THz (wavelengths from 30 μm to 1 mm) [7]. This relatively unexamined region, historically made difficult by inefficient generation and detection of THz waves, has become increasingly accessible in recent years due to significant technological advances. Spectroscopic information in the THz band is relatively unexplored and the potential exists for spectral signatures of molecules to be used for the early detection of diseases [8]. Notably, THz radiation has been shown to have an increased ability to differentiate between cancerous and normal tissue [9]. Additional applications of THz radiation have been suggested, such as using their ability to penetrate through clothing to identify concealed explosives or gather spectroscopic information from polymers and semiconductors [7, 10].

Biomedical applications of THz imaging have gained interest due to the low photon energy of THz radiation, about 4 meV at 1 THz, which is below the minimum 13.6 eV required to ionize a hydrogen atom [11]. This is uniquely advantageous when compared to X-rays, which have photon energies six orders of magnitude higher [8]. Despite the promising applications of THz imaging, the material to be analyzed is often smaller than the incident wavelength. Lord Rayleigh's criterion (Section 1.1) restricts the spatial resolution of conventional far-field microscopy to be on the scale of the wavelength, which for THz frequencies is on the order of several hundred microns [6]. Near-field imaging techniques can improve matters by introducing a subwavelength aperture as an intermediate

optical element (Section 1.2), but this method is limited by very low transmission through the aperture. However, recent advances in the field of plasmonics have allowed for extraordinary transmission that would otherwise not be possible (Section 1.3). The design and implementation of a near-field THz imaging configuration that makes use of extraordinary transmission provides a path for the inspection of biological samples and may prove as a useful tool for the diagnosis of breast cancer (Section 1.4).

1.1 Spatial Resolution and the Limit of Classical Optics

Far-field imaging configuration such as simple and compound microscopes have a spatial resolution that is limited by Fraunhofer diffraction (with the exception of any abberations caused by imperfect lenses) [6]. Consider the setup shown in Figure 1.1(a). Light of wavelength λ is emitted from a distant source and incident on an opaque obstruction, Σ, with a circular aperture of radius r. A viewing screen, σ, is placed a distance L away from the obstruction.

In the far-field case ($L > r^2/\lambda$), light travelling through the circular aperture diffracts in a pattern with a central bright spot surrounded by alternating dark and light rings, as shown in Figure 1.1(b) [6]. This intensity distribution, known as the *Airy pattern*, is given by [12]:

$$I = I_0 \left[\frac{2J_1(krq/L)}{krq/L} \right]^2, \qquad (\mathrm{W \cdot m^{-2}}) \quad (1.1)$$

where I_0 is maximum intensity located at the centre of the pattern, J_1 is the Bessel function of the first kind of order one, $k = 2\pi/\lambda$ is the wavenumber, and q is the radial distance to a point on the screen.

The location of the first dark ring is given by the first zero of the Bessel function, $krq/L = 3.83$, such that

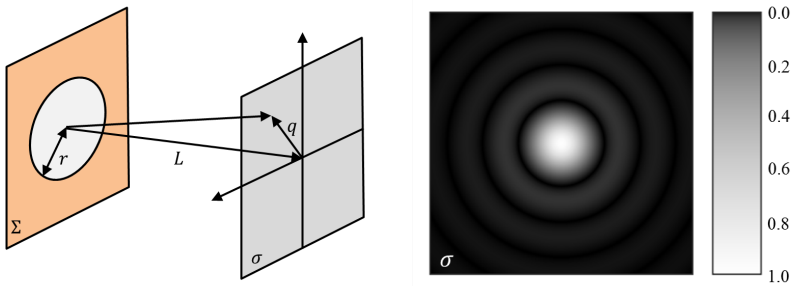

(a) (b)

Figure 1.1: (a) An opaque obstruction with a circular aperture of radius r is placed far from a source (not shown) and at a distance L from a viewing screen. (b) In the far-field case, the intensity distribution on the viewing screen is known as the Airy pattern [2].

$$q = 1.22\left(\frac{L\lambda}{d}\right), \tag{1.2}$$

where d is the diameter of the aperture.

In the case of imaging systems, the diameter of the lens is typically the diffracting aperture. When the viewing screen is placed a focal length f away, Equation 1.2 becomes

$$q = 1.22\lambda\left(\frac{f}{d}\right). \tag{1.3}$$

The ratio f/d is typically written as f/N, where N is known as the *f-number* of the lens.

The resolution of the an imaging system can be quantified by the Rayleigh criterion, which states that two incoherent point sources can be distinguished if the centre of one of their Airy patterns coincide with the first minimum of the other Airy pattern [6]. That is, the minimum resolved distance, δl_{min}, is

$$\delta l_{min} = 1.22\lambda(f/N). \tag{1.4}$$

The wavelength of light and the f-number of the optics thus limits the obtainable resolution of the imaging system, which for conventional optics is at best $\approx \lambda/2$ [6].

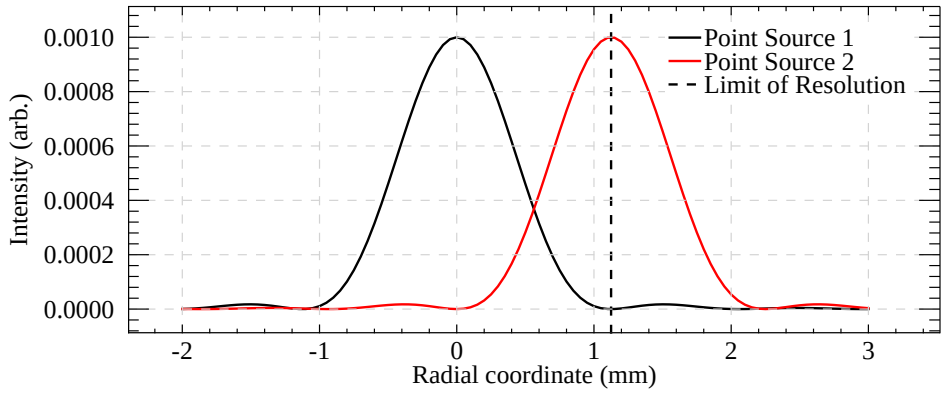

Figure 1.2: The limit of resolution is defined by the Rayleigh criterion as the point where the centre of an Airy pattern produced by one point source (red) falls on the minimum of a second Airy pattern produced by another point source (black). These curves were generated for $\lambda = 922$ µm and an $f/1$ lens, giving $\delta l_{min} \approx 1120$ µm (dashed line).

To illustrate the Rayleigh criterion, the Airy pattern of two point sources was generated for the case of $\lambda = 922$ µm illumination on an $f/1$ lens (Figure 1.2). The motivation behind these example parameters will be explored shortly, but suffice it to say that the minimum resolvable distance for this combination is approximately 1120 µm, that is, on the order of the wavelength.

1.2 Near-Field Aperture Techniques

One method to improve the spatial resolution of conventional optics is to use a subwavelength aperture to reduce the size of the source/detecting element [13]. Since the distribution of radiation intensity immediately behind a subwavelength aperture is determined by the size of the aperture rather than the wavelength, the spatial resolution of such a system is then defined by the aperture size. A schematic of a typical near-field imaging configuration is shown in Figure 1.3 [13–15]. Light is incident on a subwavelength aperture (often a tapered metal waveguide with a subwavelength exit aperture) and a sample is placed within a wavelength of the output side. The sample is scanned in a raster motion and the transmitted radiation is collected by subsequent optics and picked up by a detecting

element. This technique, initially developed for visible frequencies, is known as *near-field optical microscopy* (NSOM) [14].

At THz frequencies, initial attempts at near-field imaging using subwavelength apertures were limited by poor transmission through the hole, scaling as r^6/λ^4, where r is the radius of the aperture and λ the wavelength of light [16]. The thickness of the aperture further decreases the transmitted power with an exponential dependence. These limitations are further explored in Chapter 4. Since commonly available room temperature sources are of relatively low power, the utility of THz subwavelength imaging becomes limited.

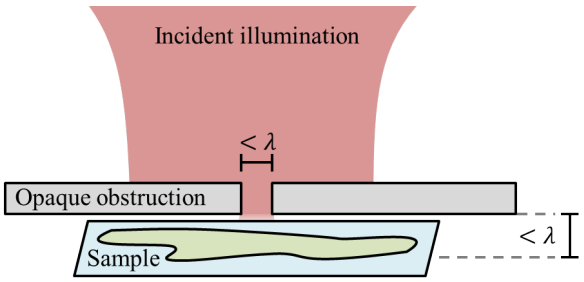

Figure 1.3: The typical setup of a near-field scanning microscope. Light is incident on a sample from a subwavelength aperture and scanned in the horizontal plane. The resolution of the image is determined by the aperture diameter.

1.3 Plasmonics: A Route to Enhanced Transmission

A radical shift in the physics of subwavelength apertures occurred in 1998 with T. W. Ebbesen's report of extraordinary transmission (EOT) orders of magnitude greater than that predicted through subwavelength hole arrays milled in an opaque metal screen [17]. The enhanced transmission reported by Ebbesen is due to the existence of electromagnetic waves trapped at a metal-dielectric interface that are interacting with the free electrons of the metal [18]. These electromagnetic excitations are known as surface plasmon polaritons (SPPs). Recent applications of SPPs at visible frequencies have been realized by modern nanofabrication techniques, allowing for the structuring of subwavelength surface features that generate and guide the electromagnetic wave. A great deal of interest has been shown

regarding the enhanced transmission of visible wavelengths through subwavelength metallic hole arrays, slits, and bullseye lenses [19].

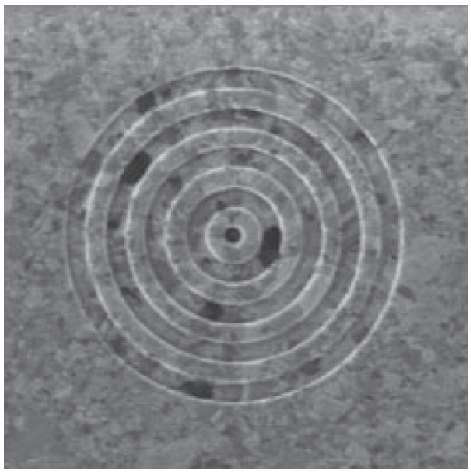

Figure 1.4: A bullseye lens designed for use at $\lambda = 660$ nm with a $d = 250$ nm diameter subwavelength aperture surrounded by grooves with 500 nm periodicity [3]. Reprinted with permission from AAAS.

The bullseye lens is of particular significance. It consists of subwavelength aperture surrounded by concentric corrugations on both the input and output sides of the metal surface [20–22]. An example of a bullseye lens is shown in Figure 1.4. Surface plasmons are resonantly excited by periodic corrugations on the input side. Corrugations on the output side serve to couple surface plasmons back to the radiation field and the geometry of the grooves can be tuned to focus the output beam [23, 24].

The entertainment and consumer electronics industry, which rely on optical data storage discs, have shown interest in subwavelength imaging applications [25, 26]. Bullseye lenses have been considered as a readout device for the ultra-dense storage of optical data [27]. Data, represented as surface pits, is read as reflections of a laser focused on the surface. The diffraction limited spot size places a limit on the smallest pit, which limits the data packing density. Subsequently smaller wavelengths have been used to read closer pits to increase data storage. Near-field techniques could reduce the pit size to be limited by the size of the readout head and would thereby increase the data packing density and readout rates [28]. Furthermore, data could be encoded in the illuminated spot as subwavelength surface fea-

tures that resonantly excite surface plasmon modes and modify the spectral content of the reflected signal [29].

Plasmonic devices have been designed for long wavelength radiation, where metals begin to behave as perfect electrical conductors and the structural parameters scale with the wavelength [7, 23, 30–35]. Applications of THz plasmonic devices range from enhancing detecting elements to biological sensing [36–38]. The work done in this thesis focuses on the design, fabrication, and performance of bullseye lenses for use at 325 GHz ($\lambda =$ 922μm), a frequency that has been shown to be optimum for the differential diagnostic for breast cancer [38, 39].

1.4 A THz Microscope for Cancer Detection

In Section 1.1, it was discussed that the Rayleigh criterion defines the limit of classical microscopy techniques to be on the order of the wavelength of the incident radiation, which for 325 GHz is around a millimeter. For edge detection of cancer cells, a resolution of ≈ 100 μm is required, which is subwavelength at THz frequencies [40]. Near-field aperture techniques lead to improved spatial resolution, however the low transmission through subwavelength apertures, low sensitivity of room temperature detectors, and low output power of typical sources results in low overall system signal-to-noise. While quantum cascade lasers provide higher power and hot electron bolometers have high sensitivity, they require cryogenic cooling [41]. If one were to use room temperature sources and detectors, the remaining component in the system that could improve matters is the focusing element.

Exploiting the enhanced transmission of a bullseye plasmonic lens provides a means to address this challenge. When placed immediately before the sample, the resolution is determined by the aperture size. The enhanced transmission conferred by the input rings of the bullseye structure results in an increase in the signal transmitted through the lens. This thesis presents the design, fabrication, and performance of plasmonic lenses operating at a frequency of 325 GHz. The plasmonic lens will serve as a key optical element

in a THz microscope with a tunable frequency range between $320-330$ GHz for the ex vivo detection of breast cancer cells. Our group is working in conjunction with Blue Sky Spectroscopy, whose expertise in THz instrumentation and optics have assisted us in the design of the THz imaging configuration [42]. Currently, we are able to scan samples at a speed of $\approx$ 5500 px $\cdot$ s^{-1}, more than 30 times faster than previous attempts to scan a tissue sample [38, 39]. Collaboration with Dr. Roy Goldstein at the University of Lethbridge and Dr. Jeff Dunn at the University of Calgary has provided our group access to tissue samples and proper sample preparation techniques [43, 44]. It is our hope that the successful fabrication and characterization of bullseye plasmonic lenses will lead to the development of a sensitive, fast-scanning THz microscope.

1.5 Thesis Overview

Surface plasmon polaritons are the key phenomenon that leads to enhanced transmission through subwavelength apertures. The main characteristics of SPPs can be described by classical electrodynamics. A review of the key concepts from electromagnetic theory is presented in Chapter 2, which builds a framework to understand the Drude model of electrical conduction in metals. Chapter 3 begins by solving Maxwell's equations on a planar metal-dielectric interface and general equations are derived that govern the unique properties of SPPs. Included is a discussion of the surface plasmon dispersion relation, the different types of surface modes, the generation of surface plasmons, and their evanescent decay. The material properties described Chapter 2 are reintroduced to highlight how SPPs differ at THz and visible frequencies. Chapter 4 then shifts to examining the transmission of light through subwavelength circular apertures and its dependence on aperture diameter and material thickness.

The design of various bullseye plasmonic lenses, which are optimized for enhanced transmission and beam confinement at 325 GHz, are introduced in Chapter 5. Chapter 6 introduces a tunable THz testbed that I designed for transmission and beam profile measure-

ments. This is followed by the experimental verification of the response of several bullseye lenses in Chapter 7.

Chapter 2

Electromagnetic Interaction with Matter

Surface plasmons can be viewed as electromagnetic modes that exist on the interface of a metal and a dielectric [45]. The characteristics of these modes are due to the unique optical properties of each media. Beginning with a review of Maxwell's equations, the starting point for classical electrodynamic problems, this chapter builds a framework for the theoretical description of surface plasmons given in Chapter 3. Included is a discussion on a material's response to an applied electric field (electric polarization), which generally is a function of frequency. The Drude model of electrical conduction is introduced to formulate this dependency for a non-magnetic metallic medium and the optical properties of metals at visible and THz frequencies are compared.

2.1 Maxwell's Equations in Free Space

Electromagnetic fields in free space are expressed in terms of the electric and magnetic field vectors $\vec{E}$ ($\mathrm{N}\cdot\mathrm{C}^{-1}$) and $\vec{B}$ (T), respectively. The space and time dependence of these vectors are described by Maxwell's equations [46]:

Gauss' Law for Electric Fields
$$\nabla \cdot \vec{E} = \frac{\rho}{\varepsilon_0} \tag{2.1a}$$

Gauss' Law for Magnetic Fields
$$\nabla \cdot \vec{B} = 0 \tag{2.1b}$$

Faraday's Law
$$\nabla \times \vec{E} = -\frac{\partial \vec{B}}{\partial t} \tag{2.1c}$$

The Ampère-Maxwell Law
$$\nabla \times \vec{B} = \mu_0 \left(\vec{J} + \varepsilon_0 \frac{\partial \vec{E}}{\partial t} \right). \tag{2.1d}$$

The constant ε_0 ($\mathrm{C}^2 \cdot \mathrm{N}^{-1} \cdot \mathrm{m}^{-2}$) is the *permittivity of free space* (or *vacuum permittivity*) and μ_0 ($\mathrm{N} \cdot \mathrm{A}^{-2}$) is the *permeability of free space* (or *vacuum permeability*), which are related to the speed of light in vacuum c ($\mathrm{m} \cdot \mathrm{s}^{-1}$) by $c = 1/\sqrt{\varepsilon_0 \mu_0}$. In the above form, Gauss' law for electric fields states that $\vec{E}$ diverges from areas in space with a *volume charge density* ρ ($\mathrm{C} \cdot \mathrm{m}^{-3}$). Conversely, the divergence of the magnetic field at any point is zero. Faraday's law of induction states that a time-vary magnetic field produces an electric field. The Ampère-Maxwell law says that a magnetic field is created by a changing electric field and/or a current $\vec{J}$, defined as the current per unit area-perpendicular-to-flow [47],

$$\vec{J} = -Ne\vec{v}, \qquad (\mathrm{A} \cdot \mathrm{m}^{-2}) \tag{2.2}$$

where N (m^{-3}) is the electron density, e (C) is the elementary charge, and $\vec{v}$ ($\mathrm{m} \cdot \mathrm{s}^{-1}$) is the velocity of the electrons.

Maxwell's equations, together with the Lorentz force law [47],

$$\vec{F} = q(\vec{E} + \vec{v} \times \vec{B}), \qquad (\mathrm{N}) \tag{2.3}$$

where $\vec{v}$ ($\mathrm{m} \cdot \mathrm{s}^{-1}$) is the velocity of a charged particle q (C), describe how electromagnetic fields are produced and how the fields affect charges.

In the absence of current and volume charge densities, Maxwell's equations can be combined to give

$$\nabla^2 \vec{E} = -\mu_0 \varepsilon_0 \frac{\partial^2 \vec{E}}{\partial t^2}, \tag{2.4}$$

which is the *electromagnetic wave equation* written in terms of $\vec{E}$, and describes the propagation of electromagnetic waves.

2.2 Permittivity

Materials can generally be categorized into two broad groups: *dielectrics* (insulators) and *metals* (conductors), both of which are of importance to the discussion of surface plasmons. Dielectrics are materials where all charges are attached to specific atoms or molecules [47]. An applied electric field can have the effect of distorting the charge distribution within a dielectric. Consider the case of a single neutral atom. The electric field will separate the positively charged nucleus and the negatively charged electron cloud such that they are aligned with the field. When in equilibrium, the atom in this dipole configuration is said to be *polarized*. The dipole moment $\vec{p}$ ($\mathrm{C}\cdot\mathrm{m}$) is a measure of the polarity of the single atom system and is typically proportional to the applied electric field. The cumulative effect of many polarized atoms can be described by the *polarization density*,

$$\vec{P} = \frac{\langle \vec{p} \rangle}{V}, \qquad (\mathrm{C}\cdot\mathrm{m}^{-2}) \tag{2.5}$$

which is the average dipole moment $\langle \vec{p} \rangle$ ($\mathrm{C}\cdot\mathrm{m}$) per unit volume V (m^3). Like the dipole moment of a single atom, the polarization density is often proportional to the applied electric field and can be written as

$$\vec{P} = \varepsilon_0 \chi_e \vec{E}, \qquad (\mathrm{C}\cdot\mathrm{m}^{-2}) \tag{2.6}$$

where χ_e is a unitless proportionality factor referred to as the *electric susceptibility* of the material and $\vec{E}$ is the total field due to both the bound charges within the dielectric and any other free charge contributions. Materials described by Equation 2.6 are called *linear*

dielectrics.

The total electric field $\vec{E}$ can be separated from the field produced by the bound charges $\vec{P}$, leaving the field due to the free charges alone,

$$\vec{D} = \varepsilon_0 \vec{E} + \vec{P}, \qquad (\mathrm{C} \cdot \mathrm{m}^{-2}) \quad (2.7)$$

which is known as the *electric displacement*. Combining Equations 2.6 and 2.7 gives

$$\vec{D} = \varepsilon \vec{E}, \qquad (\mathrm{C} \cdot \mathrm{m}^{-2}) \quad (2.8)$$

where $\varepsilon = \varepsilon_0(1 + \chi_e)$ is the *absolute permittivity* of the material and describes the strength of the polarization induced by the total electric field. A common unitless formulation is the ratio of the absolute permittivity to the permittivity of free space, called the *relative permittivity* or *dielectric constant*:

$$\varepsilon_r = 1 + \chi_e = \frac{\varepsilon}{\varepsilon_0}. \quad (2.9)$$

In Section 2.3.3, the term "dielectric constant" will be shown to be a misnomer, since the relative permittivity of a material can be a complex-valued function of frequency. To avoid confusion with different nomenclature, this thesis will refer to the dielectric constant as the *relative dielectric function* or simply the *permittivity* of the medium.

Equation 2.8 is one of two constitutive relationships for simple homogeneous, isotropic linear materials [47]. Following a similar process, the total magnetic field $\vec{B}$ can be separated into field contributions due to the free currents $\vec{H}$ $(\mathrm{A} \cdot \mathrm{m}^{-1})$ and bound currents $\vec{M}$ $(\mathrm{A} \cdot \mathrm{m}^{-1})$:

$$\vec{B} = \mu_0(\vec{H} + \vec{M}) = \mu_0(1 + \chi_m)\vec{H} = \mu \vec{H}. \qquad (\mathrm{T}) \quad (2.10)$$

This is the second constitutive relationship with analogous quantities χ_m (the unitless *mag-*

netic susceptibility) and μ (*permeability* in $\mathrm{N}\cdot\mathrm{A}^{-2}$). Note that for non-magnetic materials, $\mu = \mu_0$.

2.3 Maxwell's Equations in Matter

Maxwell's equations as given in Section 2.1 are general and apply to fields generated within a material due to the effects of polarization and magnetization as well as those in free space [46]. I.e., $\vec{E}$ and $\vec{B}$ are the total fields in the system and account for all the enclosed charge (both free and bound) and all currents (both free and bound). In the form of Equations 2.1a-2.1d, it is difficult to separate these two contributions.

In Section 2.2, constitutive relations were given that allow for the electric and magnetic field to be described in terms of free charge density (Equation 2.8) and free volume current density (Equation 2.10). Using these expressions, Maxwell's equations become

$$\nabla\cdot\vec{D} = \rho_f \tag{2.11a}$$

$$\nabla\cdot\vec{B} = 0 \tag{2.11b}$$

$$\nabla\times\vec{E} = -\frac{\partial\vec{B}}{\partial t} \tag{2.11c}$$

$$\nabla\times\vec{H} = \vec{J}_f + \frac{\partial\vec{D}}{\partial t}, \tag{2.11d}$$

where ρ_f is the free volume charge density and J_f is the free current density. In the case of metals, J_f describes the flow of charge within the conductor and is, in general, proportional to the electric field [47]:

$$\vec{J}_f = \sigma\vec{E}. \qquad (\mathrm{A}\cdot\mathrm{m}^{-2}) \tag{2.12}$$

The above equation is a form of Ohm's law. The proportionality factor σ ($\mathrm{S}\cdot\mathrm{m}^{-1}$) is an empirical constant known as the *electrical conductivity* of the medium and is a measure of the

material's ability to conduct an electrical current. The reciprocal of electrical conductivity is *electrical resistivity* ρ ($\Omega \cdot \mathrm{m}$).

2.3.1 Electromagnetic Boundary Conditions

Boundary conditions impose restrictions on the electromagnetic field at an abrupt interface between two media. An understanding of these conditions is essential for derivation surface plasmons modes, which exist on the interface between a metal and dielectric. Discontinuities in the fields can be determined from Maxwell's equations in their integral form, derivations of which can be found in introductory texts on electromagnetism [47]. The general boundary conditions are as follows: let $\hat{n}_{12}$ be a unit vector pointing from media 1 to 2 that is perpendicular to an infinitesimal area of the interface. Across the interface, the tangential components (parallel to the interface) of the $\vec{E}$-field and $\vec{H}$-field, $\vec{E}^{\parallel} = \hat{n}_{12} \times (\vec{E} \times \hat{n}_{12})$ and $\vec{H}^{\parallel} = \hat{n}_{12} \times (\vec{H} \times \hat{n}_{12})$, behave as [47]

$$\vec{E}_1^{\parallel} - \vec{E}_2^{\parallel} = 0 \tag{2.13a}$$

$$\vec{H}_1^{\parallel} - \vec{H}_2^{\parallel} = \vec{K}_f \times \hat{n}_{12}. \tag{2.13b}$$

I.e., the parallel component of $\vec{E}$ is continuous, whereas the parallel component of $\vec{H}$ is discontinuous due to a surface electric current density $\vec{K}_f$ ($\mathrm{A} \cdot \mathrm{m}^{-1}$). Two additional boundary conditions dictate how the normal components of the electric field and the electric displacement, $\vec{D}^{\perp} = (\hat{n}_{12} \cdot \vec{D})\hat{n}_{12}$ and $\vec{B}^{\perp} = (\hat{n}_{12} \cdot \vec{B})\hat{n}_{12}$, behave across the interface:

$$D_1^{\perp} - D_2^{\perp} = \sigma_f \tag{2.14a}$$

$$B_1^{\perp} - B_2^{\perp} = 0. \tag{2.14b}$$

The normal component of $\vec{B}$ is continuous and the normal component of the $\vec{D}$ is discontin-

uous due to a surface charge density σ_f ($\mathrm{C}\cdot\mathrm{m}^{-1}$).

2.3.2 Time-Harmonic Maxwell's Equations

Maxwell's equations can be cast in another form by assuming that the four field vectors $\vec{E}$, $\vec{H}$, $\vec{D}$, and $\vec{B}$ can be written as time-harmonic propagating fields. This thesis uses the general form

$$\vec{A}(\vec{r},t) = \vec{A}_0 e^{i\phi} e^{i(\vec{k}\cdot\vec{r}-\omega t)}, \tag{2.15}$$

where A_0 is the field amplitude, $\vec{r}$ (m) is the position vector, λ (m) is the wavelength, $\vec{k} = 2\pi/\lambda$ (m^{-1}) is the wave vector, $\omega = 2\pi f$ ($\mathrm{rad}\cdot\mathrm{s}^{-1}$) is the angular frequency, and ϕ (rad) is the phase.

Maxwell's equations can then be re-written in the following way by replacing the time derivatives by $\frac{\partial}{\partial t} = -i\omega$:

Gauss' Law for Electric Fields	$\nabla\cdot\vec{D} = \rho_f$	(2.16a)
Gauss's Law for Magnetic Fields	$\nabla\cdot\vec{B} = 0$	(2.16b)
Faraday's Law	$\nabla\times\vec{E} = i\omega\vec{B}$	(2.16c)
The Ampère-Maxwell Law	$\nabla\times\vec{H} = \vec{J}_f - i\omega\vec{D}.$	(2.16d)

2.3.3 Effective Permittivity

Consider the Ampére-Maxwell relation for time-harmonic dependence (Equation 2.16d). Substituting in Ohm's law (Equation 2.12) for the free current density $\vec{J}_f$ and the constitutive relation for $\vec{D}$ (Equation 2.8), we are left with [48]

$$\begin{aligned} \nabla \times \vec{H} + i\omega\varepsilon\vec{E} - \sigma\vec{E} &= 0 \\ \nabla \times \vec{H} + i\omega\left(\varepsilon + \frac{i\sigma}{\omega}\right)\vec{E} &= 0 \\ \nabla \times \vec{H} + i\omega\widetilde{\varepsilon}(\omega)\vec{E} &= 0, \end{aligned} \tag{2.17}$$

where

$$\widetilde{\varepsilon}(\omega) = \varepsilon + \frac{i\sigma}{\omega}. \qquad (\mathrm{C}^2 \cdot \mathrm{N}^{-1} \cdot \mathrm{m}^{-2}) \tag{2.18}$$

$\widetilde{\varepsilon}(\omega)$ is referred to as the *effective permittivity*. Analogous to the absolute permittivity of a dielectric material from Section 2.2, the effective permittivity is now a complex-valued parameter that accounts for free charge carrier effects associated with the conductivity of a metal. Furthermore,

$$\varepsilon_m \equiv \frac{\widetilde{\varepsilon}(\omega)}{\varepsilon_0} = \varepsilon_r + \frac{i\sigma}{\varepsilon_0\omega}, \tag{2.19}$$

is the *relative dielectric function*. For short hand, this thesis will use ε_m to represent the relative dielectric function for metals. For a complete functional form of ε_m, the Drude model of electrical condition, described in the following section, can be used to give an expression for the conductivity of a metal.

2.4 The Drude Model of Electrical Conduction in Metals

Drude theory was developed by applying the kinetic theory of gases to a metal in order to describe electrical conduction [49]. On the simplest level, kinetic theory considers the molecules of a gas as solid spheres that travel linearly until collisions occur with other molecules. The time that a single collision takes is assumed to be negligible and it is also assumed that no other forces act between the particles except those that take place

during the brief collision time. By analogy, Drude theory assumes that when a metal is formed by its constitutive element, the valence electrons become detached and are free to travel through the metal creating an electron "gas". The remaining metallic ions, which consist of the positive nucleus and the remaining core electrons, form a lattice of immobile, indivisible positive ions. Collisions between conduction electrons and the ion lattice are assumed to be instantaneous events and occur at a frequency ω_τ (rad $\cdot$ s^{-1}). Any electron-electron interactions and electron-ion interactions due to the Lorentz force that occur in between collisions are ignored.

With these assumptions in mind, the motion of an electron in a metal subject to an applied electric field, $\vec{E}$, can be written as the result of two forces [48]. The first is the force due to the applied field, $-e\vec{E}$. The second is a damping force, $-m\,\vec{v}\,/\tau$, where $\vec{v}$ is the mean velocity of the electrons and $\tau = 1/\omega_\tau$. The equation of motion for a conduction electron is then [48]

$$m\frac{d\vec{v}}{dt} = -e\vec{E} - m\frac{\vec{v}}{\tau}. \tag{2.20}$$

Substituting the expression for current density (Equation 2.2) into the equation of motion gives

$$\frac{d\vec{J}_f}{dt} = \left(\frac{-Ne^2}{m}\right)\vec{E} - \frac{\vec{J}_f}{\tau}. \tag{2.21}$$

For time-harmonic fields,

$$\begin{aligned}\left(-i\omega + \frac{1}{\tau}\right)\vec{J}_f &= \left(\frac{-Ne^2}{m}\right)\vec{E} \\ \vec{J}_f &= \left(\frac{Ne^2}{m}\right)\frac{(1/\tau + i\omega)}{(1/\tau^2 + \omega^2)}\vec{E}.\end{aligned} \tag{2.22}$$

Comparing this equation with Ohm's law (Equation 2.12), the conductivity as a function of

frequency is

$$\sigma(\omega) = \left(\frac{Ne^2}{m}\right)\frac{(1/\tau + i\omega)}{(1/\tau^2 + \omega^2)}. \tag{2.23}$$

Substituting this result into relative dielectric function (Equation 2.18) gives [45]

$$\varepsilon_m = 1 - \frac{\omega_p^2}{\omega^2 + i\omega_\tau\omega}, \tag{2.24}$$

where ω_p has been defined to be

$$\omega_p = \sqrt{\frac{Ne^2}{m\varepsilon_0}} \qquad (\text{rad}\cdot\text{s}^{-1}) \tag{2.25}$$

and is known as the *plasma frequency*. The plasma frequency physically corresponds to the natural oscillation frequency of the collective motion of the free-electron plasma charge density, a derivation of which can be found in [50]. The quantum mechanical particles associated with these oscillations are called *volume* or *bulk plasmons* [45]. The value of ε_r in Equation 2.18 was chosen to be unity to neglect high frequency dipolar interactions with the bound electrons in the metal [48]. Equation 2.24 can further be separated to give the real and imaginary parts of the dielectric function:

$$\varepsilon_m = \varepsilon_m' + i\varepsilon_m'' \tag{2.26a}$$

$$\varepsilon_m' = 1 - \frac{\omega_p^2}{\omega^2 + \omega_\tau^2} \tag{2.26b}$$

$$\varepsilon_m'' = \frac{\omega_p^2\omega_\tau}{\omega(\omega^2 + \omega_\tau^2)} \tag{2.26c}$$

An important case to examine is at frequencies less than the plasma frequency ($\omega < \omega_p$) with damping that is either small or negligible. When neglected, the relative dielectric function becomes purely real and negative. The condition $\varepsilon_m' < 0$ is required

Table 2.1: Values of the plasma frequency, ω_p, and damping frequency, ω_τ, as described by the Drude model, for Cu, Al, Au, and Ag. Experimental data was collected and fit by Ordal et al. [1].

Material	$\omega_p/2\pi$ (GHz)	$\omega_\tau/2\pi$(GHz)
Cu	1.91×10^6	8.33×10^3
Al	3.57×10^6	19.4×10^3
Au	2.17×10^6	6.48×10^3
Ag	2.17×10^6	4.35×10^3

for the existence of plasmon resonances such as surface plasmons. In the case of small damping, the imaginary part is small and positive [45]. ε_m'' is associated with "lossy" materials and stronger damping due to absorption. The latter point will become more clear in Chapter 3, where analytical formulas are given for the damping of surface plasmons.

2.4.1 General Properties at Visible and THz Frequencies

Anticipating the characteristics of surface plasmons derived in Chapter 3, it is instructive to compare the values that the relative dielectric function takes at visible frequencies to their THz counterparts. For example, at the visible frequency $f = 4.74 \times 10^{14}$ Hz for $\lambda = 632.8$ nm, permittivity data for Au from Johnson and Christy [51] was fitted with Lumerical FDTD Solutions [52] multi-coefficient model to give a relative dielectric constant of $\varepsilon_m = -11.7 + i1.2$. Low absolute permittivity values are typical at visible frequencies and lead to the electromagnetic field penetrating into the surface of the metal at depths that are relatively large with respect to the wavelength (yet small in an absolute sense). The implications of this will be explored in detail in Chapter 3, but qualitatively it can be stated that this leads to increased coupling with the free charge density [53]. Consequently, the surface plasmon mode is highly confined to the surface of the metal (with a small skin depth into the dielectric medium) and propagates at moderate distances with respect to the wavelength.

In the near- to far-infrared, Ordal et al. compiled a collection of experimental permittivity values for Cu, Al, Au, and Ag from 900 GHz to 750×10^6 GHz and made best eyeball

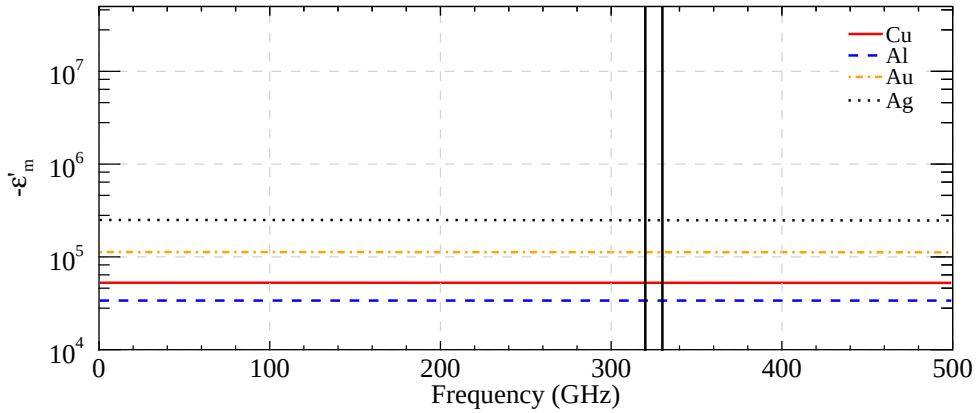

(a) Real part of the complex permittivity.

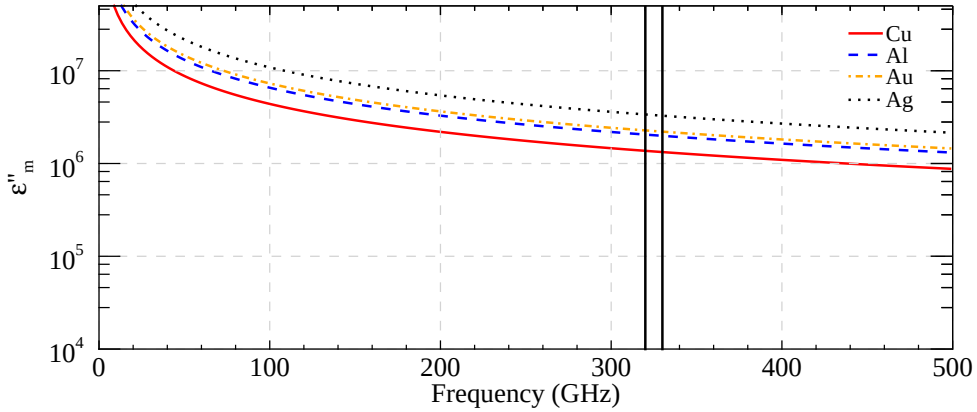

(b) Imaginary part of the complex permittivity.

Figure 2.1: The real and imaginary components of the relative dielectric function, ε_m, for Cu, Al, Au, and Ag in a section of the THz regime. The vertical band represents the tunable bandwidth of our THz line source (Section 6.1.1)

fits for the Drude model parameters ω_p and ω_τ [1]. These parameters are as summarized in Table 2.1 and were used to calculate the relative dielectric function for frequencies up to 500 GHz (Figure 2.1). At our operational frequency of 325 GHz, the Drude model give a relative dielectric function of $\varepsilon_m = -1.12 \times 10^5 + i2.24 \times 10^6$. THz permittivity values are typically 5-6 orders of magnitude larger than in the visible and approaches that of a perfect electrical conductor ($\varepsilon_m \rightarrow -\infty$). This is characterized by the metallic skin depth approaching zero and minimizes the coupling of incident electromagnetic radiation

to surface plasmon modes and leads to weak surface confinement (i.e., the field extends far into the dielectric) and increased propagation lengths.

It should be noted that the experimental data used by Ordal et al. to parametrize the Drude model are outside the frequency range of the values calculated in Figure 2.1. In the absence of more experimental data, the Drude model parameters fit by Ordal et al. were seen as the best available choice and in line with assumptions made by other groups operating at THz frequencies [53–56].

As a final note, an equivalent discussion on optical properties could be made in reference to the material's conductivity ($\sigma = \sigma' + i\sigma''$), rather than permittivity, but is left for other references [45]. Values of conductivity at THz frequencies are shown in Figure 2.2.

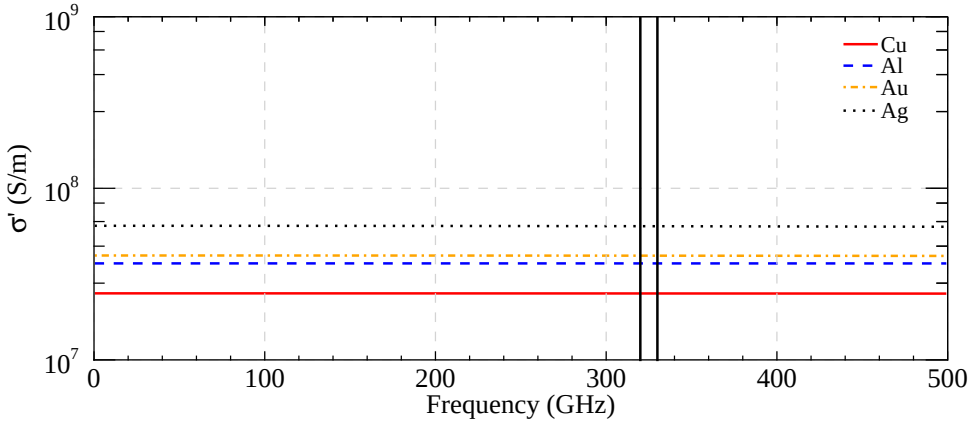

(a) Real part of the complex conductivity.

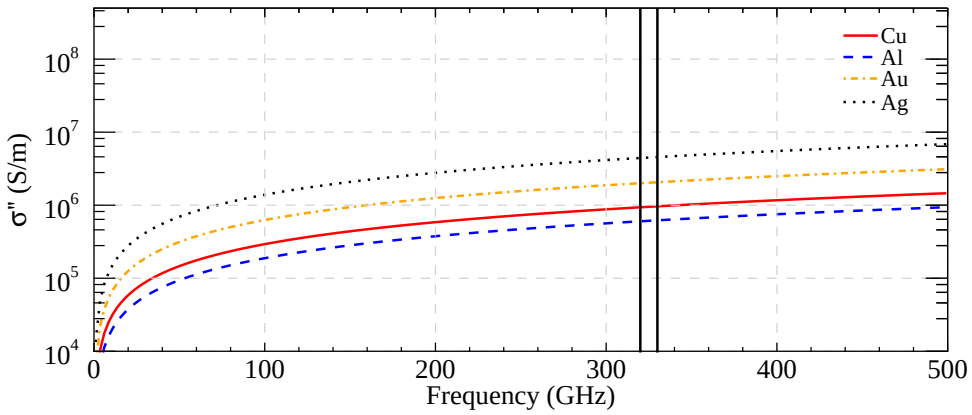

(b) Imaginary part of the complex conductivity.

Figure 2.2: The real and imaginary components of the complex conductivity, $\sigma(\omega)$, for Cu, Al, Au, and Ag in a section of the THz regime. The vertical band represents the tunable bandwidth of our THz line source (Section 6.1.1).

Chapter 3

Surface Plasmon Polaritons

In scientific literature, there are many loose, inadequate, or incomplete definitions of surface plasmons (SPs). This is not uncommon in emerging fields. A general definition typically states that SPs arise from the collective charge oscillations of the conduction electrons near the surface of a metal [45]. Other definitions of surface plasmons emphasize the "on" suffix, implying that SPs are quantized excitations with particle-like properties and should be described strictly by quantum mechanics [57]. However, the important characteristics of surface plasmons can found by treating them as simply electromagnetic modes that exist near the surface of a particular system [45]. This view places the role of the conduction electrons within the relative dielectric function, ε_m (Section 2.4).

The system of primary interest, both because of its supported modes and relative simplicity, is that of a planar metal-dielectric interface. Different classifications of surface modes exist for nearly all values of ε_m, which complicates matters by introducing a variety of adjectives to describe the characteristics of various surface modes (e.g., propagating, pseudo-propagating, localized, radiating, non-radiating, bound, evanescent, etc.). For an extensive discussion on the evolution of the terminology used in plasmonics, the reader is directed to [45] and [57].

The exact type of surface mode being discussed is not often addressed when deriving surface plasmons [50, 58–64]. To address this ambiguity, this chapter introduces the solutions to Maxwell's equations on a planar interface under general conditions and derives a dispersion relation that governs many types of surface modes. The material properties

on both sides of the interface will then be introduced, restricting our discussion to that of *propagating surface plasmon* (PSPs). The excitation of PSPs by means of a diffraction grating is discussed followed by a comparison of the properties of PSPs at visible and THz frequencies.

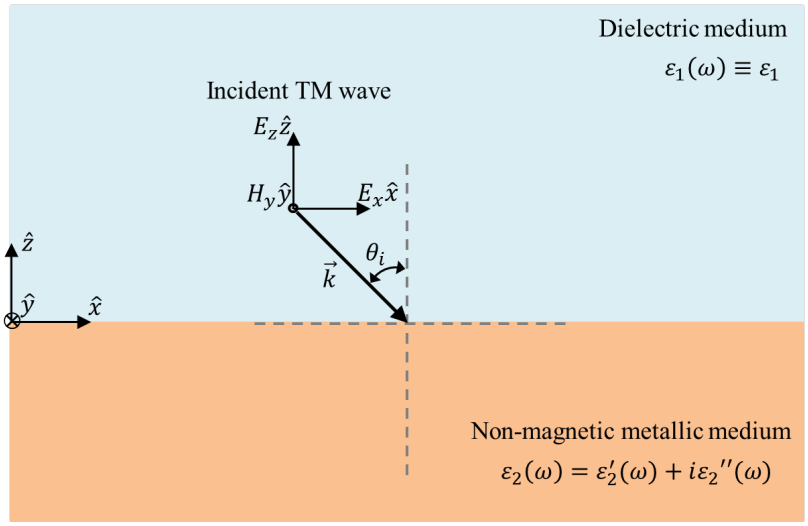

Figure 3.1: A schematic of a planar interface between a metal and dielectric. A transverse magnetic (TM) wave is incident in the *xz*-plane.

3.1 Solving Maxwell's Equations on a Planar Interface

Consider two half spaces that are separated by an interface at $z = 0$ (Figure 3.1). Let $z < 0$ consist of medium 1 with optical properties described by a permittivity of ε_1 and let $z > 0$ consist of medium 2 with optical properties described by a permittivity of ε_2. Letting the plane of incidence be the *xz*-plane, the general form of an electromagnetic wave in both media is, via Equation 2.15,

$$\vec{A}(\vec{r},t) = A_x\hat{x} + A_y\hat{y} + A_z\hat{z} = \vec{A}_0 e^{i(k_x x \pm k_z z - \omega t)}. \tag{3.1}$$

k_x is the component of the wave vector in the x-direction (parallel to the interface) and $\pm k_z$ is the component in the z-direction (normal to the interface), with "$-$" chosen for medium 1 and "$+$" chosen for medium 2. Assuming that there are no free charges and

currents ($\rho_f = 0, \vec{J}_f = 0$) and that both materials are non-magnetic ($\mu = \mu_0$), Maxwell's equations in their time-harmonic form (Equations 2.16a-2.16d) become

$$\text{Gauss' Law for Electric Fields} \qquad \nabla \cdot \vec{E} = 0 \tag{3.2a}$$

$$\text{Gauss's Law for Magnetic Fields} \qquad \nabla \cdot \vec{B} = 0 \tag{3.2b}$$

$$\text{Faraday's Law} \qquad \nabla \times \vec{E} = i\omega\vec{B} \tag{3.2c}$$

$$\text{The Ampère-Maxwell Law} \qquad \nabla \times \vec{B} = -\frac{i\omega\varepsilon_r}{c^2}\vec{E}. \tag{3.2d}$$

The partial derivative with respect to x can be replaced with $\partial/\partial x = ik_x$ and those with respect to z by $\partial/\partial z = \pm ik_z$ (with $\pm$ chosen using the previously stated sign convention). Since there is no spatial variation in the perpendicular in-plane direction, $\partial/\partial y = 0$. Maxwell's curl equations can then be expanded and simplified as

$$(\vec{\nabla} \times \vec{B})_x = \cancelto{0}{\frac{\partial B_z}{\partial y}} - \frac{\partial B_y}{\partial z} = \frac{-i\omega\varepsilon_r}{c^2}E_x \qquad \Rightarrow \qquad \frac{\partial B_y}{\partial z} = \frac{i\omega\varepsilon_r}{c^2}E_x \tag{3.3a}$$

$$(\vec{\nabla} \times \vec{B})_y = \frac{\partial B_x}{\partial z} - \frac{\partial B_z}{\partial x} = \frac{-i\omega\varepsilon_r}{c^2}E_y \qquad \Rightarrow \qquad \frac{\partial B_x}{\partial z} - ik_x B_z = -\frac{i\omega\varepsilon_r}{c^2}E_y \tag{3.3b}$$

$$(\vec{\nabla} \times \vec{B})_z = \frac{\partial B_y}{\partial x} - \cancelto{0}{\frac{\partial B_x}{\partial y}} = \frac{-i\omega\varepsilon_r}{c^2}E_z \qquad \Rightarrow \qquad k_x B_y = -\frac{\omega\varepsilon_r}{c^2}E_z \tag{3.3c}$$

$$(\vec{\nabla} \times \vec{E})_x = \cancelto{0}{\frac{\partial E_z}{\partial y}} - \frac{\partial E_y}{\partial z} = i\omega B_x \qquad \Rightarrow \qquad -\frac{\partial E_y}{\partial z} = i\omega B_x \tag{3.3d}$$

$$(\vec{\nabla} \times \vec{E})_y = \frac{\partial E_x}{\partial z} - \frac{\partial E_z}{\partial x} = i\omega B_y \qquad \Rightarrow \qquad \frac{\partial E_x}{\partial z} - ik_x E_z = i\omega B_y \tag{3.3e}$$

$$(\vec{\nabla} \times \vec{E})_z = \frac{\partial E_y}{\partial x} - \cancelto{0}{\frac{\partial E_x}{\partial y}} = i\omega B_z \qquad \Rightarrow \qquad k_x E_y = \omega B_z \tag{3.3f}$$

The x- and z-components of the electromagnetic field can then be expressed as

$$E_x = -i\left(\frac{c^2}{\omega}\right)\left(\frac{1}{\varepsilon_r}\right)\frac{\partial B_y}{\partial z} \tag{3.4a}$$

$$E_z = -\left(\frac{c^2}{\omega}\right)\left(\frac{k_x}{\varepsilon_r}\right)B_y \tag{3.4b}$$

$$B_x = i\left(\frac{1}{\omega}\right)\frac{\partial E_y}{\partial z} \tag{3.4c}$$

$$B_z = \left(\frac{1}{\omega}\right)k_x E_y. \tag{3.4d}$$

To fully define the fields, E_y and B_y are required. By taking Equation 3.3b and substituting in the expressions for B_x and B_z and taking Equation 3.3e and substituting in the expressions for E_x and E_z, two uncoupled equations emerge:

$$\left[\frac{\partial^2}{\partial z^2} + k_0^2\varepsilon_r - k_x^2\right]E_y = 0 \tag{3.5}$$

$$\left[\frac{\partial^2}{\partial z^2} + k_0^2\varepsilon_r - k_x^2\right]B_y = 0. \tag{3.6}$$

It can be shown that solutions to these fall under two general categories: if $E_y = B_x = B_z = 0$ the waves are said to be *transverse magnetic* (TM) and if $B_y = E_x = E_z = 0$ they are *transverse electric* (TE) [47]. Furthermore, it can be shown that surface modes only exist for TM polarizations (the details of which can be found in [50]). The TM solutions in each media have the following general forms:

In medium 1,

$$\vec{E}_1 = (E_{x1}, 0, E_{z1})e^{i(k_{x1}x - k_{z1}z - \omega t)} \tag{3.7a}$$

$$\vec{H}_1 = (0, H_{y1}, 0)e^{i(k_{x1}x - k_{z1}z - \omega t)}. \tag{3.7b}$$

In medium 2,

$$\vec{E}_2 = (E_{x2}, 0, E_{z2}) e^{i(k_{x2}x + k_{z2}z - \omega t)} \tag{3.8a}$$

$$\vec{H}_2 = (0, H_{y2}, 0) e^{i(k_{x2}x + k_{z2}z - \omega t)}. \tag{3.8b}$$

The TM field components, along with the assumption of no free-charges or currents at the interface, reduce the electromagnetic boundary conditions discussed in Section 2.3.1 to

Boundary Condition 1 $$E_{x1} = E_{x2} \tag{3.9a}$$

Boundary Condition 2 $$B_{y1} = B_{y2} \tag{3.9b}$$

Boundary Condition 3 $$\varepsilon_1 E_{z1} = \varepsilon_2 E_{z2}, \tag{3.9c}$$

where ε_1 and ε_2 are the relative dielectric functions in each media.

The goal now is to arrive at expressions that relate k_{x1}, k_{x2}, k_{z1}, and k_{z2}. For the x-components of the wave vector, consider boundary condition 3 with the expressions for E_z (Equation 3.4b) in both media:

$$\begin{aligned} \varepsilon_1 E_{z1} &= \varepsilon_2 E_{z2} \\ -\varepsilon_1 \left(\frac{c^2}{\omega}\right)\left(\frac{k_{x1}}{\varepsilon_1}\right) B_{y1} &= -\varepsilon_2 \left(\frac{c^2}{\omega}\right)\left(\frac{k_{x2}}{\varepsilon_2}\right) B_{y2} \\ k_{x1} B_{y1} &= k_{x2} B_{y2} \end{aligned} \tag{3.10}$$

Using boundary condition 2 (Equation 3.9b), we are left with

$$k_{x1} = k_{x2} = k_x. \tag{3.11}$$

A similar process is used to find an expression relating the z-component of the wave vector in both media. Using boundary condition 1 (Equation 3.9a) with the expression for E_x (Equation 3.4a),

$$\begin{aligned} E_{x1} &= E_{x2} \\ -i\left(\frac{c^2}{\omega}\right)\left(\frac{1}{\varepsilon_1}\right)(-ik_{z1}B_{y1}) &= -i\left(\frac{c^2}{\omega}\right)\left(\frac{1}{\varepsilon_2}\right)(ik_{z2}B_{y2}) \\ -\left(\frac{k_{z1}}{\varepsilon_1}\right)B_{y1} &= \left(\frac{k_{z2}}{\varepsilon_2}\right)B_{y2}. \end{aligned} \tag{3.12}$$

Along with boundary condition 2 (Equation 3.9b), we arrive at

$$\frac{k_{z1}}{k_{z2}} = -\frac{\varepsilon_1}{\varepsilon_2}. \tag{3.13}$$

The desire now is to find expressions for k_x, k_{z1}, and k_{z2} in terms of the permittivity of both media. With the aid of Gauss' law (Equation 3.2a) applied to the fields in both media, we can write:

Gauss' Law for Electric Fields

$$\frac{\partial E_x}{\partial x} = -\frac{\partial E_z}{\partial z} \tag{3.14a}$$

Medium 1 $(z < 0)$

$$\begin{aligned} ik_x E_{x1} &= ik_{z1}E_{z1} \\ E_{x1} &= \left(\frac{k_{z1}}{k_x}\right)E_{z1} \end{aligned} \tag{3.14b}$$

Medium 2 $(z > 0)$

$$\begin{aligned} ik_x E_{x2} &= -ik_{z2}E_{z2} \\ E_{x2} &= -\left(\frac{k_{z2}}{k_x}\right)E_{z2}. \end{aligned} \tag{3.14c}$$

Taking the y-component of Faraday's law (Equation 3.3e) and substituting in the above

expressions for E_{x1}, E_{x2}, and B_y from Equation 3.4b gives

Faraday's Law
$$\frac{\partial E_x}{\partial z} - ik_x E_z = i\omega B_y$$

Medium 1 ($z < 0$)
$$-ik_{z1}E_{x1} - ik_x E_{z1} = i\omega B_y$$
$$-ik_{z1}\left(\frac{k_{z1}}{k_x}\right)E_{z1} - ik_x E_{z1} = -ik_0^2\left(\frac{\varepsilon_1}{k_x}\right)E_{z1}$$

$$k_x^2 = k_0^2\varepsilon_1 - k_{z1}^2, \tag{3.15a}$$

and similarly,

Medium 2 ($z > 0$)
$$k_x^2 = k_0^2\varepsilon_2 - k_{z2}^2. \tag{3.15b}$$

There are now three equations relating the three unknown wave vector components: Equations 3.13, 3.15a, and 3.15b. Squaring Equation 3.13 and substituting in Equations 3.15a and 3.15b gives an expression for k_x,

$$k_x^2 = k_0^2\left(\frac{\varepsilon_1\varepsilon_2}{\varepsilon_1+\varepsilon_2}\right), \tag{3.16}$$

and substituting k_x back into Equations 3.15a and 3.15b gives expressions for k_{z1} and k_{z2},

$$k_{z1}^2 = k_0^2\left(\frac{\varepsilon_1^2}{\varepsilon_1+\varepsilon_2}\right) \tag{3.17}$$
$$k_{z2}^2 = k_0^2\left(\frac{\varepsilon_2^2}{\varepsilon_1+\varepsilon_2}\right), \tag{3.18}$$

which are now expressed in terms of the permittivity of each medium.

3.2 General Properties of Surface Plasmon Modes

Having solved Maxwell's equations on a planar interface, we are now in a position to apply assumptions about the permittivity in both media. Let medium 1 ($z < 0$) be a metal with a complex relative dielectric function $\varepsilon_1 \equiv \varepsilon_m$ such that

$$\varepsilon_m = \varepsilon_m' + i\varepsilon_m'', \tag{3.19}$$

where ε_m' and ε_m'' are the real and imaginary parts, respectively, with a frequency-dependent functional form given by the Drude model (Equation 2.26). Let medium 2 ($z > 0$) be a dielectric with a constant, positive, and real relative permittivity $\varepsilon_2 \equiv \varepsilon_d$. The system now describes the coupling of an electromagnetic field to the collective plasma oscillations of the free-electron gas in a metal. These modes are called *surface plasmons*. As mentioned at the beginning of this chapter, a variety of terminology is used to describe surface plasmons. Fortunately, many of these can be clarified by discussing their characteristic lengths, namely the skin depth into the metal/dielectric and propagation length, that are derived from the wave vector components k_x, k_{z1}, and k_{z2}.

3.2.1 Skin Depth and Confinement

The wave vector components $k_{z1} = k_{zm}$ in the metal and $k_{z2} = k_{zd}$ in the dielectric are both complex due the metal's complex dielectric function, i.e.,

$$k_{zm} = k_{zm}' + ik_{zm}'' \tag{3.20a}$$

$$k_{zd} = k_{zd}' + ik_{zd}''. \tag{3.20b}$$

From Equation 3.1, the imaginary component of the wave vector can be used to determine a distance normal to the interface where the field *amplitude* decreases to a factor of $1/e$, known as the *skin depth*:

$$\delta_m = \frac{1}{k''_{zm}} \quad \text{(m)} \quad (3.21)$$

$$\delta_d = \frac{1}{k''_{zd}}. \quad \text{(m)} \quad (3.22)$$

3.2.2 Propagation Length

The x-component of the wave vector is often called the *surface plasmon propagation constant* and is given a variety of symbols ($k_x = k_{SP} = \beta = q$) [50, 57–59]. For future clarity, this thesis will exclusively use the notation k_x. Since ε_m is complex, k_x is also complex,

$$k_x = k'_x + ik''_x = k_0\sqrt{\frac{\varepsilon_d\varepsilon_m}{\varepsilon_d + \varepsilon_m}}. \quad (3.23)$$

The distance (parallel to the interface) that the *intensity* of the electromagnetic field drops by $1/e$ is

$$L = \frac{1}{2k''_x}. \quad \text{(m)} \quad (3.24)$$

Note the subtle distinction between the definition of the propagation length, defined in terms $1/e$ field intensity, and the skin depth, defined in terms of the $1/e$ field amplitude.

3.3 The Surface Plasmon Dispersion Relationship

The solution to Maxwell's equations in Section 3.1 is an example of a *bound* or *surface mode*, which are modes that exist in the absence of an incident wave and exist only due to the presence of an interface. It is required that an incident wave *excites* or *couples to* the mode such that the two modes have the same real part of frequency and wave vector in order to generate and maintain the electromagnetic wave [45]. This is analogous to energy

and momentum conservation via $E = \hbar\omega$ and $\vec{p} = \hbar\vec{k}$, respectively. Coupling occurs under specific configurations, i.e., resonant conditions that satisfy the conservation requirements. These conservation requirements are governed by a *dispersion relation* that connects ω and $\vec{k}$.

The conditions required to couple incident light to a surface plasmon mode is often considered for the case of ideal metals and the imaginary part of ε_m is neglected [50, 58]. This leads to a specific scenario where k_{zd} and k_{zm} become purely imaginary and k_x is real. Therefore, the dispersion relation that governs the different surfaces modes is given by the x-component of the wave vector

$$k_x = \frac{\omega}{c}\sqrt{\frac{\varepsilon_d \varepsilon_m}{\varepsilon_d + \varepsilon_m}} \tag{3.25}$$

and must be matched to the parallel component of the incident wave vector, $\vec{k}_0$.

Different types of surface modes can exist depending on the permittivity values on either side of the interface, which for metals is a function of frequency. Values for k_x' were calculated for a gold-air interface for different values of ω and plotted in Figure 3.2. The dashed blue line is known as the *light line* and represents the linear dispersion relation for a free space electromagnetic wave $\omega = ck_0$.

For a planar interface at a frequency below $\omega_{sp} = \omega_p/\sqrt{1+\varepsilon_d}$, known as the *surface plasmon frequency*, the permittivity of a metal is characterized by $\varepsilon_m' < -\varepsilon_d$. This leads to a type of surface mode known as *propagating surface plasmons* (PSPs). At higher frequencies, other surface modes such as *localized surface plasmons* (LSPs) and *Brewster's modes* exist due to the frequency-dependent nature of permittivity. An in-depth discussion of these modes can be found in [45], however this thesis will focus on the properties of PSPs at THz frequencies. At low frequencies in the THz region, PSPs behave like free space waves and have a propagation constant close to, but larger than, k_0. Therefore, light cannot couple into PSPs (and vice versa). For large wave vectors, the value of ω asymptotically approaches ω_{sp}.

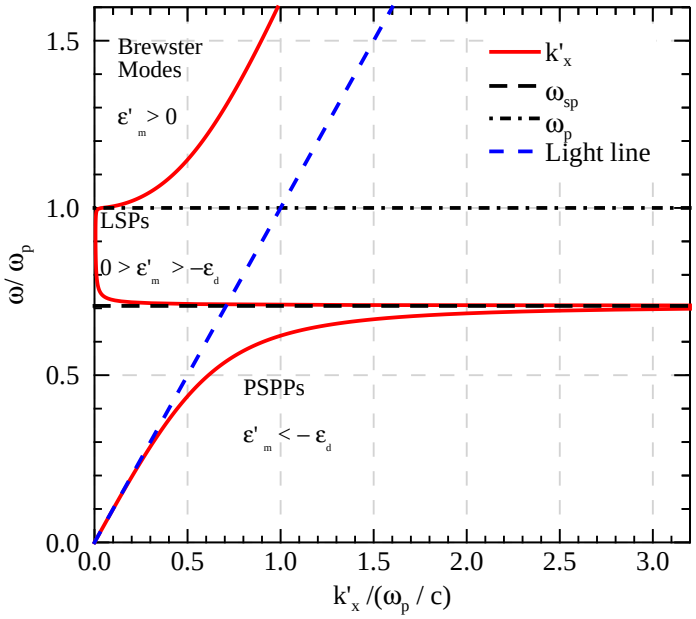

Figure 3.2: The surface plasmon dispersion relation (solid) written as $\omega(k'_x)$. k'_x was generated for various frequencies using permittivity values for Au calculated using Drude model parameters (Section 2.4). The dispersion relation can be separated into different modes for different values of ε_d and ε_m. Surface modes that propagate along the surface (PSPPs) exist for $\varepsilon_d < \varepsilon_m$ (solid, red, lower right) and have a wave vector that is greater than a free space electromagnetic wave (dashed, blue).

As a final note, a *polariton* is defined as the coupled state between an elementary excitation and a photon [45]. A distinction can now be made between the term "surface plasmon", which refers to a type of electromagnetic surface mode, and a "surface plasmon polariton", which is the coupled state between incident light and the surface plasmon mode. This thesis will use the term surface plasmon polariton (SPP) to refer to a propagating surface plasmon polariton (PSPP).

3.3.1 Excitation of PSPPs with Surface Gratings

Different coupling mechanisms exist depending on the particular application. These include attenuated total internal reflection techniques using prisms (e.g., the Otto and Kretschmann configuration), point defects, surface roughness, and, of particular interest

to bullseye lenses, surface gratings [45].

Diffraction gratings are structures with periodic surface corrugations that scatter light with specific interference conditions (Figure 3.3) [6]. The location of diffracted maxima are given by the grating equation

$$\lambda_g(\sin\theta_m - \sin\theta_i) = \pm m\lambda_0 \tag{3.26a}$$

or

$$k_0 \sin\theta_m - k_0 \sin\theta_i = \pm m k_g \tag{3.26b}$$

where $m = 1,\ 2,\ 3, \cdots$ describe the different diffracted orders at angles θ_m, λ_g is the grating period, and λ_0 is the incident wavelength at an angle θ_i. The grating equation has been re-written in terms of wavenumbers via $k = 2\pi/\lambda$. Note that the first term on the left is the component of the diffracted wave vector that is parallel to the surface $k_m^{\parallel} = k_0 \sin\theta_m$ and the second term is the component of the incident wave vector parallel to the surface $k_0^{\parallel} = k_0 \sin\theta_i$. Matching the parallel component of the diffracted wave vector to the surface plasmon wave vector $k_m^{\parallel} = k_x$ gives

$$k_x = k_0^{\parallel} \pm m k_g. \tag{3.27}$$

At normal incidence, $\theta_i = 0$ and $k_0^{\parallel} = 0$. Equation 3.27 can be simplified and arranged to find the required grating period,

$$\lambda_g = \pm m \lambda_{SP}, \tag{3.28}$$

where $\lambda_{SP} = 2\pi/k_x$ is known as the *surface plasmon wavelength*.

The efficiency of the coupling is directly related to the geometric parameters of the

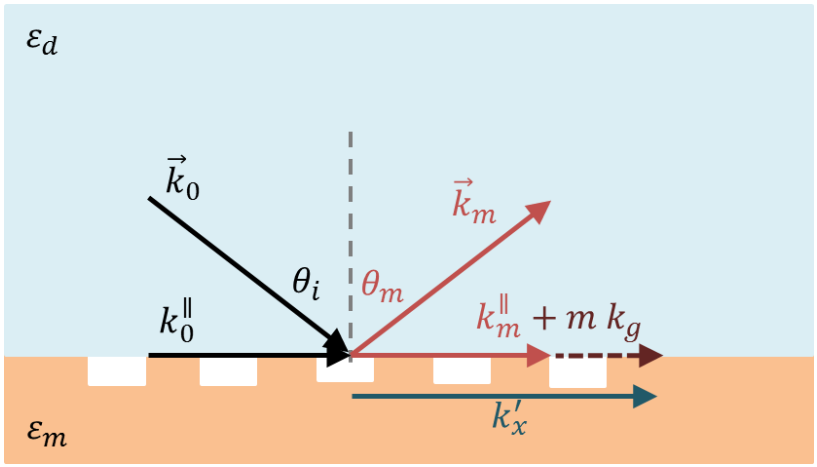

Figure 3.3: The coupling of an incident photon (black) to a SP mode (blue) with a diffraction grating. The grating vector, k_g, (brown) matches the parallel component of the diffracted wave (red) to the SP propagation constant, k_x'.

grating. Simulations using the Maxwell equation solver Lumerical FDTD Solutions were performed to optimize this coupling and will be further discussion in Chapter 5 [52]. This coupling process also occurs in the opposite manner allowing surface plasmons to radiate into the dielectric medium [50].

The use of surface gratings modifies the simple geometry of a planar interface as solved in Section 3.1 and, to be strict, SPPs would not have the same characteristics. For shallow surface structures (i.e., less than the incident wavelength) the nature of the mode is not substantially altered, however the coupling of the surface mode to incident photons has shown that radiative losses into the dielectric medium can affect the propagation length [45].

3.4 Surface Plasmons at Visible and THz Frequencies

It is instructive at this point to highlight the different length scales associated with visible and THz PSPPs. These differences arise due to the large magnitude of THz permittivity compared to its visible counterpart. A Lumerical multi-coefficient model (Appendix B) fit to data from Johnson and Christy [51] for $\lambda \in [500\text{ nm}, 700\text{ µm}]$ yields $\varepsilon_m = -11.7 + i1.2$ at $\lambda = 633.08$ nm. At THz frequencies, the complex permittivity of metals is orders of magnitude greater than in the visible, tending to that of perfect electrical conductor. For

example, using the Drude model parameters given in Section 2.4.1, the permittivity of Au at 325 GHz is $\varepsilon_m = -1.12 \times 10^5 + i2.24 \times 10^6$. The characteristic lengths for these permittivity values in the visible and THz regime are given in Table 3.1. Skin depths and propagation lengths have been calculated up to 500 GHz for the metals Cu, Al, Au, and Ag in air as shown in Figures 3.4 and 3.5

Table 3.1: The skin depth in the metal, δ_m, skin depth in the dielectric, δ_d, and propagation length, L, of visible and THz SPPs on a Au-air interface.

	λ (m)	δ_m (m)	δ_d (m)	L (m)
Visible SPPs	6.33×10^{-7}	$3.00 \times 10^{-8} \approx 10^{-2}\lambda$	$3.00 \times 10^{-7} \approx 0.5\lambda$	$1.00 \times 10^{-5} \approx 16\lambda$
THz SPPs	9.22×10^{-4}	$1.35 \times 10^{-7} \approx 10^{-4}\lambda$	$3.00 \times 10^{-1} \approx 10^{2}\lambda$	$3.30 \times 10^{2} \approx 10^{5}\lambda$

For noble metals at visible frequencies, PSPPs are typically characterized by strong confinement of their electromagnetic field near the interface (i.e., $\delta_d \approx 0.5\ \lambda$) with moderately long propagation lengths. Comparably, THz PSPPs extend far into the dielectric medium and have propagation lengths many orders of magnitude larger than the wavelength.

Low permittivity values in the visible leads to a large penetration within the metal with respect to the wavelength, which leads to increased coupling with the free charge density. In the THz region, δ_m is small with respect to the wavelength. Since only the material properties within approximately one skin depth significantly contribute to the operation of a plasmonic device, this allows for thin THz plasmonic devices [54].

While THz bullseye devices have been made using nano-techniques, this requires access to a nano-fabrication facility [30,34,54]. In addition, the metallic deposition depths required are large compared to typical applications at optical wavelengths. Since the required precision of a THz plasmonic lens scales with wavelength and is thus low when compared to an optical equivalent, it is possible to achieve the same relative accuracy at THz wavelengths using a micro-machining approach. This is further discussed in Appendix C.

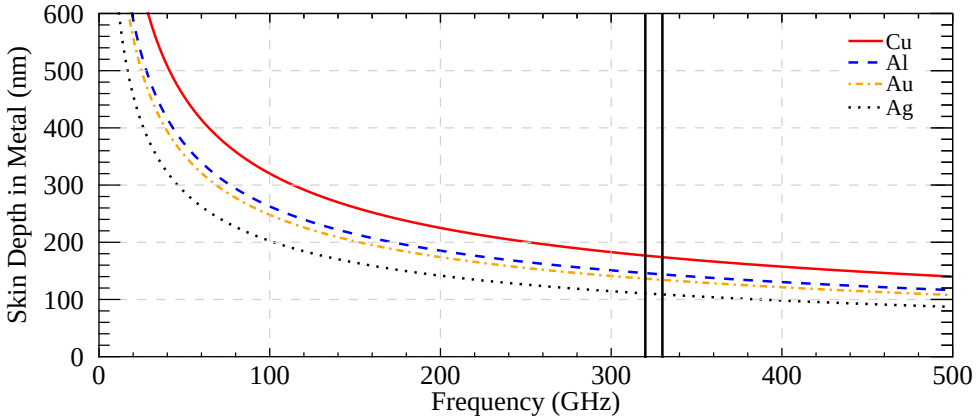

(a) The skin depth in metal, δ_m.

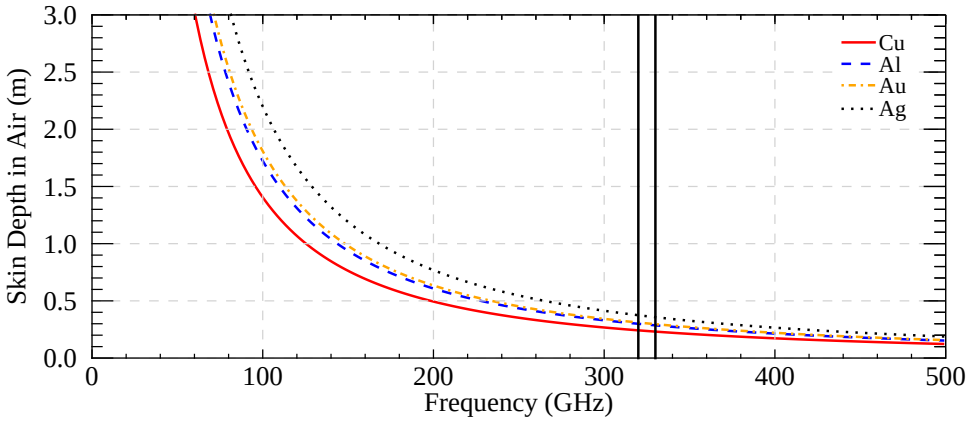

(b) The skin depth in air, δ_d.

Figure 3.4: Surface plasmon skin depths into Cu, Al, Au, and Ag and into the dielectric medium (air) in a section of the THz regime. The vertical band represents the tunable bandwidth of our THz line source (Section 6.1.1). The excited surface plasmons have little penetration into the metal and extend far into the dielectric.

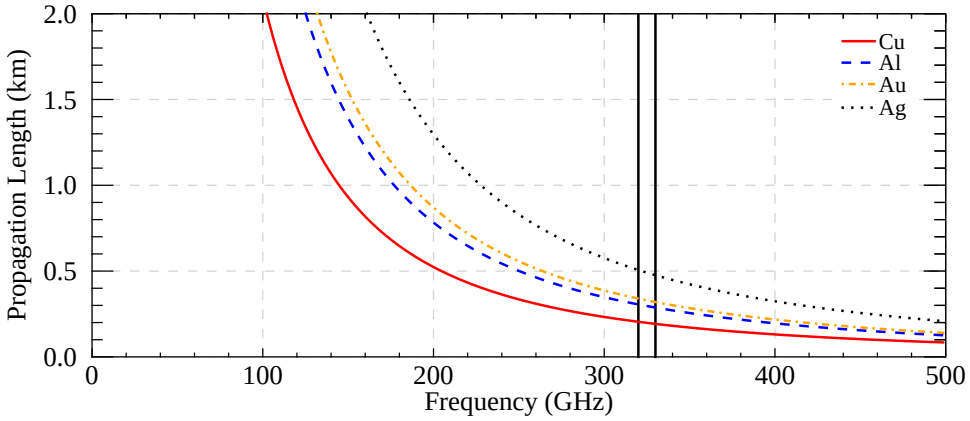

Figure 3.5: The propagation length of excited surface plasmons for the metals Cu, Al, Au, and Ag on an air interface. The vertical band represents the tunable bandwidth of our THz line source (Section 6.1.1).

Chapter 4

Transmission of Light Through Subwavelength Circular Apertures

A single subwavelength aperture plays an important role in the operation of high resolution near-field imaging systems (Section 1.2). The diffraction properties of subwavelength holes have been a source of discussion since their first observation by Grimaldi in 1665 and are still debated in contemporary theoretical and experimental studies [65–68]. Solutions to diffraction problems are mathematically challenging and analytical solutions in general do not exist. This chapter presents simple approximations that depend on the size of the incident wavelength relative to the size of the geometry of the problem.

4.1 Diffraction Regimes

The Huygens-Frensnel principle has classically been a powerful tool that describes the majority of diffraction effects [6]. This construction states that every point of a wavefront can be considered as a source of a secondary emission of spherical waves known as Huygen wavelets. The wavefront of a propagating wave of light at any instant is defined by the envelope of the wavelets. The resulting amplitude of the wave is the vector sum of the amplitude of all secondary waves. This theory was later mathematically formulated as Kirchhoff's scalar diffraction theory.

The simple case of an opaque screen with a single aperture of radius r at a distance L from a viewing screen was introduced in Section 1.1. Kirchhoff's theory can be reduced to useful approximate forms in the *near-field* (*Fresnel*) regime ($L < r^2/\lambda$) and *far-field*

(*Fraunhofer*) regimes ($L > r^2/\lambda$), where λ is the incident wavelength. Diffraction patterns of circular apertures that are large compared to the wavelength, i.e., $kr \gg 1$, where k is the wavenumber of the incident light, fall in the far-field regime and have intensity distributions described by the Airy pattern [12]. This model is valid up to $kr \sim 1$ [69].

4.2 Bethe's Transmission Efficiency

Kirchhoff's theory does not take into account the polarization of the incident light. In the extreme subwavelength regime, $kr \ll 1$, this basic scalar assumption fails and a full vectorial approach using Maxwell's equations is required, as addressed by Bethe in 1944 [16]. Bethe applied Maxwell's equations in an infinitesimally thin perfect electrical conductor with a single subwavelength aperture and presented two main predictions. The first was an expression for the power P_{out} transmitted through the aperture:

$$P_{out} = \sigma_{eff} I_i, \qquad \text{(W)} \quad (4.1)$$

where I_i ($\mathrm{W \cdot m^{-2}}$) is the incident intensity and σ_{eff} ($\mathrm{m^2}$) is the *effective diffraction cross section*. The effective diffraction cross section was calculated for polarized light with the electric field in the plane of incidence, perpendicular to the plane of incidence, and for unpolarized light. In all cases, the effective diffraction cross section for light at normal incidence is [16]

$$\sigma_{eff} = \frac{64}{27\pi} k^4 r^6 \propto \frac{d^6}{\lambda^4}. \qquad (\mathrm{m^2}) \quad (4.2)$$

The definition of transmission can be ambiguous in the technical literature due to different conventions used when normalizing the transmitted power. For clarity, this thesis will define *absolute transmission* T as the ratio of the transmitted power P_{out} to the total source power P_0:

$$T = P_{out}/P_0. \tag{4.3}$$

Another common representation of transmission is the *effective diffraction cross section normalized to the area of the aperture*,

$$\eta = \frac{\sigma_{eff}}{A_a} = \frac{P_{out}}{I_i A_a} = \frac{P_{out}}{P_{in}}, \tag{4.4}$$

which is equivalent to the ratio of the transmitted power to the power $P_{in} = I_i A_a$ incident on the aperture area A_a. This thesis will define η as the *transmission efficiency*. When $\eta = 1$, all of the light impinging on the aperture is transmitted. For $\eta > 1$, more power is transmitted than is incident on the hole (e.g., for $\eta = 2$ twice as much power is transmitted). Using Bethe's expression for σ_{eff},

$$\eta = \frac{\sigma_{eff}}{A_a} = \frac{64}{27\pi^2}(kr)^4 \propto \left(\frac{d}{\lambda}\right)^4. \tag{4.5}$$

Later, additions by Bouwkamp included higher order terms [70]:

$$\eta = \frac{64}{27\pi^2}(kr)^4 \left[1 + \frac{22}{25}(kr)^2 + \frac{7312}{18375}(kr)^4 + \cdots\right]. \tag{4.6}$$

Bethe's second prediction addressed the angular pattern that emerged from the aperture. The angular distributions in the far-field depend on the orientation of the polarization of the incident light relative to the direction that the pattern is measured. If a detector was scanned parallel to the polarization direction, the intensity is constant, whereas if scanned perpendicular to the polarization the intensity has an angular dependence of $\cos^2\theta$.

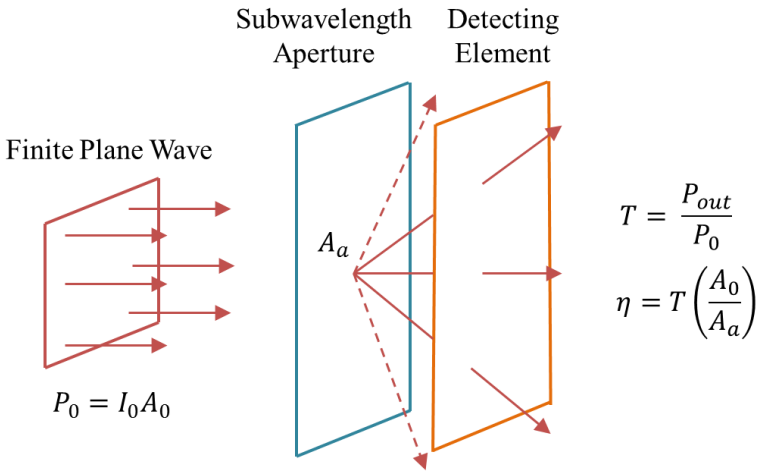

Figure 4.1: A finite plane wave incident on an aperture of area A_a in an opaque screen. The measured transmission, T, can be used to calculate the transmission efficiency, η.

4.2.1 Transmission Efficiency of a Plane Wave

An ideal plane wave is a monochromatic wave with wavefronts that are infinite, parallel surfaces of constant phase and amplitude that extend in a direction normal to the wave's propagation. Anticipating the discussion in Chapter 5 regarding numerical methods to solve Maxwell's equations, it is practical to consider a plane wave of finite extent and, consequently, finite power injected in an arbitrary region of interest (Figure 4.1). The power of a finite plane P_0 is the product of the intensity of the plane wave I_0 and its finite area A_0. The absolute transmission T of a plane wave incident on an aperture can be converted to a transmission efficiency by:

$$\eta = \frac{P_{out}}{I_0 A_a} = T\left(\frac{A_0}{A_a}\right). \tag{4.7}$$

Therefore, with the absolute transmission T, aperture area A_a, and the source area A_0, the transmission efficiency can be calculated.

4.3 Gaussian Beams

A Gaussian beam is a type of electromagnetic wave that is spatially localized along its axis of propagation, i.e., they are *paraxial*. Gaussian beams arise as solutions to the electromagnetic wave equation (Equation 2.4) by assuming solutions of the form given in Equation 2.15 and applying separation of variables. Paraxial approximations and a full derivation can be found in [71]. The main result is a wave with an intensity distribution given by

$$I(r,z) = I_0 \left[\frac{w_0}{w(z)}\right]^2 \exp\left[\frac{-2r^2}{w^2(z)}\right], \qquad (\mathrm{W}\cdot\mathrm{m}^{-2}) \quad (4.8)$$

where I_0 is the maximum beam intensity and $r = x^2 + y^2$ is the radial distance from the propagation axis.

Equation 4.8 represents an intensity distribution that is circularly symmetric in the transverse plane and falls off with a Gaussian cross-section. Figure 4.2 shows the main properties and parameters that describe a Gaussian beam. The beam propagates along the z-direction and has a minimum cross-sectional radius called the *beam waist* w_0 (m) at $z = 0$. The full cross-sectional width, $2w_0$, is known as the *spot size*. The radial size of any cross section along the axis of propagation is known as the *beam radius* $w(z)$ and is defined as the radial distance where the beam intensity falls to I_0/e. The beam radius is calculated at any point using

$$w(z) = w_0\sqrt{1 + \left(\frac{z}{z_R}\right)^2}, \qquad (\mathrm{m}) \quad (4.9)$$

where z_R is the *Rayleigh range*. The Rayleigh range is wavelength dependent and is given by

$$z_R = \frac{\pi w_0^2}{\lambda}. \qquad (\mathrm{m}) \quad (4.10)$$

At a distance of z_R, the beam radius increases by a factor of $\sqrt{2}$ and the cross sectional area

increases by a factor of 2. A related parameter is the *depth of focus*:

$$b = 2z_R. \qquad \text{(m)} \quad (4.11)$$

For a given wavelength, a focused beam with a small spot size has a short depth of focus, which increases the accuracy required when locating the image plane.

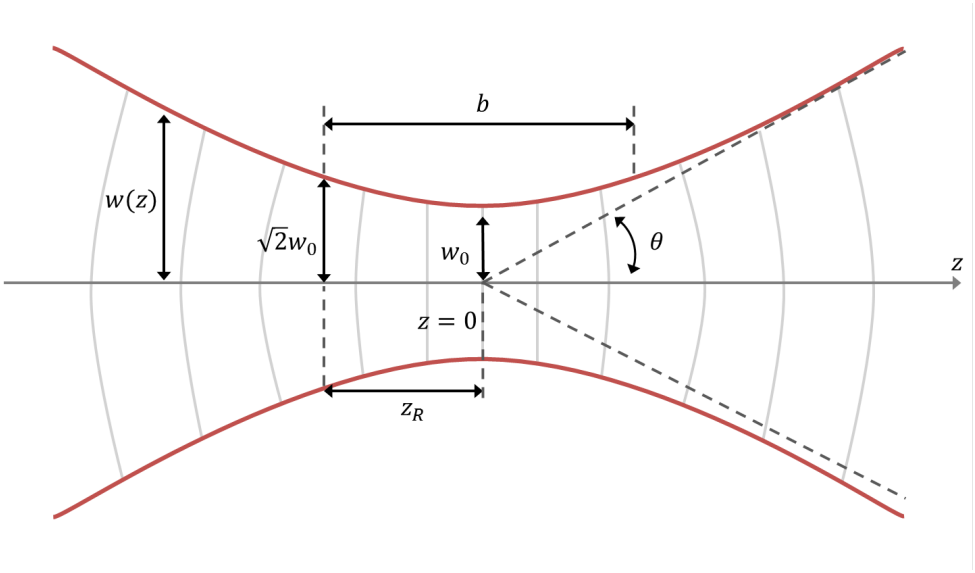

Figure 4.2: Diagram of the parameters that define the propagation of a Gaussian beam. The red line is the location where the intensity in the radial direction drops to I_0/e. The light grey lines show the curvature of the wavefront, which is planar at the location of the beam waist and become spherical as the beam diverges.

Far from the Rayleigh range, $z \gg z_R$, the approximated beam radius is given by

$$w(z) \approx \frac{w_0}{z_R} z. \qquad \text{(m)} \quad (4.12)$$

The beam width increases linearly and the resulting beam is cone-shaped with a divergence half-angle of

$$\theta = \frac{w_0}{z_R} = \frac{\lambda}{\pi w_0}. \qquad \text{(rad)} \quad (4.13)$$

Since the divergence half-angle is directly proportional to the wavelength, λ, and inversely

proportional to the beam waist, w_0, a beam with a tight spot size has increased divergence.

In general terms, the width of a function is defined as the location at which its dependent variable falls to a fraction of its maximum value. Common examples are the full-width at half-maximum (FWHM) and standard deviation σ of a Gaussian distribution. For the case of Gaussian beams, the radial distance where the beam intensity falls to I_0/e is the typical measure of width. However, it is useful to derive expressions that relate the beam radius $w(z)$ of a Gaussian beam to its FWHM.

The FWHM of the Gaussian beam occurs when the intensity is at half its maximum value:

$$\begin{aligned} \frac{1}{2} I_0 \left[\frac{w_0}{w(z)}\right]^2 &= I_0 \left[\frac{w_0}{w(z)}\right]^2 \exp\left[\frac{-2r^2}{w^2(z)}\right] \\ \frac{1}{2} &= \exp\left[\frac{-2r^2}{w^2(z)}\right] \\ \ln\left(\frac{1}{2}\right) &= \frac{-2r^2}{w^2(z)}. \end{aligned} \tag{4.14}$$

Since r is the radial distance from the axis of the Gaussian beam, it represents the half-width at half maximum, i.e., $r = \text{FWHM}/2$. Substituting this to the above equation gives

$$w(z) \approx 0.8493 \text{ FWHM}. \tag{4.15}$$

4.3.1 Beam Power

The total power P_0 carried by the beam is the integral of the intensity distribution at a given axial position z in the transverse plane:

$$
\begin{aligned}
P_0 &= \int I dA \\
&= \int_0^\infty I(r,z)\, 2\pi r\, dr \\
&= \int_0^\infty I_0 \left[\frac{w_0}{w(z)}\right]^2 \exp\left[\frac{-2r^2}{w^2(z)}\right] 2\pi r\, dr \\
&= I_0 \left[\frac{w_0}{w(z)}\right]^2 \int_0^\infty \exp\left[\frac{-2r^2}{w^2(z)}\right] 2\pi r\, dr \\
&= 2\pi\, I_0 \left[\frac{w_0}{w(z)}\right]^2 \int_0^\infty r \exp\left[\frac{-2r^2}{w^2(z)}\right] dr.
\end{aligned} \tag{4.16}
$$

Letting

$$
\begin{aligned}
u &= -\left(\frac{2r^2}{w(z)^2}\right) \\
du &= -\left(\frac{4r}{w(z)^2}\right) dr \\
dr &= \left(\frac{w(z)^2}{4r}\right) du,
\end{aligned}
$$

the integral can be simplified to

$$
\begin{aligned}
P_0 &= -2\pi\, I_0 \left[\frac{w_0}{w(z)}\right]^2 \int_0^\infty r \left(\frac{w(z)^2}{4r}\right) \exp[u]\, du \\
&= -\frac{1}{2}\pi\, I_0 w_0^2 \int_0^\infty \exp[u]\, du \\
&= -\frac{1}{2}\pi\, I_0 w_0^2 (0-1) \\
&= \frac{1}{2}\pi\, I_0 w_0^2.
\end{aligned} \tag{4.17}
$$

Note that this result is independent of z since the total power in any transverse plane is conserved.

4.3.2 Transmission Efficiency of a Gaussian Beam

To calculate the transmission efficiency $\eta = P_{out}/P_{in}$ through an aperture under Gaussian beam illumination, the power incident on an aperture P_{in} is no longer given by the simple expression for a plane wave (Section 4.2.1) since intensity distribution of a Gaussian beam falls off as a function of radial distance. Using Equation 4.17, the intensity distribution of a Gaussian beam can be rewritten in terms of the total beam power P_0 as

$$I(r,z) = \frac{2P_0}{\pi w(z)^2} \exp\left[\frac{-2r^2}{w^2(z)}\right]. \tag{4.18}$$

The power within a circle of radius r is given by

$$\begin{aligned} P(r,z) &= \int_0^r I(r,z) 2\pi r' \, dr' \\ &= \int_0^r \frac{2P_0}{\pi w(z)^2} \exp\left[\frac{-2r'^2}{w^2(z)}\right] 2\pi r' \, dr' \\ &= P_0\{1 - \exp[-2r^2/w^2(z)]\}. \end{aligned} \tag{4.19}$$

Figure 4.3 shows the fractional power contained in a Gaussian beam for a given radii normalized to the beam waist. Approximately 86% of the total beam power is contained within a circle of radius $r = w(z)$ and approximately 99% within a circle of radius $r = 1.5w(z)$.

The transmission efficiency through an aperture illuminated by a Gaussian beam can now be calculated by using $P_{in} \equiv P(r,z)$, where the radial coordinate r is equivalent to the aperture radius, when normalizing the measured output power in Equation 4.4.

4.4 Material Thickness

Waveguide theory can be applied to a circular aperture to describe how the power transmitted depends on the material thickness, t. Consider a hollow, cylindrical waveguide consisting of perfectly conducting walls surrounding a lossless interior (Figure 4.4). By

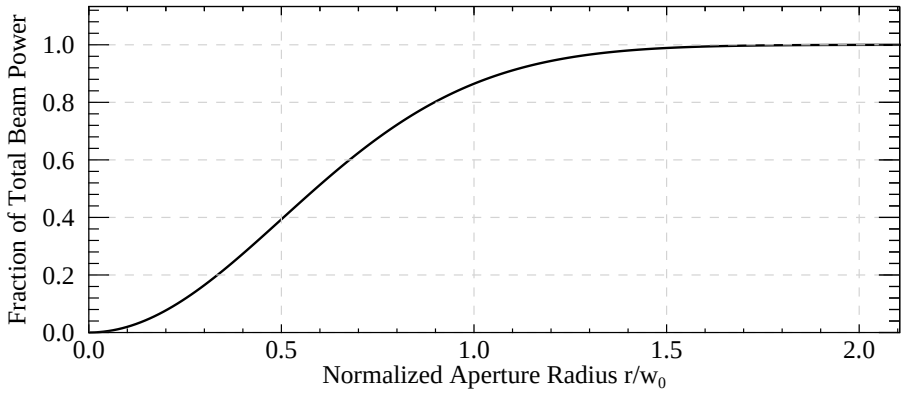

Figure 4.3: The fraction of total Gaussian beam power as a function of the normalized aperture radius.

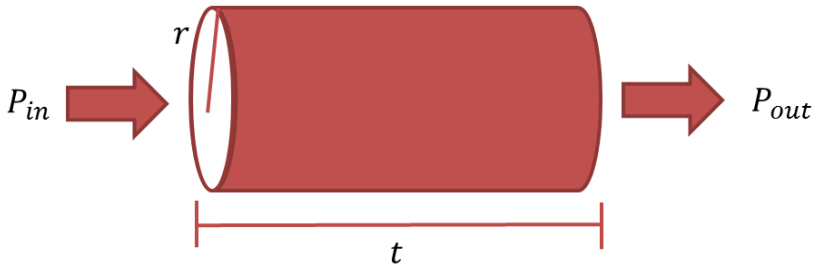

Figure 4.4: A simple cylindrical waveguide of radius r and thickness t.

assuming time-harmonic variation and solving Maxwell's equations in cylindrical coordinates, it can be shown that the dominate mode that exists in the waveguide (i.e., the mode with the longest wavelength at which light can propagate) is the TE_{11} mode [72]. The cutoff wavelength λ_{co} for this mode, which defines a transition where longer wavelengths become exponentially attenuated, is given by

$$\lambda_{co} = \frac{2\pi r}{1.84}, \tag{4.20}$$

where 1.84 is the first root of the derivative of the first order Bessel function. The attenuation of average power within the waveguide as a function of the distance z along the central axis is

$$P = P_{in} \exp(-2\alpha z), \tag{4.21}$$

where P_{in} is the power incident on the front waveguide and the amplitude attenuation constant, α, is given by

$$\alpha = \frac{2\pi}{\lambda_0} \sqrt{\left(\frac{\lambda_0}{\lambda_{co}}\right)^2 - 1}. \tag{4.22}$$

Applying this analogy to a circular aperture cut in a substrate of thickness t, the effect of the thickness on the transmitted power $P = P_{out}$ is

$$P_{out} = P_{in} \exp(-2\alpha t). \tag{4.23}$$

It should be noted that for real metals, λ_{co} is increased by taking into account the metallic skin-depth, as the electromagnetic fields will penetrate inside the walls of the waveguide. However, as noted in Section 3.4, the skin depth at THz frequencies is on the order of 100 nm and metals begin to behave as perfect electrical conductors [1].

4.5 Validity of Approximations

Both Bethe's theory for subwavelength apertures and the treatment of an aperture as a cylindrical waveguide are useful approximations that quantify the transmitted power as a function of aperture size and material thickness. The regimes in which both theories are valid were briefly discussed in the preceding sections. To properly apply these approximations to the results of simulations or experimental observations, it is important to explicitly state their respective cutoff wavelengths for a given aperture diameter d (or, alternatively, their cutoff diameters for a given incident wavelength λ).

Bethe's theory is valid in the extreme subwavelength region defined as $kr \ll 1$. The corresponding cutoff wavelength $\lambda_{co,b}$ and diameter $d_{co,b}$ are

$$\lambda_{co,b} \gg \pi d \qquad \text{and} \tag{4.24a}$$

$$d_{co,b} \ll 0.318\lambda\,. \tag{4.24b}$$

Waveguide theory is valid below the cutoff condition

$$kr = 1.84, \tag{4.25}$$

which corresponds to a cutoff wavelength λ_{co} and a cutoff diameter of

$$\lambda_{co} \geq 1.707d \qquad \text{and} \tag{4.26a}$$

$$d_{co} \leq 0.586\lambda\,. \tag{4.26b}$$

Figure 4.5 shows a plot of the aperture cutoff diameter as a function of wavelength. The cylindrical waveguide approximation is valid below the dashed line (including the blue and green regions). Bethe's theory, with the additions made by Bouwkamp, are valid below the solid line (green). Consider the THz microscope described in Section 1.4 with a THz source that emits a predominately Gaussian beam with a a frequency from 320-330 GHz, corresponding to wavelengths of 908-937 μm. This is represented as the vertical band in Figure 4.5. Bethe's theory would be valid for an incident wavelength of 908 μm for diameters well below 289 μm. Apertures with a diameter less than 532 μm will be subject to the power losses given by Equation 4.23.

4.6 Simulated Transmission Through a Circular Aperture

Although the equations that govern electromagnetic phenomena are well established, full theoretical approaches are difficult to solve. To address this, different numerical meth-

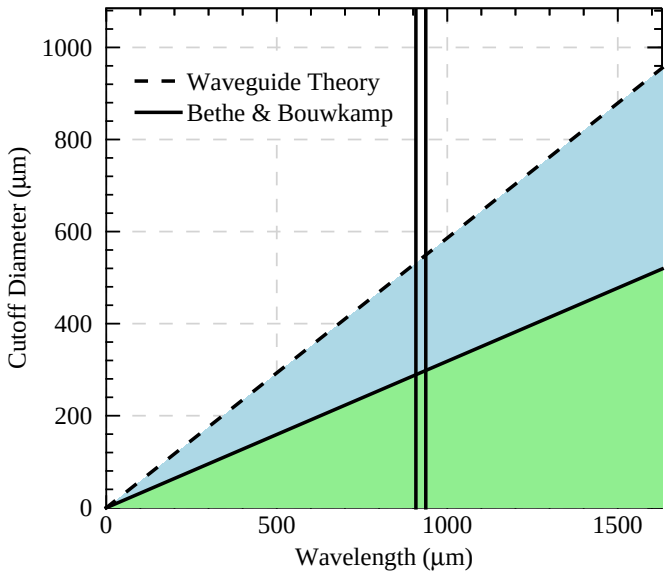

Figure 4.5: Regions in the diameter-wavelength space that are valid for Bethe's approximation for subwavelength transmission (below the solid line, green) and for waveguide theory (dashed line, blue and green). The vertical band represents the tunable bandwidth of our THz line source.

ods have been used to calculate the transmitted power as a function of aperture diameter, thickness, and wavelength [67, 73–75]. In this thesis, the finite-difference time-domain (FDTD) method was used to simulate the optical response of single apertures using Lumerical FDTD Solutions [52]. More details about this software, including common simulation consideration, testing of numerical convergence, and a full list of simulation parameters, can be found in Appendix B. Simulations were performed with a linearly polarized plane wave over a bandwidth of 722-1122 μm for a practical range of aperture diameters and thicknesses that could be used in a THz near-field imaging configuration.

To verify that cylindrical waveguide theory is a valid method to calculate power losses as a function of material thickness, an aperture with a diameter of $d = 300$ μm was simulated for thicknesses ranging from 60-300 μm (Figure 4.6). Note that the simulated wavelength range is above the waveguide cutoff wavelength of $\lambda_{co} = 512$ μm (Equation 4.26a).
The power transmitted at 922 μm was taken from this data set and plotted as a function of

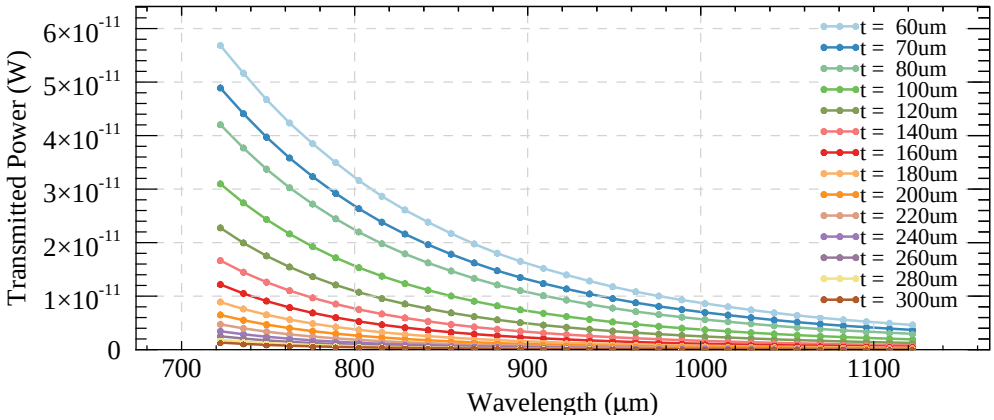

Figure 4.6: Simulated power transmission through 300 µm diameter apertures in a perfect electrical conductor of varying thickness. Circles denote simulated data points.

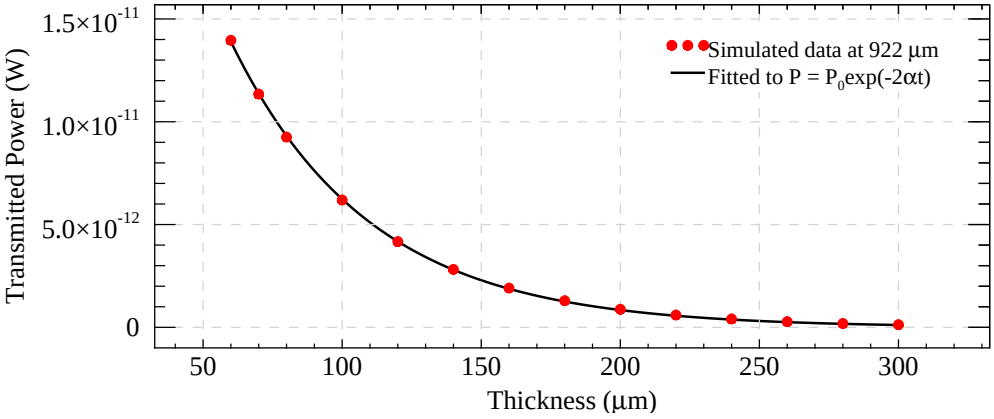

Figure 4.7: Simulated transmitted power of a $\lambda = 922$ µm plane wave through a 300 µm diameter aperture in a perfect electrical conductor of varying thickness. An exponential fit was made to the simulated data (solid line).

substrate thickness, as shown in Figure 4.7. For light of wavelength $\lambda = 922$ µm incident on an aperture of diameter $d = 300$ µm, the amplitude attenuation constant predicted by Equation 4.22 is $\alpha \approx 10.21\ \text{mm}^{-1}$. A fitted exponential function with the form of Equation 4.21 gave an amplitude attenuation of $\alpha = 10.02 \pm 0.04\ \text{mm}^{-1}$, a 2% difference, demonstrating that FDTD Solutions reasonably simulates a circular aperture as a cylindrical waveguide and that the equations given in Section 4.4 can be used as a good approximation for the thickness dependence on transmission. A full convergence test of various settings

in Lumerical FDTD Solutions, including mesh and simulation region size, would provide more accurate results with a better estimate of the absolute error in the simulated value of α.

To examine how the transmission efficiency varies as a function of diameter and wavelength, apertures with a thickness of 100 µm and diameters from 100-600 µm were simulated and the transmission efficiency was plotted as a function of d/λ. A subset of this data is shown in Figure 4.8, where the diameter has been expressed as the ratio t/d. As expected, the transmission efficiency approaches 1 in the small wavelength limit. For each simulated diameter, a peak in the transmission efficiency is observed. Similar peaks have been observed in subwavelength slits for incident light with a polarization perpendicular to the slit edge [76–78]. The origin of this phenomenon was first theoretically described by Takakura as a result of Fabry-Pérot-like resonances due to standing wave patterns formed within the slit [76]. In the context of subwavelength circular apertures, incident linear polarized light is not perpendicular to the all of the aperture edge, leading to lower resonant values of η compared to resonances within slits [67]. It is also noted that the peak shifts to smaller wavelengths for an increased relative thickness t/d, is in agreement with other numerical calculations [67, 73, 74].

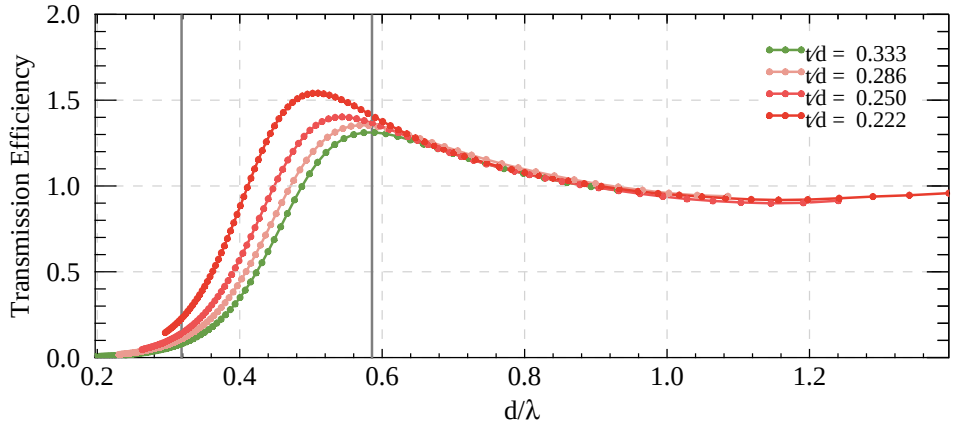

Figure 4.8: The transmission efficiency of a 100 µm thick subwavelength circular aperture of various diameters plotted as function of d/λ. Vertical lines represent the cutoffs for Bethe's theory and the waveguide approximation.

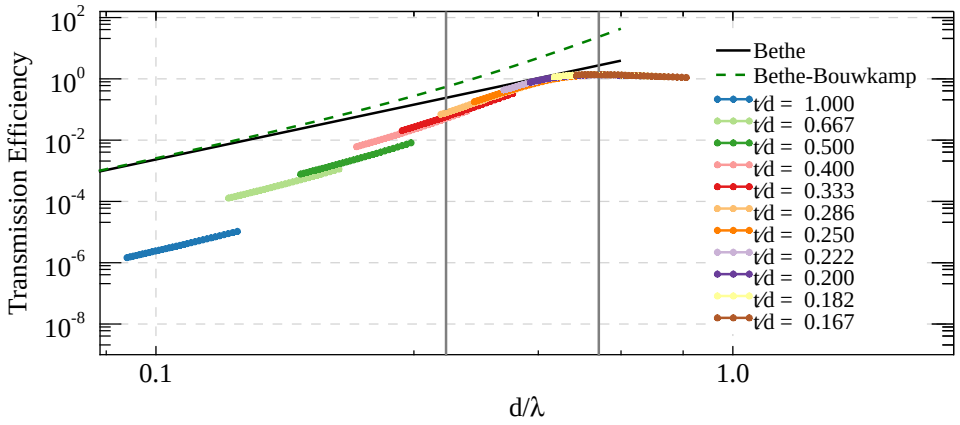

Figure 4.9: A log-log plot of the transmission efficiency of $t = 100$ µm thick apertures for various radii, expressed as the relative thickness t/d, compared to Bethe's theory. Vertical lines represent the cutoffs for Bethe's theory and the waveguide approximation.

Figure 4.8 was plotted on a log-log scale to verify Bethe's predicted $(d/\lambda)^4$ dependence on the transmission efficiency. The slope of the curves below the cutoff $d/\lambda \approx 0.3$ was then calculated. Bethe's prediction is better approximated for small (d/λ) values. E.g., for $t/d = 1.00$ ($d = 100$ µm), the fitted slope was found to be 4.56 ± 0.01. This increases to 6.33 ± 0.03 for $t/d = 0.333$ ($d = 300$ µm). In all cases, Bethe's theory overestimates the transmission efficiency for thick apertures and is a more accurate approximation as the relative thickness vanishes.

These numerical calculations highlight the complicated nature of diffraction theory outside of the regions where simple approximations can be applied. For a THz near-field imaging configuration with an operational wavelength of $\lambda = 922$ µm and a subwavelength aperture with a modest diameter of $d = 300$ µm, the ratio $d/\lambda \approx 0.3$ allows for the attenuation due to thickness to be reasonably approximated by waveguide theory. However, this wavelength and diameter combination exists on the edge of where Bethe's theory can be applied and numerical simulations are required to calculate the transmission efficiency.

Chapter 5

The Bullseye Plasmonic Lens

The phenomenon of extraordinary transmission through subwavelength circular apertures has been widely attributed to the resonant interaction of incident light with surface plasmon modes [17, 79]. As discussed in Section 3.3, light incident on a diffraction grating with a period that is similar or commensurate with the wavelength couples light into SPPs. When an aperture is surrounded by an annular grating, a configuration known as a bullseye plasmonic lens, the excited SPPs propagate radially inwards and outwards along the surface. Surface waves travelling towards the centre of the structure result in a large enhancement of the electric field above the aperture and, consequently, transmission efficiencies are orders of magnitude larger than expected from standard diffraction theory [17, 22, 27, 80, 81]. This has raised interest in the use of bullseye lenses at visible wavelengths for subwavelength imaging techniques and for high-density optical data storage [20–22, 74, 82].

Bullseye lenses typically have two main types of cross-sectional profiles. The surface can be patterned with grooves/indentations, as shown in Figure 5.1(a), or with ridges/protrusions, as shown in Figure 5.1(b). These models are parameterized as follows. The aperture is defined by its diameter, d, and its thickness, t. Let N be the total number of grooves/ridges and $i \in \{1, 2, \ldots, N\}$ be the index number of the feature. The distance a is measured from the centre of the aperture to the centre of the first groove/ridge. For regularly spaced surface features, the period, p, is the centre to centre spacing between grooves/ridges. The radial position, r_i, is measured from the centre of the aperture to the centre of surface feature i. The depth/height of the groove/ridge is denoted by s and the width by w.

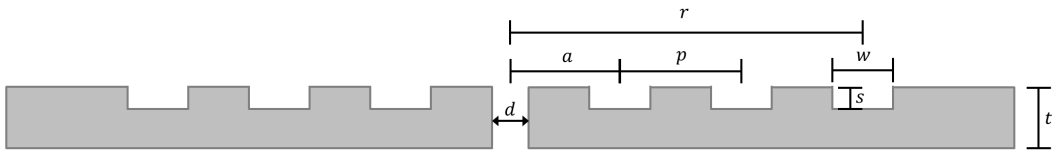

(a) Grooves (or indentations)

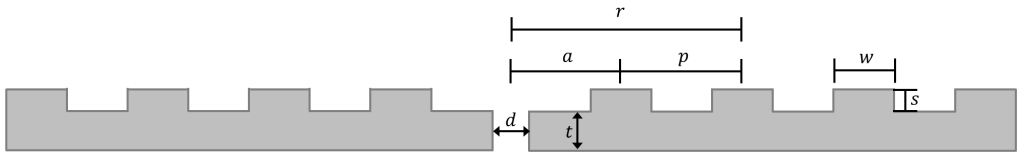

(b) Ridges (or protrusion)

Figure 5.1: The definition and cross-sectional profile of the two types of bullseye lenses discussed in this thesis.

The transmission process through bullseye lenses can be broken into three independent steps: coupling of the incident light into SPPs, evanescent transmission through the aperture, and coupling back into the radiation field [22]. This chapter begins with a systematic examination of the performance of different grating structures using Lumerical FDTD Solutions (Appendix B) [52]. These devices are optimized for enhanced transmission at a frequency of 325 GHz ($\lambda = 922$ μm), coinciding with the desired operational frequency of the THz imaging configuration described in Section 1.4. The performance of various bullseye designs are quantified in terms of their *transmission efficiency*, η, as discussed in Sections 4.2.1 and 4.3.2. A useful figure of merit is the *enhancement factor*, G, defined as [20]

$$G = \frac{\eta_{be}}{\eta_{ap}}, \tag{5.1}$$

where η_{be} and η_{ap} are the transmission efficiencies of a single aperture of the same thickness and diameter with and without gratings, respectively. If the value of η_{be} is larger than unity, then more power is transmitted through the aperture than is directly incident.

Attention will then be turned to output diffraction gratings, which have been shown

to modify the beam profile emitted from the plasmonic lens such that the output beam is focused/collimated for distances of several wavelengths [3,83,84]. Two final manufactured devices and their simulated response are then presented. A discussion of the fabrication procedure can be found in Appendix C.

5.1 Input Groove Optimization

The wavelength of light that is resonantly excited is mainly determined by the periodicity of the grating. Numerical and experimental studies have shown that other structural parameters can be chosen for optimized coupling of incident light with surface plasmon modes [85–88]. In 2010, Mahboub et al. explored, both experimentally and theoretically, the structural parameter space of a visible-frequency bullseye lens with input surface grooves, demonstrating that the parameters describing the grating are interlinked and that simple scale laws can be used as "rules of thumb" when designing a bullseye lens [88]:

$$\begin{aligned} \lambda &\approx 1.1p & \frac{w}{p} &\approx 0.5 \\ \frac{s}{w} &\approx 0.4 & \frac{s}{p} &\approx 0.2. \end{aligned} \tag{5.2}$$

Since the optical properties of metals at visible frequencies differ from those in the THz regime (Section 2.4.1), a perfect electrical conductor with input grooves was simulated using Lumerical FDTD Solutions [52]. The above relationships were used to determine initial groove parameters for a resonant wavelength of $\lambda_R = 922$ μm and are given in Table 5.1. Each parameter was then swept over a range of values to optimize the transmission efficiency with grooves illuminated by a linearly polarized plane wave. While a thin substrate increases the power transmitted through the aperture (Section 4.4), a large thickness of 1000 μm was intentionally chosen to accommodate a sufficient span of groove depths.

In Appendix B.2, it is shown that simulations converged for a mesh size of 19 μm in

Table 5.1: Initial groove parameters chosen via Equations 5.2 and the final, optimized parameters found using Lumerical FDTD Solutions (distances in μm). Note that an increasing number of grooves and a thinner aperture leads to further enhancement (see text). A full list of the simulation parameters can be found in Appendix B.4.

Input Face		Initial Parameters	Optimized Parameters
Type	–	Groove	Groove
Number of Features	N	4	6
Initial Distance	a	839	1332
Period	p	839	890
Width	w	419	445
Depth	s	168	134

the xy-direction and 4 μm in the z-direction. For optimization of groove parameters, a mesh size of 10 μm was chosen in all directions as a tradeoff between acceptable error and computation time. At this point in the analysis, it was assumed that the error in any optimized parameter, and consequently, the error in resonant peak wavelength, λ_R, was approximately on the order of the mesh size, which was chosen to be 10 μm.

In the following sections, the method used to optimize each of the bullseye design parameters is discussed.

Period Sweep

The model given in Table 5.1 was simulated for periods from 860-940 μm. The recorded transmission efficiency is shown in Figure 5.2. For $p = 890$ μm, a transmission peak was observed at $\lambda = 922$ μm. To compare this result with the basic scale laws in Equation 5.2, the peak wavelength was found for each period by interpolating 1000 points over the simulation bandwidth and locating the wavelength with a maximum transmission efficiency. The ratio λ_R/p was calculated for each curve. The mean and standard deviation determined from the λ_R/p value from each curve is $\lambda_R/p = 1.041 \pm 0.004$. For a desired $\lambda_R = 922$ μm, this corresponds to a period of $p = 886 \pm 3$ μm. A shift in the resonant wavelength could be attributed to the mesh precision of 10 μm.

Note that while the transmission efficiency at 922 μm for a groove period of 890 μm

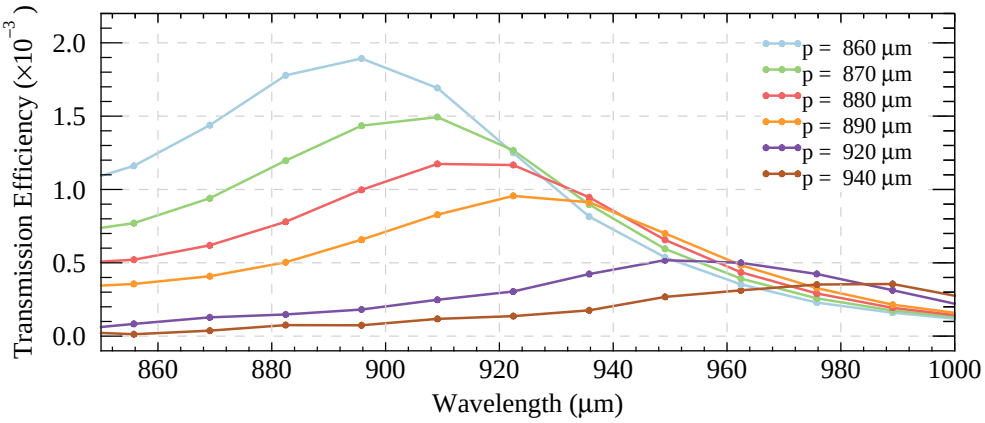

Figure 5.2: Simulated transmission efficiency of a bullseye structure with input grooves of varying periodicity. Points represent simulated values.

is lower than for periods from 860-880 μm, the smaller resonance at 922 μm could be attributed to the remaining groove parameters being unoptimized. For the remaining parameter sweeps, the period was set to 890 μm.

Number of Grooves Sweep

The number of grooves was initially set to 4 to reduce the size of the simulation volume and, consequently, simulation times. To ensure that the resonant wavelength did not change with an increased number of grooves, the number of features was swept from 1-6, as shown in Figure 5.3(a). Strong transmission resonances were observed for 3-6 grooves. For each groove, the ratio λ_R/p was $\approx$ 1.04 mm, in agreement with the results from the previous section. The transmission efficiency was then plotted at 922 μm as a function of the number of grooves (Figure 5.3(b)). A parabolic fit was made, demonstrating the transmission increases proportionally with N^2 dependence. This could be attributed to the constructive interference of SPPs at the aperture. If each groove contributes a linear sum of amplitudes at the aperture, then the intensity at the aperture increases by the amplitude squared. Final bullseye designs were fabricated with 6 input surface features.

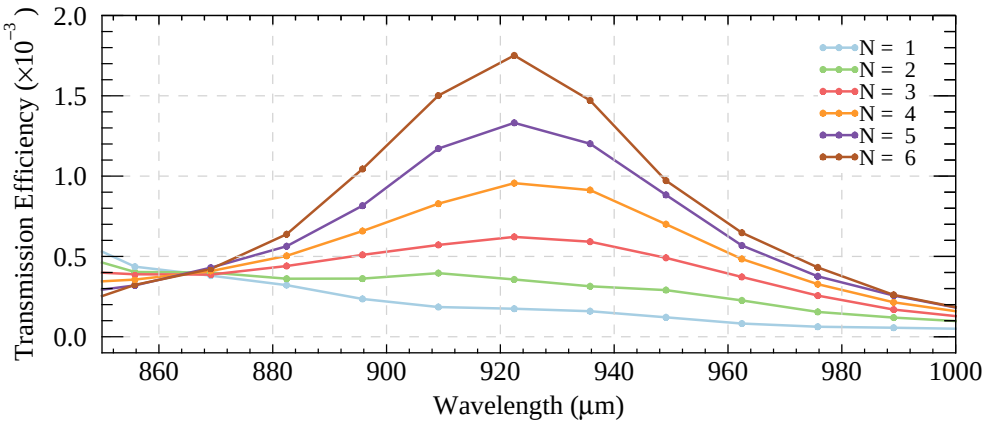

(a)

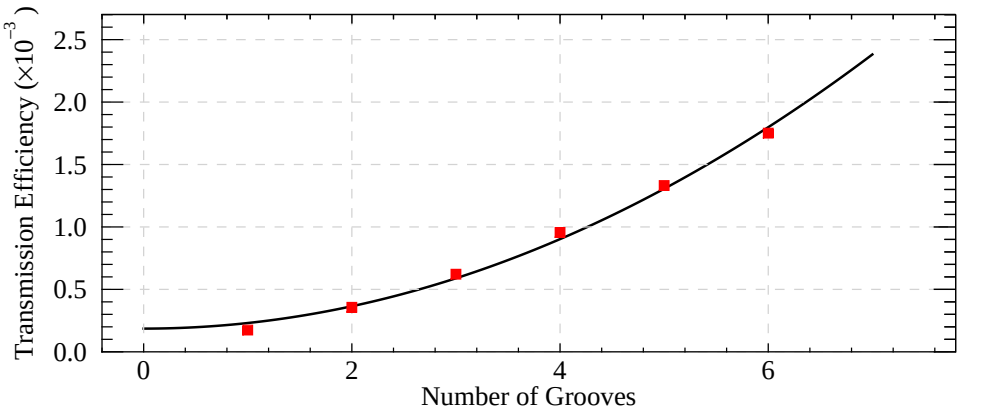

(b)

Figure 5.3: (a) Simulated transmission efficiency of a bullseye structure with an increasing number of input grooves. (b) Transmission values were taken at $\lambda = 922$ μm and plotted for an increasing number of input grooves, exhibiting N^2 dependence.

Groove Width Sweep

Following a similar methodology, a width sweep was simulated for ratios of w/p from 0.1 to 1.0 with a constant period of $p = 890$ μm (Figure 5.4(a)). Note that the simulations performed for this parameter sweep and in the remaining optimization simulations was set to $d = 445$ μm.

The data shown in Figure 5.4(a) was plotted at a wavelength of $\lambda = 922$ μm as a function of the relative width-to-period, as shown in Figure 5.4(b). A cubic spline was calculated over the data set and a maximum ratio of $w/p \approx 0.5$ was found. This ratio is in

agreement with the scale laws given in Equation 5.2.

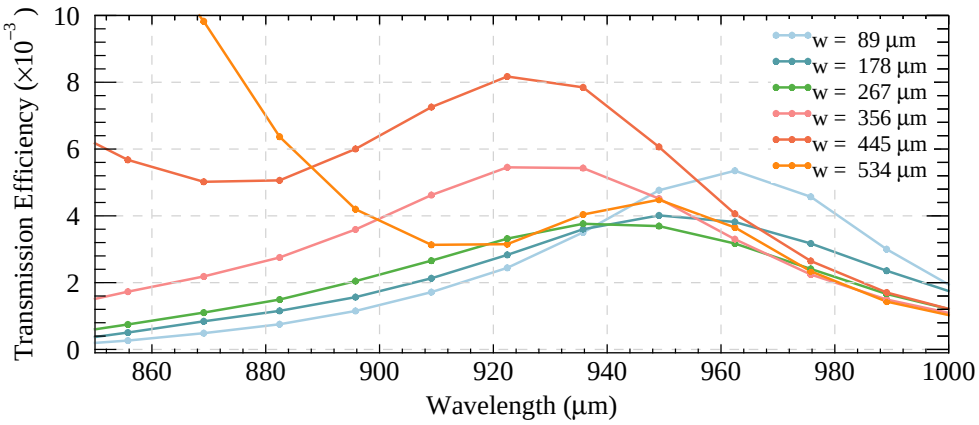

(a)

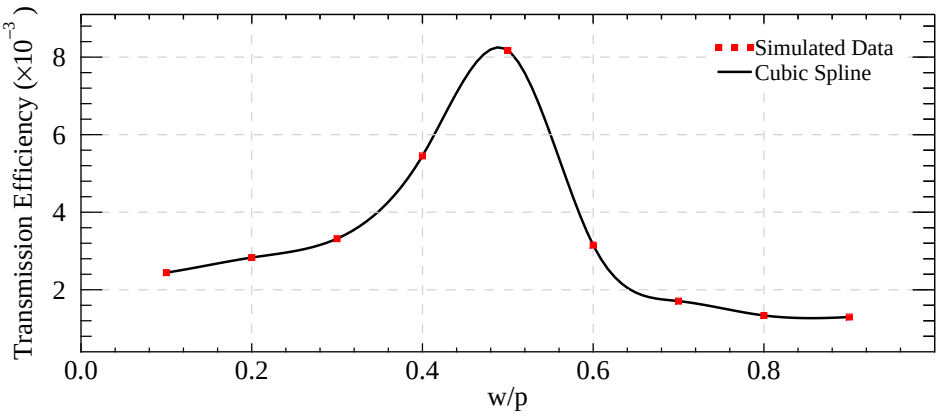

(b)

Figure 5.4: (a) Simulated transmission efficiency of a bullseye structure with grooves of constant period and varying width. (b) For each curve, the transmission efficiency was taken at $\lambda = 922$ μm and plotted as a function of the ratio w/p. A cubic spline was made over all points and a maximum ratio was found to be $w/p \approx 0.5$.

Groove Depth Sweep

The groove depth was then systematically varied for ratios of s/p from 0.1 to 1.0 with a constant period $p = 890$ μm and constant width of $w = 455$ μm (Figure 5.5(a)). The transmission efficiency at $\lambda = 922$ μm was plotted as a function of s/p and a maximum value of interpolated data was found for a ratio $s/p \approx 0.14$.

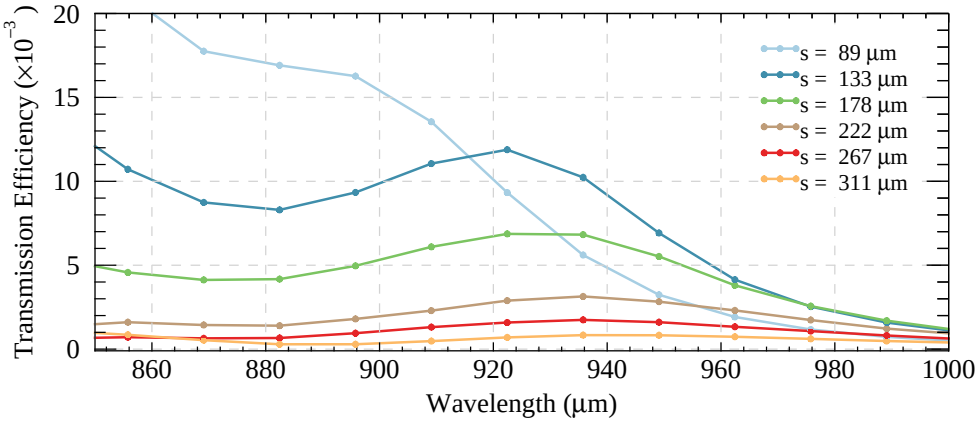

(a)

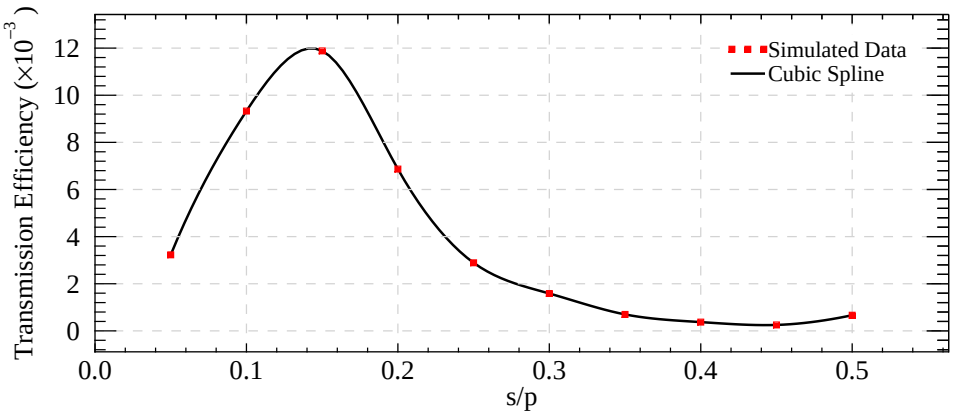

(b)

Figure 5.5: (a) Simulated transmission efficiency of a bullseye structure with grooves of constant period, constant width, and varying depth. (b) For each curve, the transmission efficiency was taken at $\lambda = 922$ μm and plotted as a function of the ratio s/p. A cubic spline was made over all points and a maximum ratio was found to be $s/p \approx 0.14$.

Material Thickness

The material thickness of the bullseye was then changed to verify that waveguide theory (Section 4.4) can be used to approximate the thickness dependence on the transmitted power, as shown in Figure 5.6(a). A slice of the data in Figure 5.6(a) was taken at 922 μm and plotted as a function of aperture thickness, as shown in Figure 5.6(b). An exponential fit using the same procedure described in Section 4.6 gave an amplitude attenuation constant of $\alpha_{be} = 3.97 \pm 0.03$ mm^{-1}.

For comparison, a single aperture with an identical diameter was simulated for corresponding thicknesses. The simulated amplitude attenuation constant of the single aperture was found to be $\alpha_{be} = 4.05 \pm 0.02$ mm^{-1}, which differs from the bullseye by approximately 1%. I.e., the thickness dependence of power transmitted through the bullseye is approximately independent of the surface corrugations.

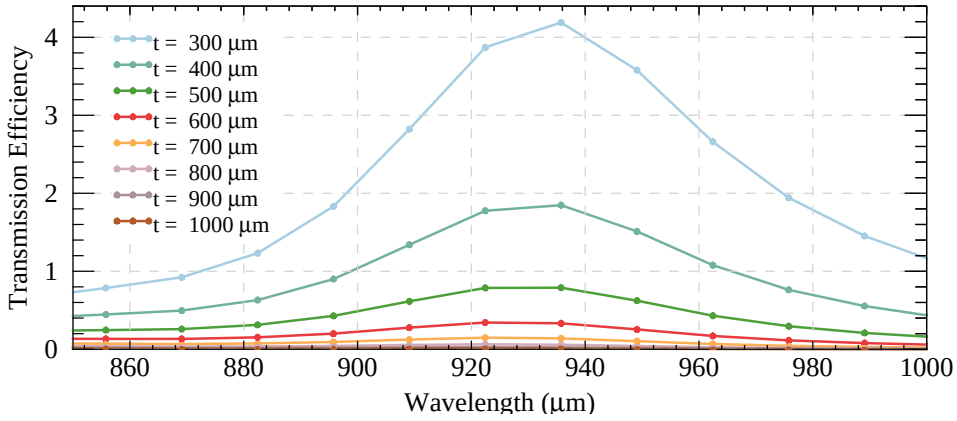

(a)

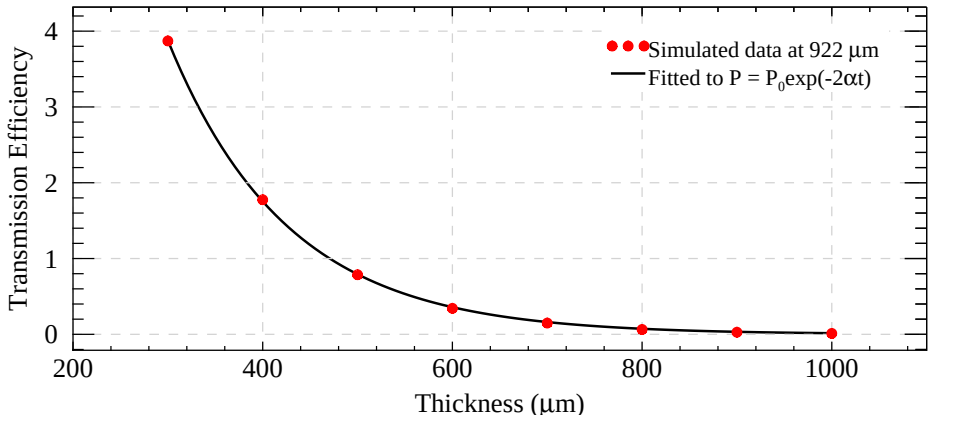

(b)

Figure 5.6: (a) Simulated transmission efficiency of a bullseye structure with varying aperture thickness. (b) An exponential fit was made to a slice of the data in (a) at 922 μm. The amplitude attenuation constant was fit to 4.05 ± 0.02 mm^{-1}.

Basic waveguide theory predicts the amplitude attenuation constant of the single aperture with a diameter of 445 μm to be $\alpha_{theo} = 4.7$ μm^{-1}. Both values have an error of approximately 15% compared to the theoretical value. This is larger than the 2% discrep-

ancy between theory and simulation in Section 4.6, which adopted a 4 μm simulation mesh. This optimization procedure was performed by simply choosing a uniform 10 μm mesh to reduce simulation times. As previously noted, it is expected that a finer mesh in z-direction would show improvement, however, these results show the anticipated trend.

The transmission enhancement, G (Equation 5.1), was then calculated by simulating apertures of identical diameters and thickness. As shown in Figure 5.7, the enhancement profile remains constant for all thicknesses. This is expected, as it implies that the transmission process through the aperture is independent of enhancement mechanism due to the input corrugations [22]. Therefore, once a transmission enhancement curve is generated for a given bullseye structure, cylindrical waveguide theory can be applied to the enhancement profile to predict the transmission loss as a function of thickness.

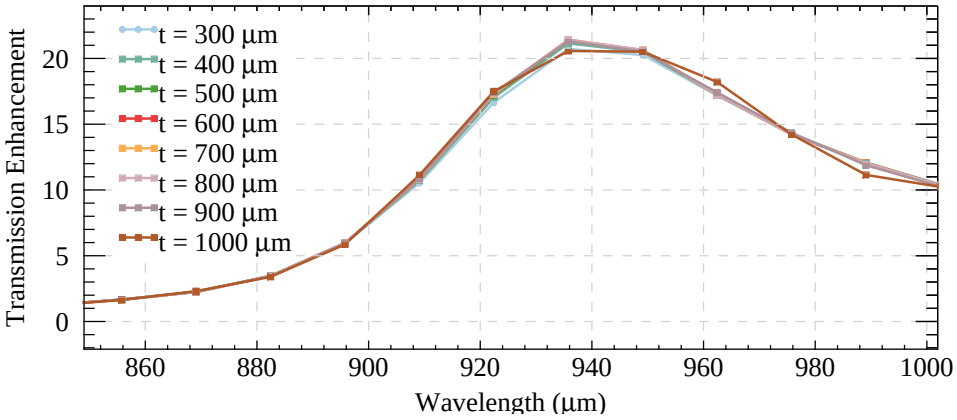

Figure 5.7: The transmission enhancement of the bullseye structure compared to a single aperture. Simulations were performed for substrates of different thicknesses. The transmission enhancement remains the same for all thicknesses.

Ridge Model and Distance to First Ridge

Since the difficulty to micromachine thin structures was unknown, the first fabricated design was an optimized groove model with a thickness of 300 μm was chosen to primarily determine if bullseyes could be fabricated by this method. The details of these results are not presented here, but ultimately, low transmission was observed because of strong

attenuate due to thickness.

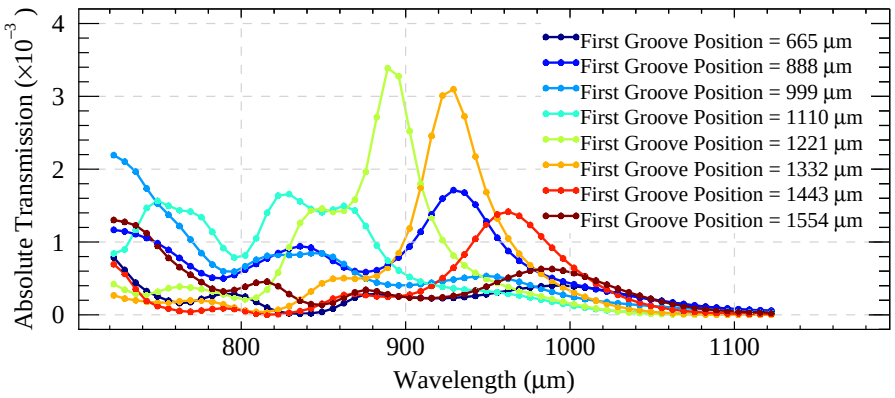

(a) The distance a swept from $0.75p$ to $1.75p$.

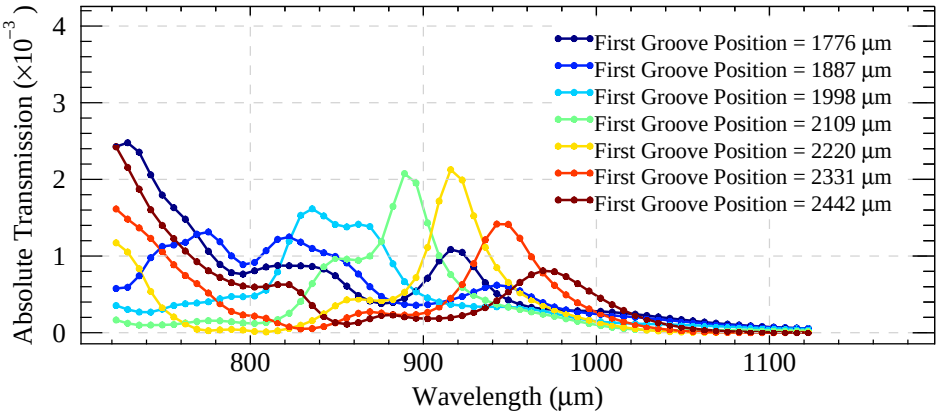

(b) The distance a swept from $2p$ to $2.75p$.

Figure 5.8: Increasing the distance from the centre of the aperture to the first ridge. Lower transmission resonances were observed at $\lambda = 922$ μm for $a = mp$ and larger resonances for $a = (2m + 1)p/2$, where m is an integer.

As a result, a ridge model was adopted that has a thin, internal aperture (Figure 5.1(b)). The optimized parameters used for groove designs were applied to the ridge model, where the groove depth s now represents the ridge height. In the ridge simulations that follow, modest variations in the ridge parameters of approximately 2 μm were made as the result of additional small optimization tests. These changes were within converged simulation mesh (4 μm in z and 19 μm in x and y) and were not expected to have a significant change in simulation results.

Table 5.2: The design of the bullseye model that was simulated for Gaussian beams of increasing waist radii (distances in μm). A full list of the simulation parameters can be found in Appendix B.4.

Input Face		Simulated Parameters
Type	–	Ridge
Number of Features	N	6
Initial Distance	a	888
Period	p	888
Width	w	445
Depth	s	130

The final input grating parameter that was optimized was the distance a to the centre of the first groove (Figure 5.1(b)). Figure 5.8 shows two ranges over which a was varied. Two smaller resonances were observed at $a = 888$ μm and 1776 μm, which correspond to integer multiples of the period. Larger resonances are found at $a = 1332$ μm and 2220 μm, which correspond to odd multiples of half the period. A distance of 1332 μm displayed the highest transmission at $\lambda = 922$ μm and was chosen in the final bullseye designs.

Gaussian Illumination

Up to this point in the parameter optimization, the simulations have all considered the illumination of the bullseye structure with a linearly polarized plane wave. In other words, all of the rings were illuminated. Investigating the effect of illuminating a different number of rings required the use of a Gaussian beam source. The behaviour of the Gaussian source in Lumerical FDTD Solutions is detailed in Appendix B. The Gaussian beam source is of particular interest, as the experimental THz source used to characterize the bullseye devices is predominately Gaussian (Section 6.1.1).

Table 5.2 gives the parameters of a bullseye ridge-model that was simulated with Gaussian beams with waist radii from 2 mm to 5 mm, illuminating approximately $2-5$ rings. The absolute transmission is plotted as a function of wavelength in Figure 5.9(a). Since the total power contained within a traverse plane of the beam is conserved as the spatial extent of the beam is increased, less power is incident on the area of the aperture. The remain-

ing power is spread across the input ridges. Simulations showed that for waist radii above 3 mm, the power transmitted through the aperture remains approximately the same, despite the energy density on the aperture falling as approximately $1/w_0^2$. It must be emphasized that this is due an increased transmission enhancement that continues to rise as more ridges are illuminated, as shown in Figure 5.9(b).

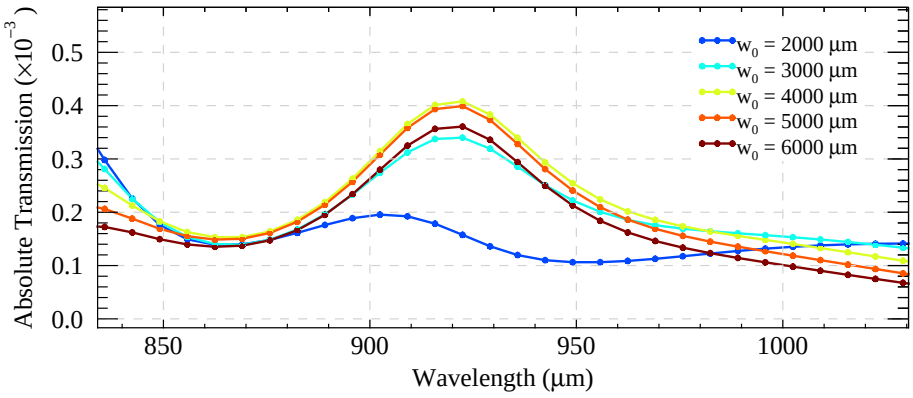

(a)

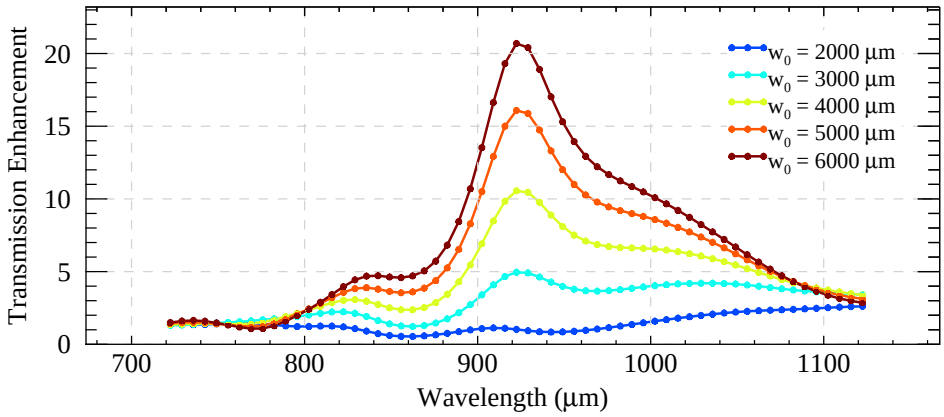

(b)

Figure 5.9: (a) The absolute transmission through bullseye lens with input ridges. The transmission for waist sizes above 3 mm was approximately constant due to (b) the increased transmission enhancement, G.

5.2 Bragg Reflector

When an incident wave couples to a surface plasmon mode, SPPs propagate towards the centre of the structure, enhancing the electromagnetic field at the aperture, as well as propagating radially outward. These outward travelling waves can contribute to the resonant transmission if they are reflected in phase with the inward travelling wave. In an experimental study by Ishihara et al., the transmission of THz radiation through bullseye devices was further enhanced with the introduction of a Bragg reflector [30]. Bragg reflectors are half-period concentric grooves that are placed outside of the main bullseye structure and reflect SPPs back towards the central circular aperture, therefore improving transmission.

Table 5.3: Structural parameters of the simulated Bragg reflector. The Bragg reflector surrounds the ridges given in Table 5.2. Distances are in μm.

Bragg Reflector		**Optimized Parameters**
Type	–	Ridge
Number of Features	N_r	3
Initial Distance	a_r	444
Period	p_r	444
Width	w_r	222
Depth	s_R	130

Simulated reflection gratings were parametrized by the number of grating structures, N_r, the distance to the first feature, a_r , the grating period, p_r, their width, w_r, and their depth, s_r. The ridge model described in the preceding sections was surrounded by three Bragg reflectors with half-periods and half-widths of $p_r = 444$ μm and $w_r = 222$ μm, respectively (see Table 5.3), and simulated using Lumerical FDTD Solutions with a Gaussian beam with a 5 mm waist. Converged simulation parameters were used and error propagation was calculated assuming a 6% error in simulated transmission, as detailed in Appendix B.2.

A comparison of the regular bullseye device with an identical device surrounded by the reflector is shown in Figure 5.10. Table 5.4 summarizes the transmission efficiency η and enhancement factors G of each structure at their resonant wavelength. Although the

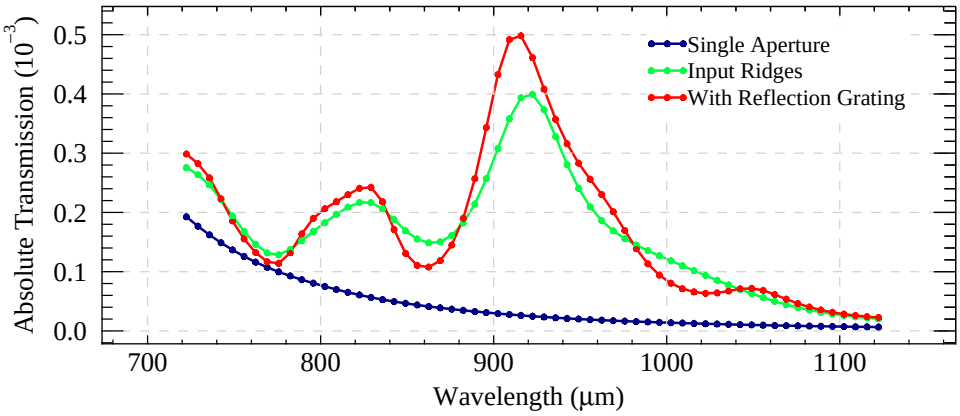

Figure 5.10: The absolute transmission of a $w_0 = 5$ μm Gaussian beam through an aperture ($d = 300$ μm, $t = 200$ μm), a bullseye device with input ridges, and with ridges surrounded by $N_r = 3$ reflection gratings.

peak wavelength is shifted to 915 μm with the addition of the Bragg reflector, which may be due to the reflected SPPs not being entirely in phase, the reflector further increased the transmission efficiency by approximately 25%.

Table 5.4: The absolute transmission, T, transmission enhancement, η, and gain, G, of a Gaussian beam ($w_0 = 5$ μm) through an aperture ($d = 300$ μm, $t = 200$ μm) and bullseye device with input ridges at $\lambda = 922$ μm, and with ridges surrounded by $N_r = 3$ reflection gratings at $\lambda = 915$ μm.

	T ($\times 10^{-4}$)	η	G
Aperture Only	0.248 ± 0.009	0.14 ± 0.01	–
Input Ridges	4.0 ± 0.2	0.22 ± 0.01	16 ± 1
Input Ridges with Reflector	5.0 ± 0.3	0.28 ± 0.02	20 ± 2

5.3 Focusing with Phase Tuned Output Structures

In a similar way that geometrical structures on the input side couple incident light into SPPs, structures on the output side of the lens can collimate, focus, or directionally beam the emerging light. This has been shown by mirroring the input corrugations to the output surface [3, 23, 83] and by modulating the radial position [89] or depths of grooves [82, 84, 90, 91]. These reports have attempt to relate the structural parameters to the focusing

behaviour, however, a full design methodology is not often discussed.

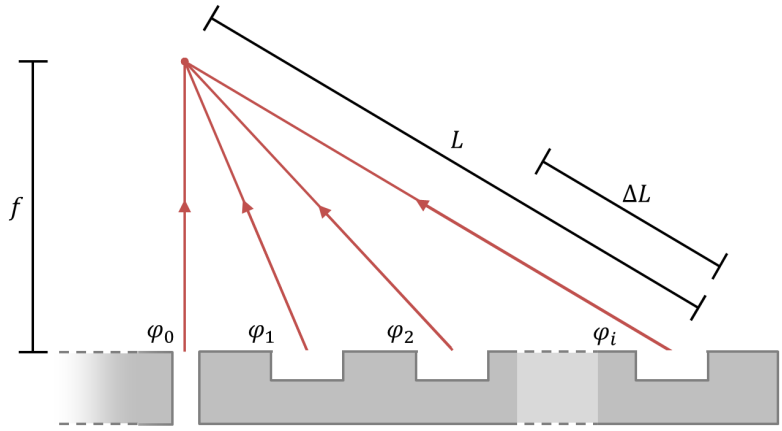

(a) Simulated phase locations for the groove model.

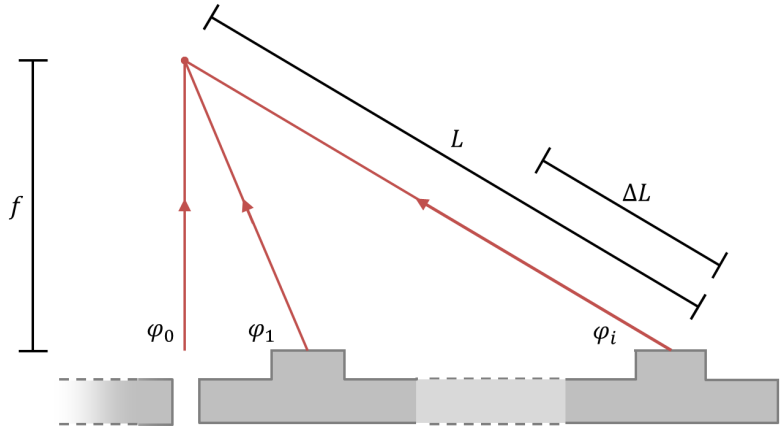

(b) Simulated phase locations for the ridge model.

Figure 5.11: For groove designs, the phase was recorded in the output plane of the aperture. For ridge designs, the phase was recorded at the top of the ridge and at the centre of the aperture in the plane defined by the top of the ridge.

Phenomenological phase modulation models have been recently developed for nano-scaled slit-groove devices and bullseye lenses [24, 92–94]. In these simple models, light diffracted at the output face couples with SPP modes and propagate along the surface, scatters off an output surface structure, and couples back into the radiation field (see Figure5.11(b)). I.e., individual grooves/ridges can be considered as a Huygen emitter with a specific initial phase, φ_i. The relative phase difference between light travelling through the central aperture, φ_0, and that of SPPs scattered off of surface corrugations, φ_i, can be found using

numerical techniques.

To illustrate this principle, in order to produce a focal spot at a distance f from the bullseye structure, the path length of the scattered SPP is calculated using

$$L = \sqrt{f^2 + (nr_i)^2} \tag{5.3}$$

and the path difference with a directly transmitted photon is

$$\Delta L = L - f = \sqrt{f^2 + (nr_i)^2} - f. \tag{5.4}$$

The corresponding phase difference due to ΔL is given by $k\Delta L$, where k is the wavenumber. Using the condition of constructive interference, the sum of the phase due to the path difference and the phase difference due to the scattering off of the groove/ridge must be an integer multiple of 2π:

$$(\sqrt{f^2 + (nr_i)^2} - f)k + \varphi_{i,0} = 2\pi m, m = 0, \pm 1, \pm 2, \ldots, \tag{5.5}$$

where $\varphi_{i,0} = \varphi_i - \varphi_0$ is the difference between the wave directly transmitted through the aperture and a secondary wave emitted from surface corrugation i.

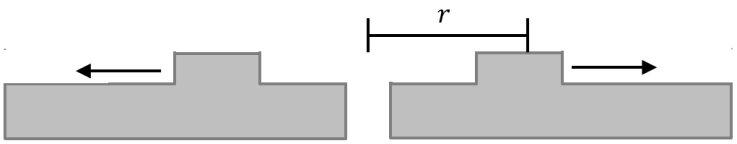

Figure 5.12: Simulations were performed by shifting one concentric ridge radially outward.

To investigate the variation in phase of the secondary sources as a function of ridge radius and width, simulations were performed at $\lambda = 922$ μm for an aperture diameter of 200 μm and thickness of 50 μm. A single ridge with a width of 445 μm and a height of 100 μm was placed on the output side of the device with increasing radial positions, as shown in Figure 5.12. The phase at the location of the ridge and the aperture, as shown in

Figure 5.11(b), was recorded to find the phase difference $\varphi_{i,0}$ as a function of r. The raw simulated data is shown in Figure 5.13(a). The phase difference $\varphi_{i,0}$ increases linearly as a function of groove radius and is wrapped around $\pm\pi$. This data was unwrapped, as shown in Figure 5.13(b), and a linear fit was performed.

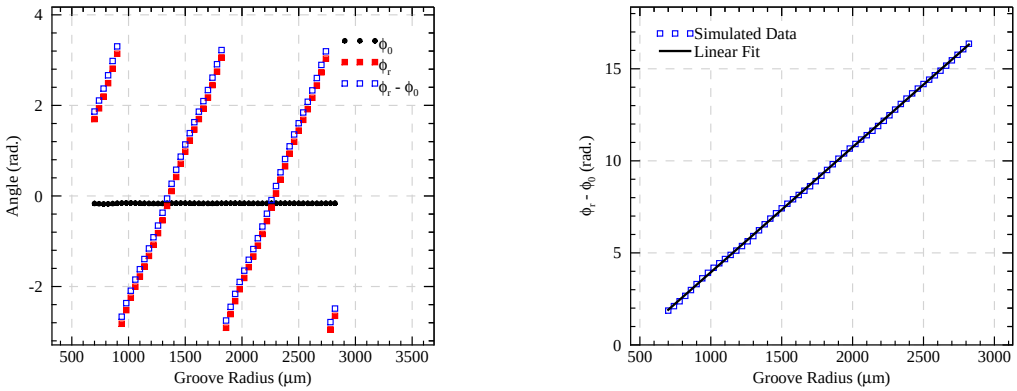

(a) Simulated wrapped phase values.

(b) Unwrapped phase values with linear fit.

Figure 5.13: (a) The phase difference between light transmitted through a $d = 200$ μm aperture, φ_0, and that light scattered off a $s = 100$ μm, $w = 445$ μm ridge at increasing radial distances. (b) The phase difference was unwrapped and fit with a linear function.

The fitted slope and intercept were $m_r = 6.80 \pm 0.01$ mm^{-1} and $b_r = -2.85 \pm 0.1$, respectively. This procedure was repeated for a ridge height of 180 μm with a fitted parameters $m_r = 6.90 \pm 0.09$ mm^{-1} and $b_r = -9.1 \pm 0.1$. The average of both the simulated slopes was found to be $m_r = 6.8 \pm 0.1$ mm^{-1}. This value was used as the radial dependence on the phase difference $\varphi_{i,0}$.

A single ridge was then simulated at $r = 700, 1150$, and 2500 μm for different widths of constant height $s = 100$ μm. Linear fits were made following a similar procedure and the average slope was found to be $m_w = -3.5 \pm 0.3$ mm^{-1}.

It was assumed that $\varphi_{i,0}$ is a sum of the linear contributions due to each structural parameter, i.e.,

$$\varphi_{i,0} = \varphi_r + \varphi_w, \qquad \text{(rad)} \quad (5.6)$$

where $\varphi_r = m_r r + b_r$ and $\varphi_w = m_w w + b_w$. Combining the independent contributions of ridge location and width gives a general form of

$$\varphi_{i,0} = m_r r + m_w w + b, \quad \text{(rad)} \quad (5.7)$$

where the intercept

$$b = b_r + b_w \quad \text{(rad)} \quad (5.8)$$

was found to be $b = -1.3 \pm 0.1$ by combining simulated values for φ_r and φ_w. The final equation describing the phase difference $\varphi_{i,0}$ for ridges of varying radial positions and widths is

$$\varphi_{i,0} = (6.8\ \text{mm}^{-1})r - (3.5\ \text{mm}^{-1})w - 1.3. \quad \text{(rad)} \quad (5.9)$$

Using this phase relationship, Equation 5.5 was solved numerically for a wavelength of 922 μm, a constant width of $w = 445$ μm, and a focal length of $f = 3$ mm, for integers multiples of 2π to obtain the required radii of each ring. This procedure is shown graphically in Figure 5.14 and the simulated beam profile is shown in the following section.

For completeness, a similar model was also generated for output grooves as a function of radial position and groove depth:

$$\varphi_{i,0} = (6.85\ \text{mm}^{-1})r + (10.0\ \text{mm}^{-1})s - 6.61. \quad (5.10)$$

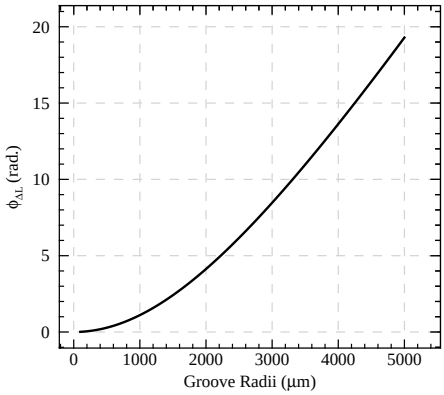

(a) The phase difference due to the path length difference ΔL.

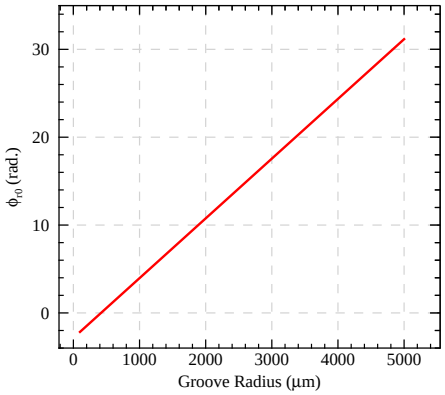

(b) The phase difference between light travelling through the aperture and SPPs scattered from ridges.

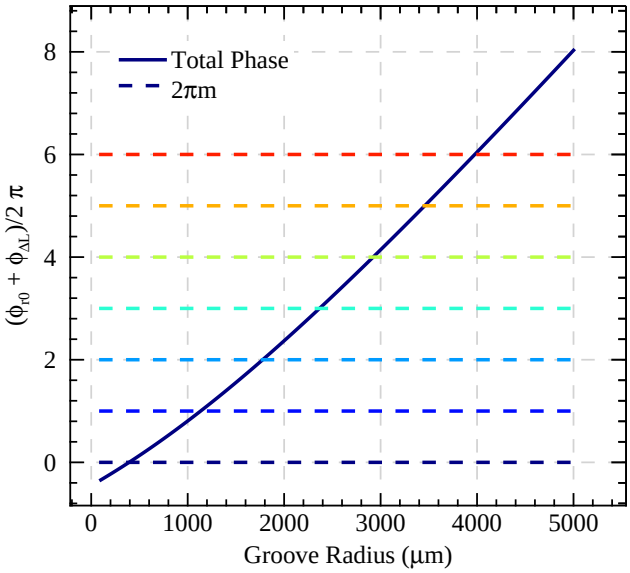

(c) Radii where the total phase satisfies the condition of constructive interference (i.e., is integer multiples of 2π).

Figure 5.14: (a) The phase contributions $\varphi_{\Delta L}$ for $f = 3$ mm and (b) $\varphi_{i,0}$ were summed and (c) solved for $2\pi m$ to obtain radial positions of 5 ridges.

5.4 Fabricated Bullseye Designs

As a result of the optimization procedure described in this chapter, two final bullseye lenses were designed and fabricated, as shown in Figures 5.15 and 5.19. Both designs have input ridges that were chosen for maximum transmission efficiency and have identical aperture diameters of 300 μm and thicknesses of 50 μm. The first design consists of only input ridges and a planar output face. The second design is patterned with a radially-tuned output surface to focus outgoing radiation approximately 3 mm away from the output face. An outer support ring was placed around the bullseye structure with dimensions chosen for mounting purposes (Section 7.1). The distance from the last groove to the inner wall of the support ring was chosen to be an integer multiple of ridge periods away from the reflection grating, however simulations showed that this was not a relevant parameter.

The theoretical performance of each device was determined by simulating their transmitted powers and the beam profiles when illuminated by a linearly polarized Gaussian beam of $w_0 = 5.1$ mm. A single aperture with the same diameter and thickness was also simulated to calculate the transmission enhancement, G, of each device. The transmission enhancement through the single-sided and double-sided devices are shown in Figures 5.16 and 5.20, respectively. Since the input ridges on both devices were identical, it was expected that transmission enhancement curves for each device would be identical. Although some variation in the simulation results is apparent, the transmission enhancement values are within the 8% estimated simulation error (discussed in Appendix B). The reported theoretical transmission enhancement is presented as the average of values from both curves. The maximum transmission enhancement occurs at $\lambda = 915$ μm with a value of $G = 37 \pm 3$. At $\lambda = 922$ μm, the simulated enhancement has a value of $G = 29 \pm 2$.

The simulated beam profile at $\lambda = 922$ μm for the double-sided device is shown in Figure 5.21. Data along $x = 0$ was interpolated to locate the focus at a distance of $z \approx 3.5\lambda$, or 3.2 mm, away from the output surface of the device. A cross-section in the x-direction through the location of the focus was fitted to a Gaussian function to find a FWHM of

864 ± 7 μm (Figure 5.22). It should be noted that the phase modulation model described in Section 5.3 was determined for ridges with a height of 100 μm, while the final fabricated devices have ridge heights of 130 μm. Despite the height discrepancy in the analysis, the phase distribution model provided a good estimate of the location of the simulated focal spot.

Fabrication was performed at NRC Automotive and Surface Transportation using micromachining techniques [95]. Since metals behave as perfect electrical conductors at THz frequencies, the type of metal used in the machining of the device was not a limiting factor, and copper was chosen for all designs. Information regarding the fabrication procedure of a double-sided bullseye, results from which are not presented in this thesis, can be found in Appendix C. Photographs of the final devices are shown in Figures 5.18 and 5.23. A fabrication report can be found in Appendix C that details accuracy of the critical design parameters, which were within $\pm$ 1 μm.

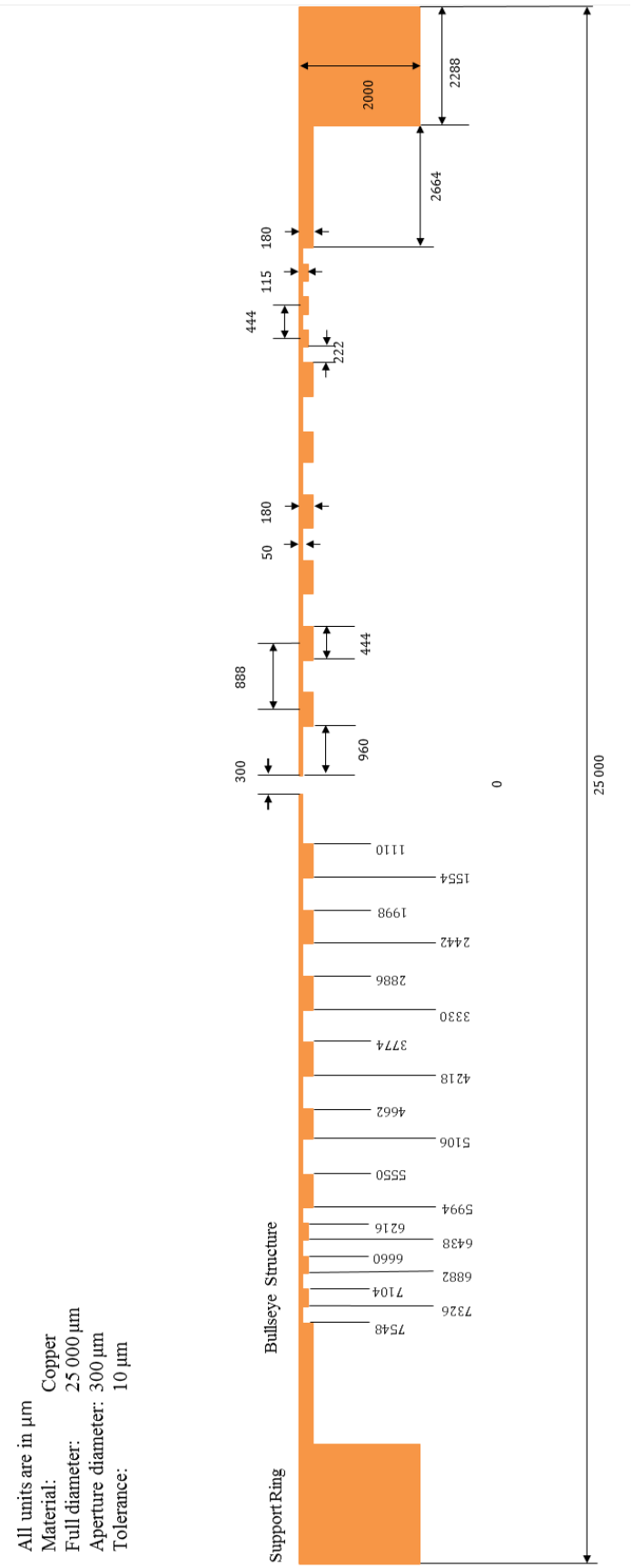

Figure 5.15: Single-sided bullseye with input ridges and reflection grating. An outer support ring was modelled for mounting purposes. Distances are in µm.

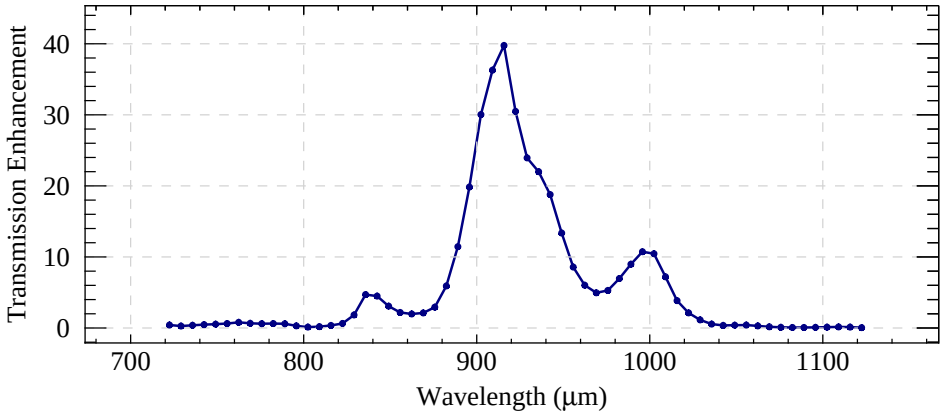

Figure 5.16: Simulated transmission enhancement through the designed single-sided bullseye illuminated with a $\lambda = 922$ μm linearly polarized Gaussian beam of $w_0 = 5.1$ mm.

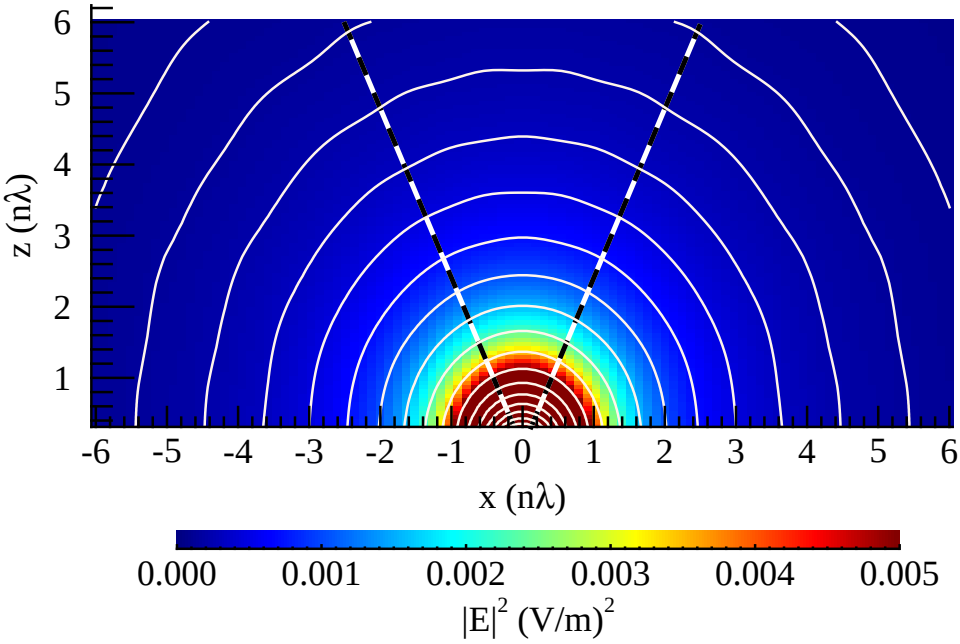

Figure 5.17: Simulated beam profile of the designed single-sided bullseye illuminated with a $\lambda = 922$ μm linearly polarized Gaussian beam of $w_0 = 5.1$ mm. Dashed lines represent the acceptance angle of f/1 parabolic mirrors.

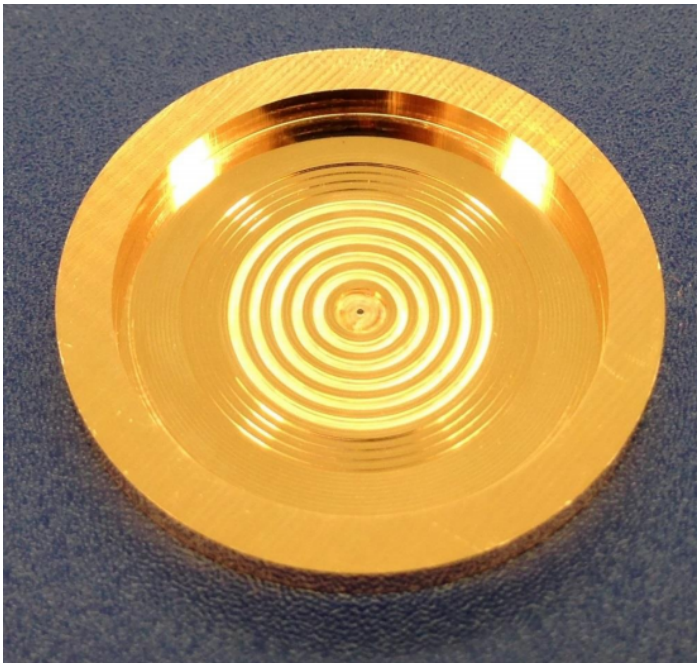

(a) Input face.

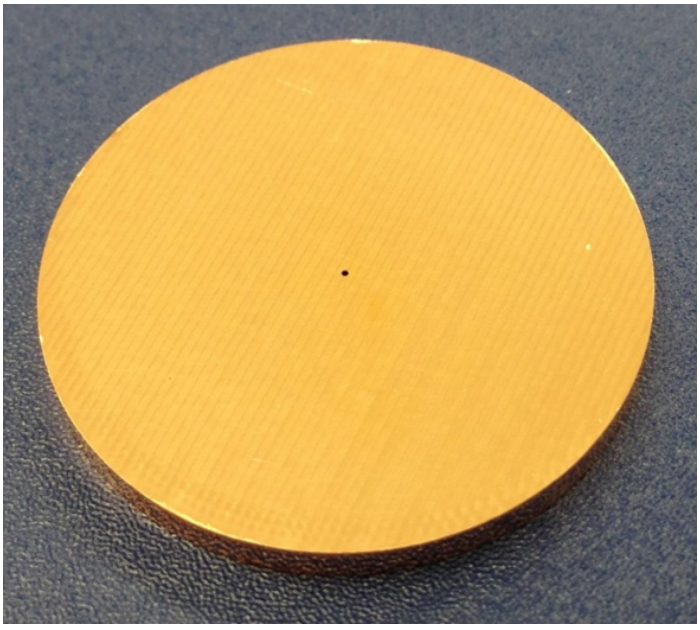

(b) Output face.

Figure 5.18: Photographs of the final single-sided bullseye with ridges and a Bragg reflector on the input side of the device.

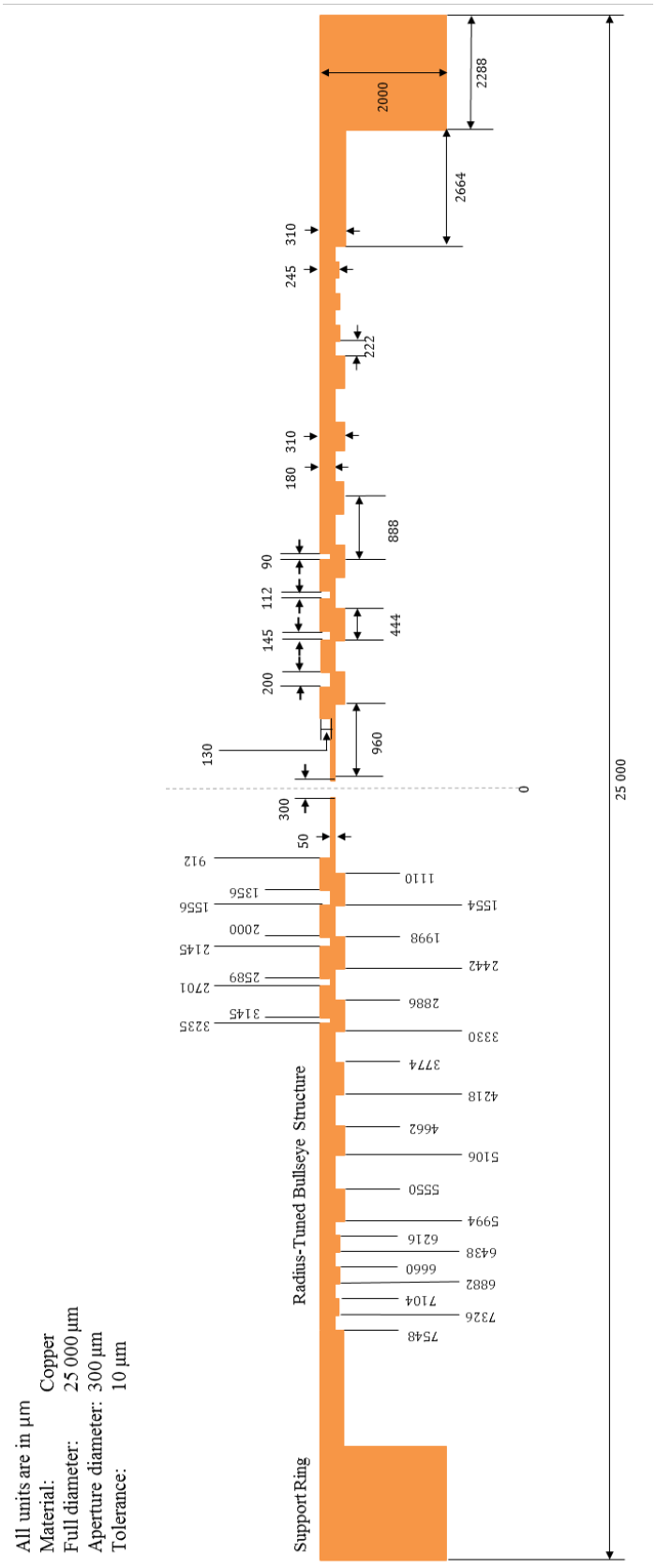

Figure 5.19: Double-sided bullseye design with input and output ridges, input reflection grating, and output grooves radially tuned for a focus at $f = 3$ mm from the output face. Distances are in µm.

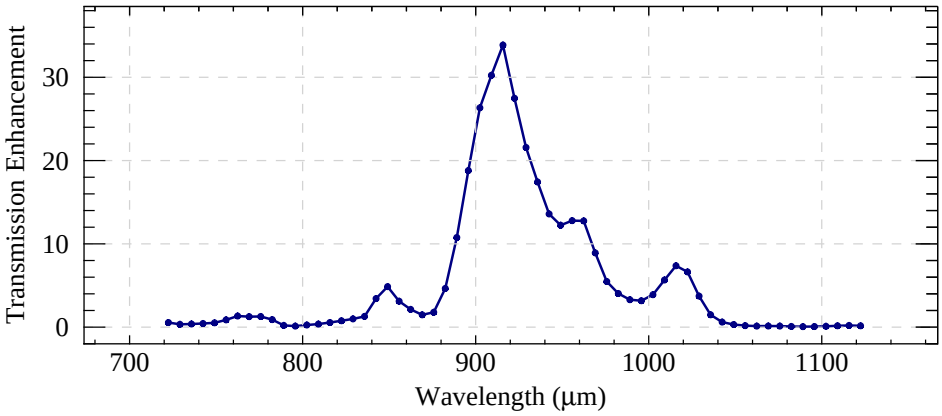

Figure 5.20: Simulated transmission enhancement through the designed double-sided radially-tuned bullseye illuminated with a $\lambda = 922$ μm linearly polarized Gaussian beam of $w_0 = 5.1$ mm.

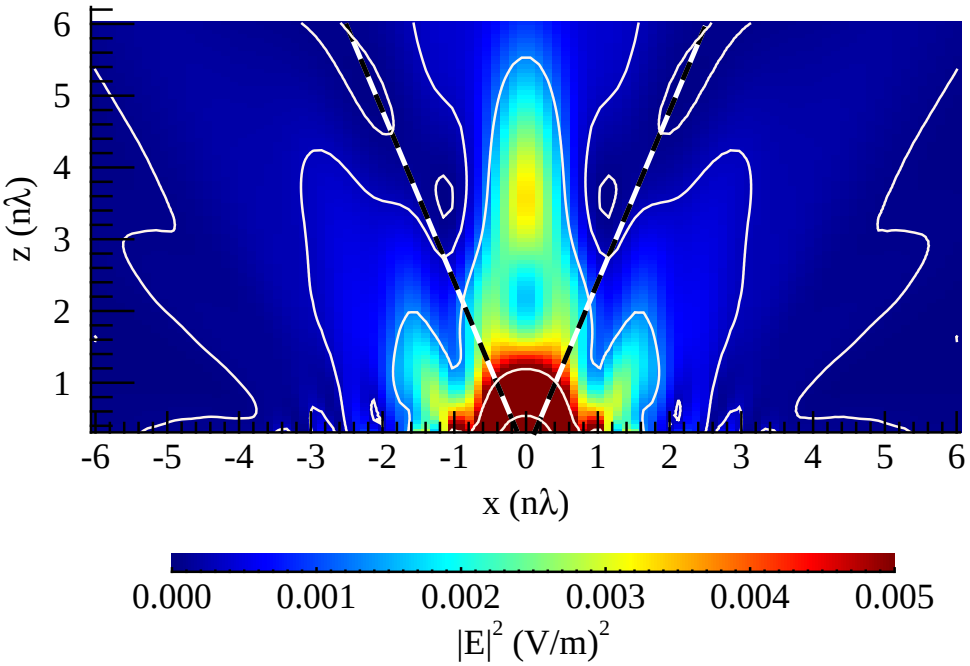

Figure 5.21: Simulated beam profile of the designed double-sided radially-tuned bullseye illuminated with a $\lambda = 922$ μm linearly polarized Gaussian beam of $w_0 = 5.1$ mm. Dashed lines represent the acceptance angle of f/1 parabolic mirrors.

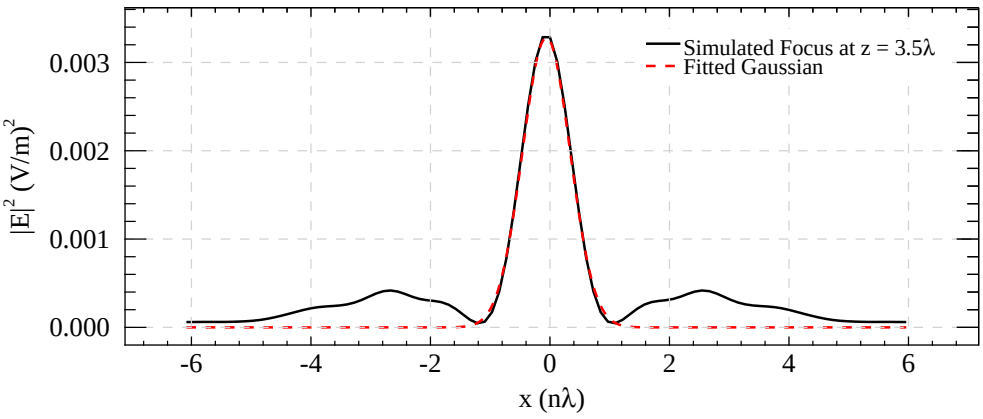

Figure 5.22: A cut in the *x*-direction through the focus was fitted to a Gaussian function to find a FWHM of 864 $\pm$ 7 μm.

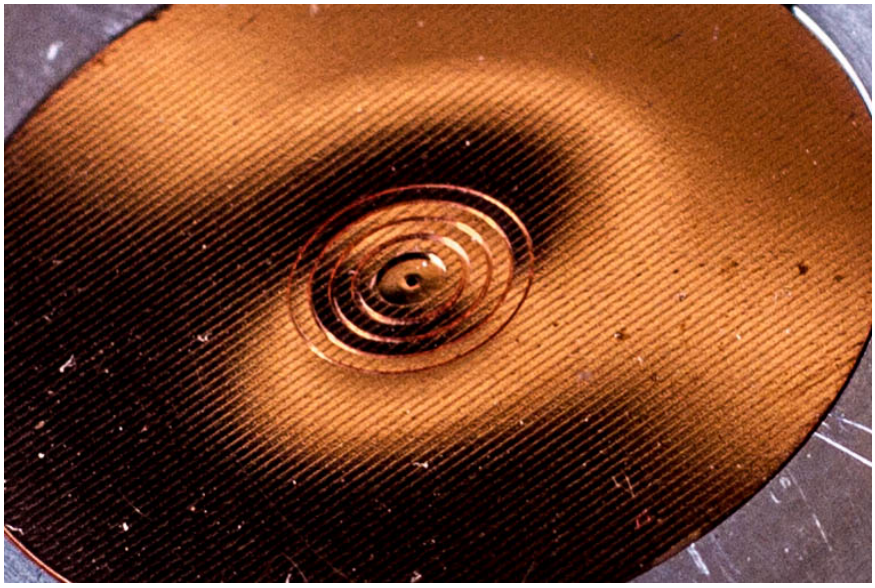

Figure 5.23: Photograph of the output face of the double-sided radially-tuned bullseye.

Chapter 6

Design of a THz Testbed

In Chapter 5, the design and simulated performance of bullseye plasmonic lenses, optimized for enhanced transmission and beam confinement at THz frequencies, was presented. To verify the performance of the fabricated devices, an optical testbed consisting of a room temperature THz source and detector was designed and developed. A photograph of the system is shown in Figure 6.1. The testbed makes use of a line source whose beam profile is predominately Gaussian and whose frequency can be tuned over the range of $320-330$ GHz, corresponding to wavelengths of $908-937$ μm. Two 90° off-axis parabolic (OAP) mirrors re-image the beam from the horn at the location of the bullseye lens. After the lens, two additional OAPs collect the transmitted light and focus it on the detector. Details pertaining to the design of the THz testbed are given in Section 6.1. Signal acquisition was accomplished using standard lock-in techniques and is described in Section 6.2. Section 6.3 details beam profile measurements of the THz source. The frequency dependent power of the THz source is discussed in Section 6.4. A ubiquitous feature of optical systems at these wavelengths is resonant cavities that are unavoidable. Due to the resonant nature of the system, transmission measurements as a function of a frequency require careful interpretation and is further discussed in Chapter 7.

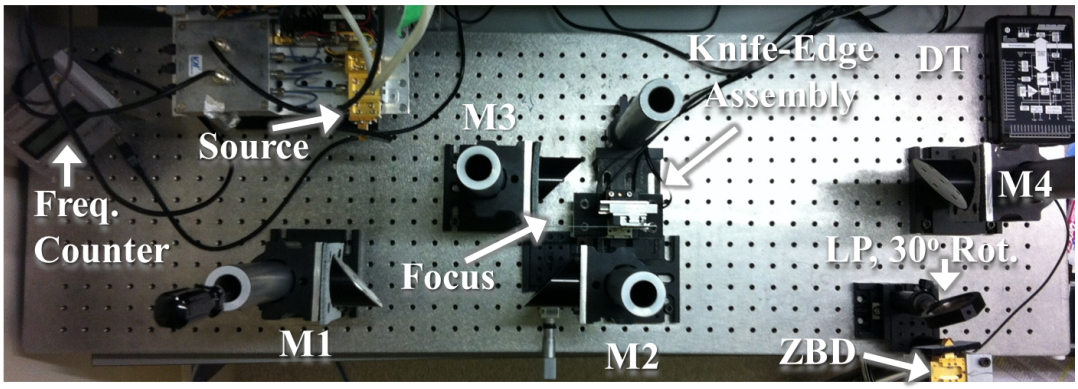

Figure 6.1: A top-down photograph of the THz testbed configuration used for source power measurements. The THz beam produced by the source is collected by mirror M1, focused by M2 to an intermediate image plane, collimated by M3, and brought to a focus by M4 on the detector. LP: a linear polarizer is rotated approximately 30° with respect to the transverse *xy*-plane to minimize reflections within the system. DT: digital-to-analogue converter.

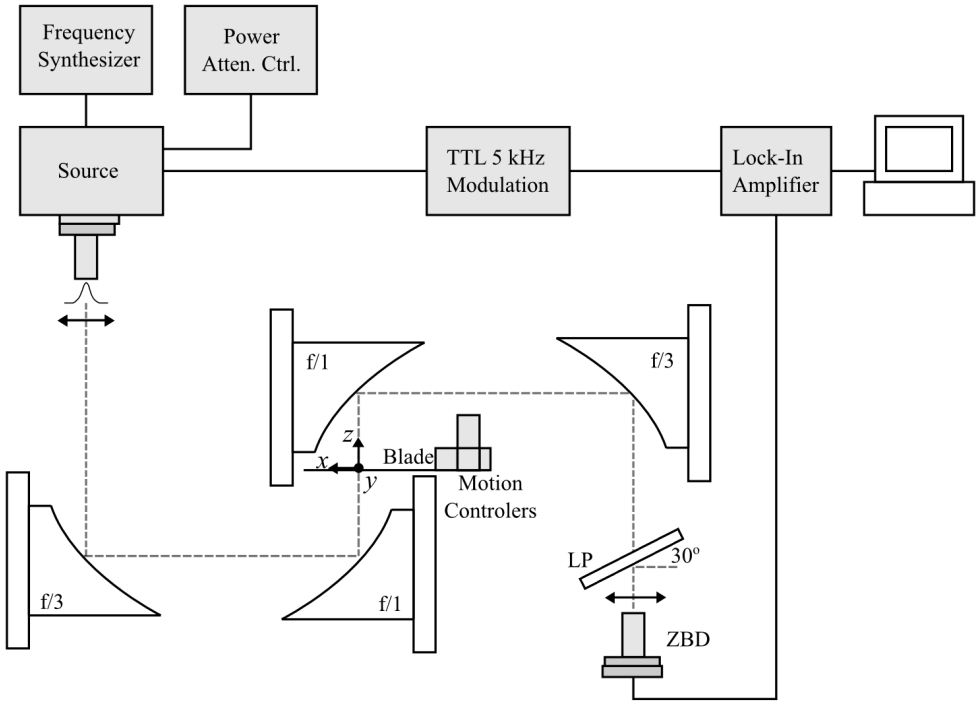

Figure 6.2: A schematic diagram of the testbed configuation shown in Figure 6.1.

6.1 Testbed Components

A schematic diagram of the testbed is shown in Figure 6.2. The z-direction is defined as the axis of propagation. Perpendicular to the propagation axis, x and y correspond to the horizontal and vertical directions, respectively. Specific components of the optical configuration, including the source, detector, and polarizing elements, are described in the following sections. Different configurations of the testbed were used to measure: beam profiles, source power, and transmission through single apertures and bullseye lenses. This discussion will highlight the common features of each configuration.

6.1.1 THz Line Source and Corrugated Horn

The THz signal is produced by a Virginia Diodes, Inc. (VDI) line source transmitter with a frequency bandwidth of 320-330 GHz ($908-937$ μm) [96]. The source is based on the principle of frequency multipliers, which takes advantage of the nonlinear response of a GaAs Schottky diode to incident microwave radiation produced by a 10 GHz oscillator, which is stabilized to a 10 MHz crystal oscillator [96, 97]. The diode generates an output signal that contains harmonics of the input frequency, a portion of which is selected as the desired output frequency. There are several multiplier stages that produce a resulting gain of 32. Tuning the 10 GHz source results in a frequency range of 320-330 GHz. The source is rated to have a maximum power output of approximately 10 mW, however, the output power varies with frequency, as discussed Section 6.4. Two key features of the system are a BNC attenuation input that accepts up to 5V to control the output power and a BNC input for modulating the source up to 20 kHz.

To produce a single mode Gaussian beam, a corrugated feedhorn is required [98]. However, they are difficult to manufacture. It has been shown that a split-block rectangular feedhorn (Figure 6.3(a)) is easier to fabricate and emits a horizontally polarized Gauss-Hermite beam with approximately 84.3% of its power in the fundamental Gaussian mode [98]. A schematic of the VDI source/detector horn is shown in Figure 6.3(b). The characteristics of

the Gaussian beam can be derived from the geometry of the horn using waveguide theory. The Gaussian beam waist, w_0, and location of the beam waist inside the throat of the horn, z_a, are given by: [98]

$$w_0 = \frac{\kappa a}{\sqrt{1 + \left(\frac{\pi \kappa^2 a^2}{\lambda L}\right)^2}} \tag{6.1}$$

$$z_a = \frac{L}{1 + \left(\frac{\lambda L}{\pi \kappa^2 a^2}\right)^2}, \tag{6.2}$$

where

$$\kappa a \approx 0.863191 \tag{6.3}$$

was calculated numerically in [98] to optimize the power in the fundamental Gaussian mode.

The VDI horn has a length of $L = 21.4$ mm and an aperture opening of $d = 4.6$ mm.

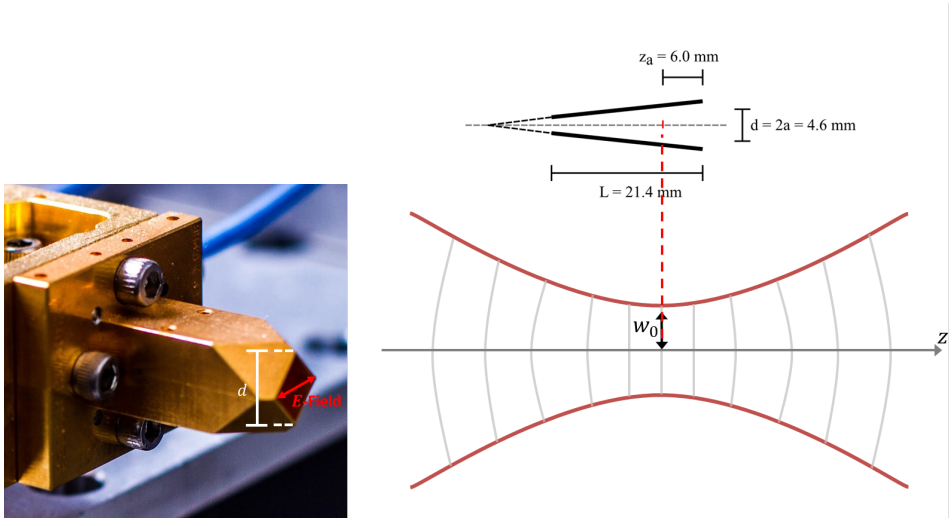

(a) (b)

Figure 6.3: (a) Photograph of the split-block diagonal horn. (b) Horn dimensions and location of beam waist.

The beam waist and waist location were calculated as a function of the source frequency and are summarized in Table 6.1.

Table 6.1: The beam waist radius, w_0, and its location within the horn, z_a, as measured from the horn output, as a function of source frequency. To a good approximation, it can be assumed that the mean values can be used ($z_a = 6.04 \pm 0.09$ mm and $w_0 = 1.682 \pm 0.005$ mm).

f (GHz)	λ (μm)	z_a (mm)	w_0 (mm)	FWHM (mm)
320	937	5.909	1.689	1.989
321	934	5.936	1.688	1.987
322	931	5.963	1.686	1.985
323	928	5.990	1.685	1.984
324	925	6.016	1.683	1.982
325	922	6.043	1.682	1.980
326	920	6.070	1.680	1.978
327	917	6.096	1.679	1.977
328	914	6.123	1.677	1.975
329	911	6.150	1.676	1.973
330	908	6.180	1.675	1.972

6.1.2 Zero Biased Diode Detector

The detector used is a zero-biased diode (ZBD) with an optical noise-equivalent power of 2.9 pW/$\sqrt{Hz}$. The horn on the detector is identical to that on the source and accepts horizontal polarized light. The diode response is intrinsically nonlinear, however when the diode is not biased and the incident power is sufficiently small, on the order of 0–10 μW, the diode is well approximated by a linear response. Furthermore, by not applying an external bias, there is no additional noise associated with a necessary power supply.

Manufacturer specifications give the responsivity R of the detector between 320–330 GHz to be $R \approx 1500$ V/W. Using this responsivity, a maximum signal of 15 mV ensures that the power incident on the detector lies within the linear regime. Safe operation of the ZBD requires the input signals to be less than 1 mW (1.5 V).

6.1.3 Stage Optics

Optics were mounted on a Newport Scientific Grade Optical Breadboard using Newport M-VPH no-slip optical post holders, M-SP stainless steel optical mounting posts, and LH-2 2" diameter lens mounts [99]. Four 50.8 mm diameter aluminum 90° off-axis parabolic (OAP) mirrors were configured in an arrangement to provide an intermediate imaging plane [97]. The OAPs were orientated such that rays from a single field point strike identical coordinates on each parabolic mirror (i.e., in a "tip-to-tip" fashion) to avoid a tilted image plane [100].

The source and detector horns were aligned such that the location of the Gaussian beam waist within the horn was at a focal length away from mirrors M1 and M4 (Figure 6.1). Although the input waist size and its location within the horn change with frequency (Table 6.1), mean values of $w_0 = 1.682 \pm 0.005$ mm and $z_a = 6.04 \pm 0.09$ mm were adopted.

6.1.4 Linear Polarizers

Wire-grid polarizers, consisting of parallel conducting wires whose width and spacing are smaller than the incident wavelength, provide a simple means to attenuate the THz beam [6]. Consider the wire-grid orientated vertically; the component of the electric field parallel to the wires drives conduction electrons to accelerate and re-radiate an electric field that results in the reflection of the incident wave. Electrons in the perpendicular direction are not free to move and the perpendicular component is transmitted. When the axis perpendicular to the wires, i.e., the transmission axis, is rotated by an angle, θ, the transmission through the polarizer follows Malus' Law [6],

$$\frac{I}{I_0} = \cos^2 \theta_i, \tag{6.4}$$

where I_0 ($\mathrm{W \cdot m^{-1}}$) is the intensity of the light incident on the polarizer, I ($\mathrm{W \cdot m^{-1}}$) is the transmitted intensity, and θ_i (rad) is the angle between the light's initial polarization

and the transmission axis of the polarizer. For unattenuated source power measurements, a polarizer with its transmission axis crossed with the incident polarization to effectively reduce the source power to a value that can be safely measured by the ZBD.

6.2 Signal Detection with a Lock-in Amplifier

Lock-in detection is a method used to measure small amplitude AC signals in the presence of a high background noise. A lock-in amplifier has two inputs: a modulated signal from the detector and a reference signal with the same frequency. The two signals are then multiplied and integrated for a time longer than their period (usually on the order of milliseconds). Making use of the orthogonality of sinusoidal functions, if the frequencies of the two signals are not equal, the integrated product is zero. When the two functions have identical frequency, the integrated result is half the product of the amplitudes. That is, the lock-in produces a DC output that filters out Fourier components of the signal that are not equal to the modulated frequency. This filtering occurs over a very narrow frequency range, leading to high signal-to-noise.

A 5 kHz TTL modulation was applied to the source using a Stanford Research Systems Model DS335 3.1 MHz Synthesized Function Generator [101]. Lock-in techniques were applied using a Stanford Research Systems Model SR830 DSP Lock-In Amplifier to extract the THz signal referenced against the 5 kHz modulation. The modulated signal measured by the ZBD, the reference signal, and the output from the lock-in were viewed on a Tektronix DPO 4034 Digital Phosphor Oscilloscope, as shown in Figure 6.4 [102]. The top green line shows the modulating signal applied to the THz source. The middle blue line shows raw signal from the ZBD, which is a slightly asymmetric square wave (i.e., the marked-to-space ratio is not 50:50). Nevertheless, it has a fundamental frequency that the lock-in can determine when provided the reference signal.

The bottom, pink signal is the DC signal that is output from the lock-in. As is common with all lock-in amplifiers, the output signal is related to the signal displayed on channel 1,

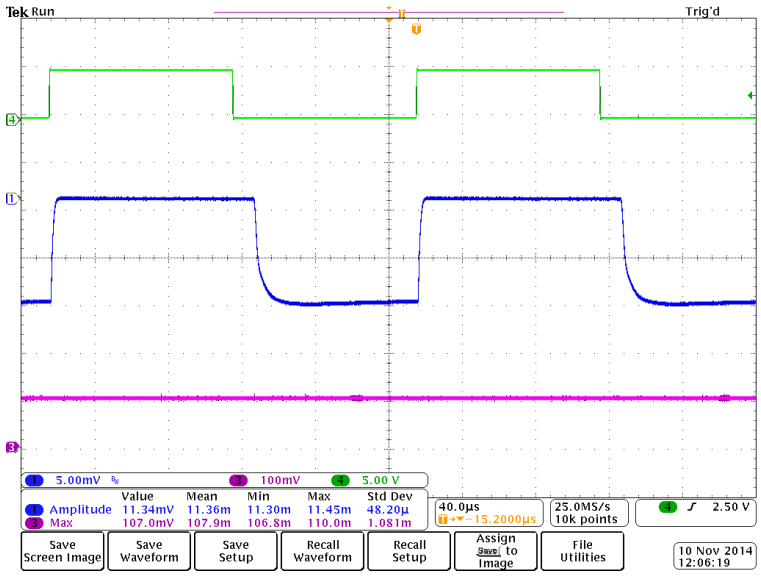

Figure 6.4: A screenshot of the oscilloscope when performing lock-in measurements. Top, green: modulating signal. Middle, blue: raw signal from the ZBD. Bottom, pink: the DC signal output from the lock-in.

X, and the sensitivity setting:

$$\text{Output} = (X/\text{Sensitivity}) \times 10 \text{ V}. \tag{6.5}$$

It is important to consider this gain, as the lock-in output was measured using a Data Translation DT9804 analogue-digital-to converter with a bipolar input range of $\pm$ 10 V [103]. The source attenuation and the sensitivity scale of the lock-in amplifier were carefully chosen such that the output of the lock-in does not exceed this allowable input range.

6.3 Beam Profile Measurements

It is common practice to determine the quality of a beam by measuring the integrated power as a straight- or knife-edge is translated through the focus. This is referred to as a knife-edge test. The signal measured as a function of the knife-edge position takes the form of:

$$P = P_T[1 - \text{erf}(\sqrt{2}(y - y_0)/w_0], \tag{6.6}$$

This corresponds to the integrated beam intensity profile of the Gaussian beam and is commonly referred to as an S-curve.

The knife-edge apparatus consists of a standard utility blade mounted to a three-axis piezo CONEX-AGP Agilis-P Controller with Encoder Feedback placed near the focus [99]. This apparatus is shown in Figure 6.5. The three-axis stage allowed the knife to be moved with a minimum incremental motion of 0.2 µm with a travel range of 27 mm. The back side of the arm-razor configuration was covered with THz-absorbing Eccosorb to limit stray reflections. A control and data-acquisition program was written in IDL that recorded the output DC voltage from the Data Translation unit as a function of position as the knife was moved across the aperture [103, 104]. In a typical configuration, the knife was moved vertically (y) until the entire beam was blocked. This was performed at successive locations along the propagation axis to determine the location of the focus.

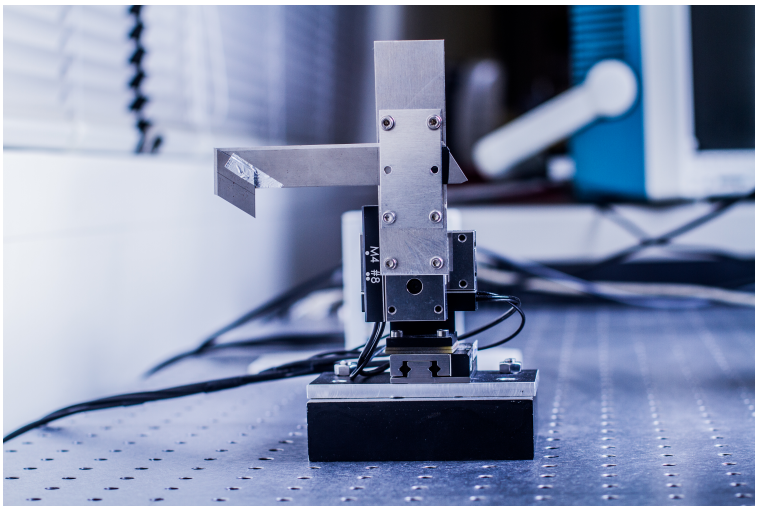

Figure 6.5: The knife-edge testing apparatus used to measure the integrated beam intensity.

To illustrate this method, Figure 6.6 shows the S-curve measured at the location of the focus. An error function was fit to the S-curves with a fixed total power P_T to obtain the Gaussian beam waist, w_0, and the height of the optical axis, y_0. Since this measurement represents the integrated beam intensity, the derivative is taken to obtain the corresponding Gaussian profile.

This can be repeated as a function of z and obtain the full beam profile, as shown in Figures 6.7(a) and 6.7(b). The location of the focus can be determined by locating the beam profile with a minimum waist size, as shown in Figure 6.8(a).

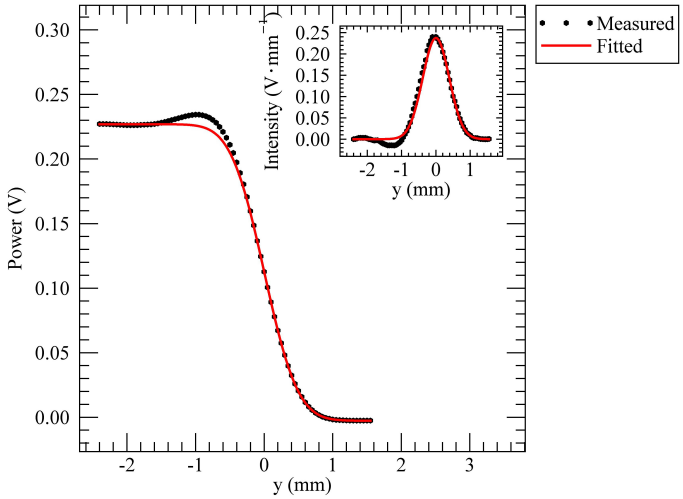

Figure 6.6: Measured (black, dotted) S-curve with an error function fit (red, solid) at the focus of the Gaussian beam. Inset: the corresponding Gaussian beam profile overlaid with the derivative of the error function fit.

In anticipation of the results in Section 6.4, it is worth noting that oscillations in Figures 6.7 and 6.8 occur when the blade position is translated by a distance of $\approx \lambda/2$, where $\lambda \approx 1$ mm, along the axis of propagation. This can be attributed to the presence of a resonant cavity in the optical system (further discussed in Section 6.4.1).

6.4 Source Power

As mentioned in Section 6.1.1, the output power of the VDI source is a function of the source frequency. In order to calculate the transmission through an aperture as a function of frequency, a reference power curve is required to normalize the transmitted signal.

When the testbed is used to study the transmission through single apertures and bulls-eye lenses, the source was unattenuated to maximize the signal-to-noise. However, without a device in place, the voltage across the ZBD would exceed the safe limit of 1.5 V (Section 6.1.2). Since the source attenuation is frequency dependent, reference power measure-

ments were made by placing a linear polarizer near the ZBD with its transmission axis at an angle of $\approx 65^{\circ}$ with respect to the incident horizontal polarization. An IDL program was written to step through the source frequency from 320-330 GHz in steps of $1/64$ GHz ($\Delta\lambda \approx 0.18$ μm) [104]. A 20 ms wait between steps allowed for output power to stabilize before a measurement was made. An average of 100 data points was taken and error bars are presented as one standard deviation. The measured output power as a function of

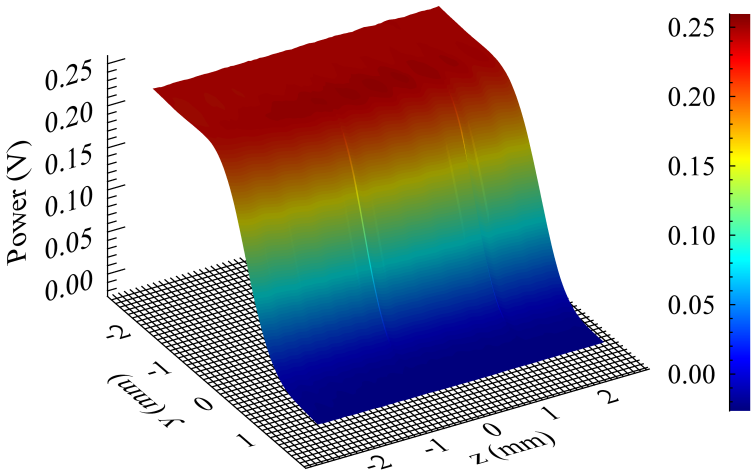

(a)

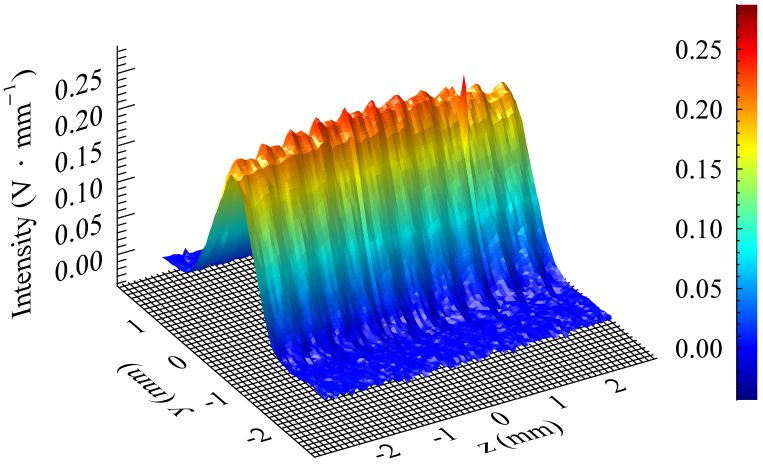

(b)

Figure 6.7: (a) The measured S-curves at positions along the axis of propagation. (b) The derivative of the S-curves was taken to obtain the Gaussian profile.

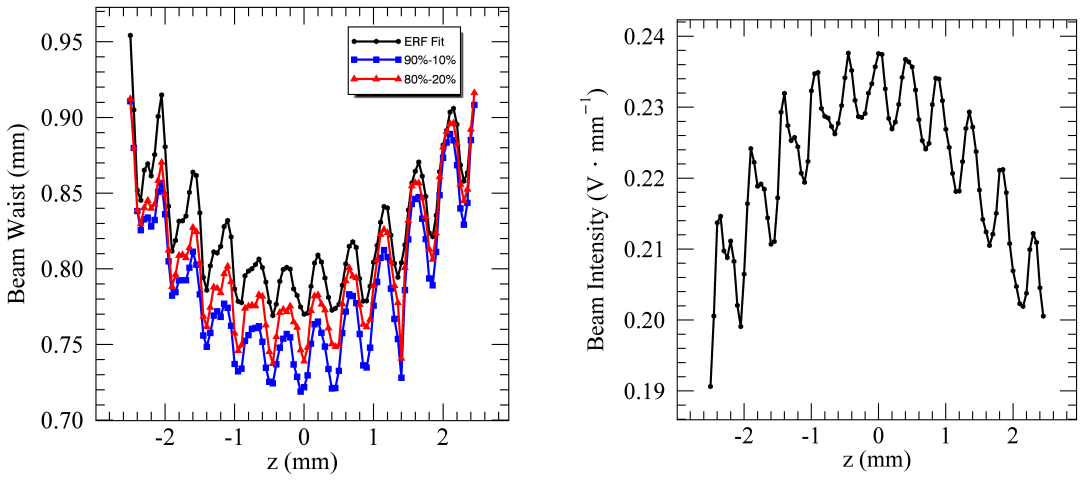

(a) (b)

Figure 6.8: (a) The beam waist radius (left) and maximum Gaussian beam intensity (right) from corresponding error function fits (black, dotted) along the propagation axis (z). The waist radius was also calculated using a 90%-10% (blue, squares) and 80%-20% (red, triangles) analysis. The oscillations seen are due to resonant cavities formed in the optical system.

frequency is shown in Figure 6.16, exhibiting resonant fringes.

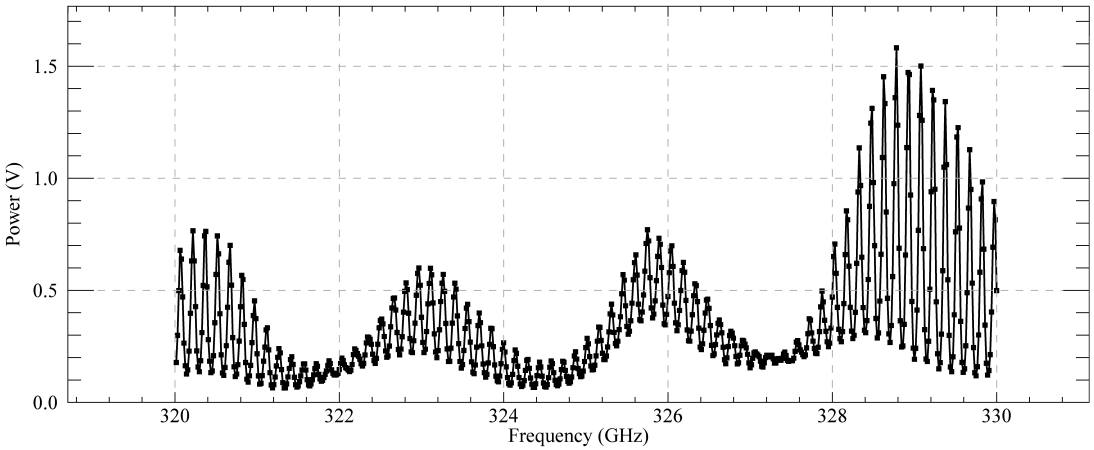

Figure 6.9: Measured power output from the VDI source with a polarizer placed perpendicular to the optical axis (rotation of 0°). Error bars are suppressed for clarity and are shown in Figure 6.10.

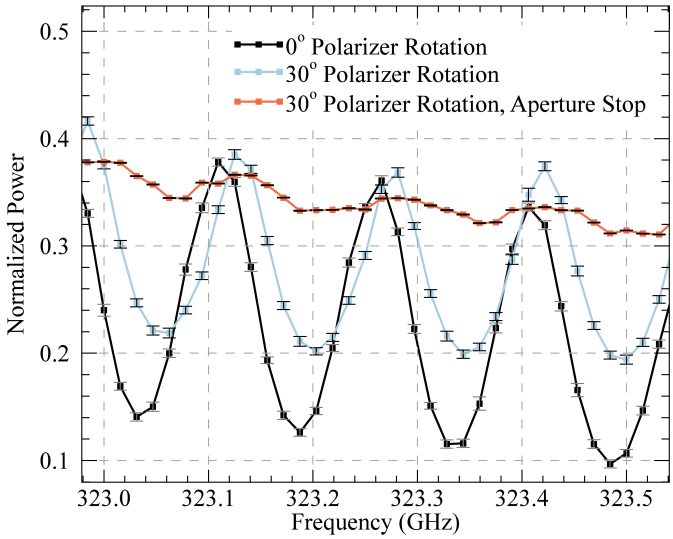

Figure 6.10: A subsection of the data from Figures 6.9 and 6.16 between 323.0-323.5 GHz. The power measured for a perpendicular polarizer (black) shows fringes with a spacing of $\Delta\bar{f} = 0.15 \pm 0.03$ GHz. Error bars represent $10\times$ the standard deviation of 100 data points.

6.4.1 Fabry-Pérot Resonances

The resulting interference pattern is analogous to that produced by a Fabry-Pérot etalon [6]. The Fabry-Pérot etalon is device that consists of two parallel reflecting surfaces separated by a fixed distance, l, that encloses a medium with a refractive index, n. Incident light at an angle, θ, undergoes multiple reflections between the two reflecting surfaces. Considering only the first reflection, an optical path difference between primary transmitted beam, T_1, and the secondary transmitted beam due to a reflection, T_2, results in a phase difference

$$\phi = \left(\frac{2\pi}{\lambda}\right) 2ln\cos\theta. \tag{6.7}$$

When the $\phi = 2m\pi$, the electric fields of the primary and secondary transmitted waves interfere constructively, resulting in a maximum field amplitude of $(E_2 + E_1)$ and intensity $(E_2 + E_1)^2$.

In terms of the THz testbed, any resonant cavity within the system that could allow for the propagation of multiple reflected beams to reach the detector will cause resonant

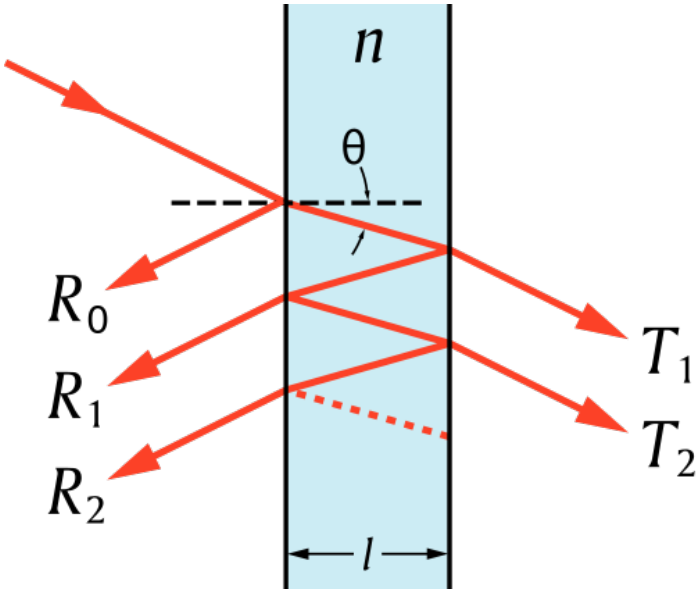

Figure 6.11: Multiple internal reflections R in a Fabry-Pérot etalon of length, l, with an internal medium of index n [4]. Light is incident at an angle θ. Transmitted light, T, has phase differences given by Equation 6.7.

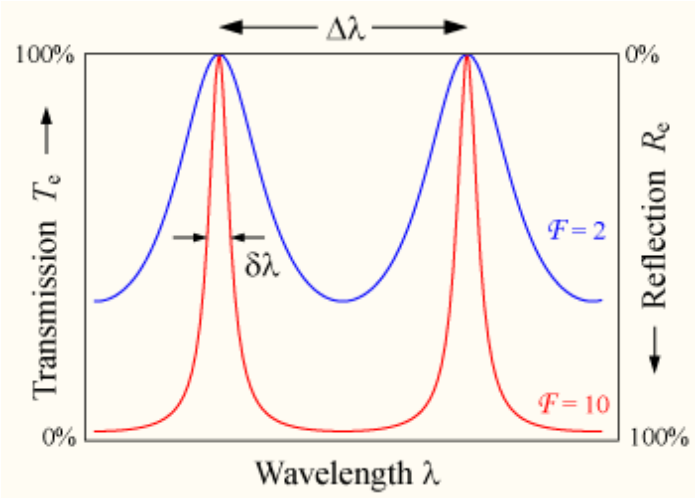

Figure 6.12: Transmission in a Fabry-Pérot etalon with a constant cavity length, l [5]. Narrow peaks are said to have a high *finesse*, $\mathscr{F}$, which is the result of more reflections that interfere constructively [6].

fringes similar to that in a Fabry-Perot elaton, as shown in Figure 6.12. Considering that the incident beam is at approximately normal incidence ($\theta = 0°$) and air is the medium between the reflecting surfaces, the phase difference in terms of the frequency of light, f, is

Table 6.2: Lengths of potential resonant cavities in the THz testbed, as shown in Figure 6.13. Error is the largest standard deviation in measured distances. Distance PD was difficult to measure due to the polarizer being close to the ZBD and is given as an approximation.

Path	Length (cm)
SD	98.36 ± 0.03
PD	≈ 2.5
SP	100 ± 1

$$\phi = \left(\frac{2\pi f}{c}\right) 2l. \tag{6.8}$$

Potential cavities in the testbed with a physical length l have been identified in Figure 6.13, where "S" denotes the front face of the input horn,"P" the location of the wire-grid polarizer, and "D" the front face of the detecting horn. Table 6.4.1 summarizes the measured physical path lengths associated with potential cavities.

For an unknown, fixed round-trip path length $2l$, the ZBD will measure maxima at frequencies when Equation 6.8 satisfies the condition of constructive interference. The spacing between fringes in the system, given by Δf, can be used in Equation 6.8 to calculate the corresponding length l of the cavity.

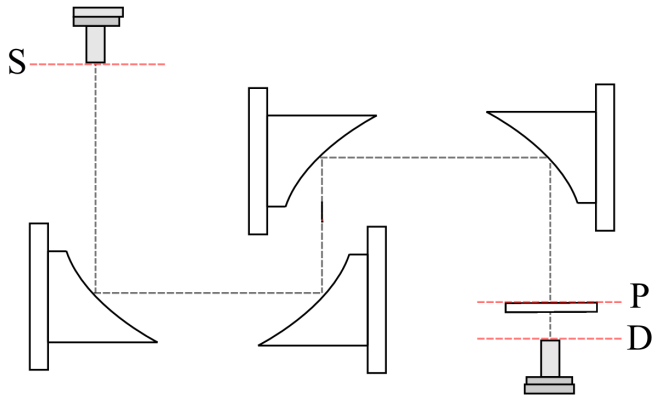

Figure 6.13: Potential reflective surfaces in the THz testbed.

Furthermore, the interference pattern in Figure 6.16 resemble two unequal-amplitude

harmonic waves of different frequencies superimposed to produce a beat pattern. This implies that there are two resonant cavities with fringe spacings Δf_1 and Δf_2. Together, these cavities result in a modulated fringe pattern with a modulated and average fringe spacing given by

$$\Delta f_m = \frac{2(\Delta f_1 \Delta f_2)}{\Delta f_2 - \Delta f_1} \tag{6.9}$$

and

$$\Delta \bar{f} = \frac{2(\Delta f_1 \Delta f_2)}{\Delta f_2 + \Delta f_1}, \tag{6.10}$$

respectively. The measurement of these values are given in the next section.

6.4.2 Fringe Spacing

To calculate the fringe spacing, local extrema were found by noting where the derivative of the measured data with respect to frequency changed sign. A cubic spline was used to interpolate the data in a region of approximately ± 2 points surrounding the local extrema. The interpolated data were again checked for a maximum/minimum value. An average fringe spacing of $\Delta \bar{f} = 0.149 \pm 0.005$ GHz was calculated by taking the mean difference between the location of successive minima and maxima. Using these minima and maxima, the modulation envelope was plotted in Figure 6.15. The fringe spacing of the envelope was calculated to be $\Delta f_m = 2.8 \pm 0.2$ GHz.

The spacings $\Delta \bar{f}$ and Δf_m correspond to two individual fringe patterns with spacings of $\Delta f_1 = 0.1452$ GHz and $\Delta f_2 = 0.1531$ GHz. However, propagating the errors in Δf_m and $\Delta \bar{f}$ leads to a high 8% error. Consequently, Δf_1 and Δf_2 are only known to ± 0.01 GHz and $\Delta f_1 \approx \Delta f_2 = 0.15$ GHz. This corresponds to a physical path length of $l = 100 \pm 8$ cm, which is within error of both SP and SD.

Further evidence that these are the two contributing paths is shown in Figure 6.16, where the modulation was significantly reduced by tilting the polarizer approximately 30°

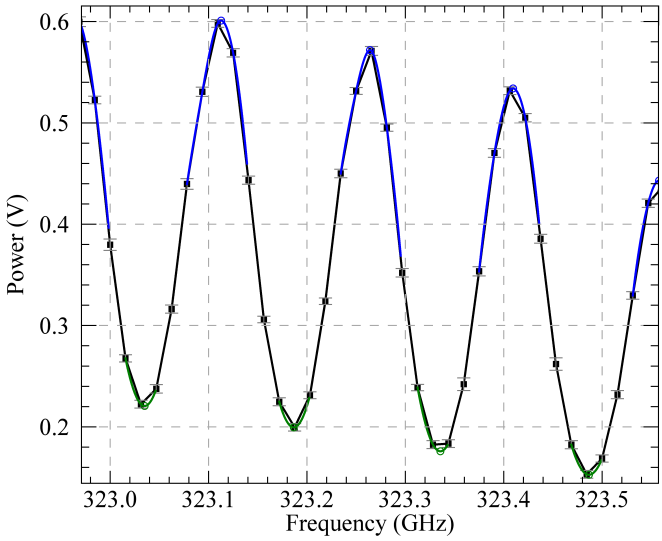

Figure 6.14: Visual representation of the routine to find local extrema. The black curve is a subsection of the ZBD data from Figure 6.16 with the polarizer placed perpendicular to the optical axis. Blue and green curves show the interpolated data over a small region. Open blue and green circles show the extracted local extrema. The difference between successive minima/maxima was taken to determine $\Delta\bar{f} = 0.149 \pm 0.005$ GHz.

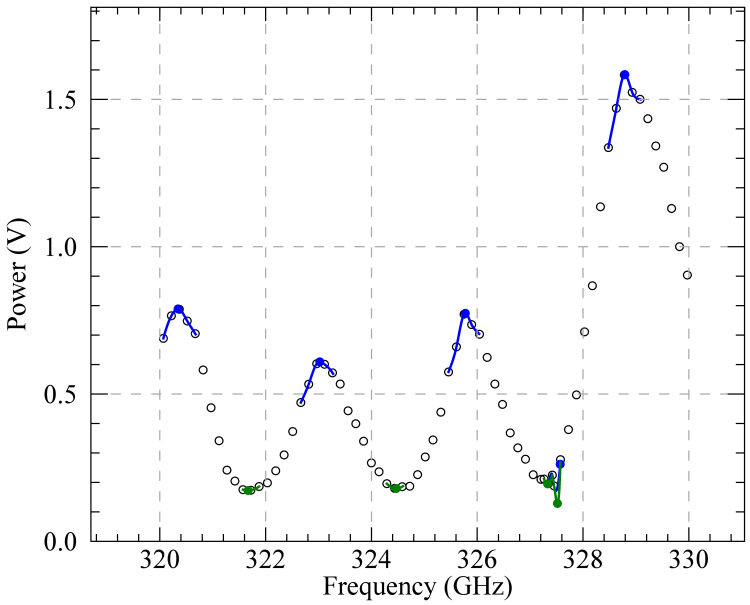

Figure 6.15: The envelope of the power measurements. Local extrema were found using the method described in the text. Extrema around 327 GHz were incorrectly extracted by the routine and were visually inspected. The fringe spacing was found to be $\Delta f_m = 2.8 \pm 0.2$ GHz.

with respect to the plane perpendicular to the optical axis. This would cause unwanted reflections to reflect at an angle of 30°, thereby not contributing to the observed interference, leaving the path between the source and detector as the primary source of fringing. In this configuration, a measured fringe spacing of $\Delta f = 0.146 \pm 0.003$ GHz gives a physical path length of $l = 103 \pm 2$ cm. Therefore, it is evident that reflections between the detector and source is the primary optical cavity in the system.

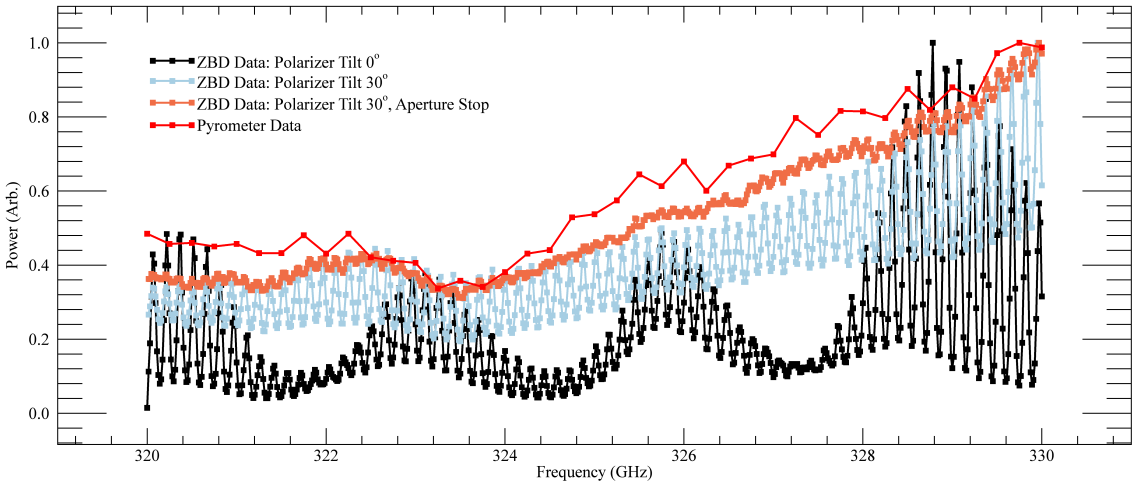

Figure 6.16: Measured power output from the VDI source for different optical configurations. Black: polarizer placed perpendicular to the optical axis (rotation of 0°). Blue: polarizer rotated 30° CCW from the optical axis. Orange: polarizer rotated 30° with a $\approx$ 17 mm diameter stop placed in the parallel beam between mirrors M1 and M2 (see Figure 6.1). Error bars are suppressed for clarity and are shown in Figure 6.10.

To investigate this further, an aperture stop with a diameter of approximately 17 mm was then placed in the parallel beam between mirrors M1 and M2, reducing the available beam power that can contribute to the observed fringing (Figure 6.16, black curve). Fringe spacing was measured to be $\Delta f = 0.14 \pm 0.06$ GHz ($l = 100 \pm 5$ cm), which has a larger error due to the small amplitude of the fringe.

As a final test, the ZBD was replaced by a pyrometer. A pyrometer is a bolometric detector with a flat frequency response. Although less sensitive, these measurements had an overall similar result.

The source power measured with different testbed configurations highlights the diffi-

culty measuring transmission as a function of frequency. The changing fringe pattern between the reference power measurement and that with an aperture placed at the focus would introduce errors if used to directly normalize the transmitted signal. An optical isolator arrangement, consisting of a quarter wave plate and linear polarizer, is a potential solution. However, the frequency-dependent nature of quarter wave plates limits the efficiency of the isolator unless operating at its designed wavelength.

Due to these challenges, transmission measurements through single apertures and bullseye lenses, presented in the following chapter, are performed at a single frequency. With a device placed at the focus, the optical cavity is optimized for to the nearest fringe.

Chapter 7

Transmission Measurements

This thesis has concerned itself with the development of plasmonic lenses. The primary goal of plasmonic lenses is to increase the transmission over that obtained with a single aperture of identical diameter and thickness. To confirm that the response of a lens agrees with the simulated model, transmission measurements are required. Considering that the source power varies with frequency, as discussed in the previous chapter, all measurements were taken at a fixed frequency. Furthermore, since fringes arise due to resonant cavities within the system, an alignment procedure was followed to optimize the signal on a specific resonance (Section 7.1). Since the output power of the source cannot be determined with accuracy, the signal measured through a plasmonic lens will be compared to that of a single aperture to confirm enhanced transmission (Section 7.3).

7.1 Aperture Mounting and Alignment

The error bars presented in this chapter are a measure of the stability of the source (as will be shown in Section 7.3). However, the highly resonant nature of the system leads to larger errors due to the misalignment of apertures. The testbed is a multiply reflecting cavity, as discussed in Section 6.4.1, and misalignments along the z-direction correspond to a change in the physical path length of the cavity. A rule of thumb is to align the system within 10° of phase, which corresponds to $\approx$ 30 μm for our THz source. Furthermore, because of the multiply reflecting beams, misalignments are amplified. The required alignment precision of components in the cavity, both in position and tilt, becomes increasingly

important.

To position the central aperture with precision control, all devices were placed on a 3-axis assembly consisting of two Newport M-SDS40 Metric Linear Translation Stages with 10 μm divisions and an Edmund Metric Z-Axis Stage [99, 105]. An optical axis, used to define the height of each component, was established using a vernier height gauge. Single apertures milled in shim stock were fastened to a Newport LH-2 lens mount on an optical post and holder. Bullseye devices were mounted in a custom machined frictional mount designed to induce minimal stress on the lens, which consists of a metal frame with a screw used to release the bullseye.

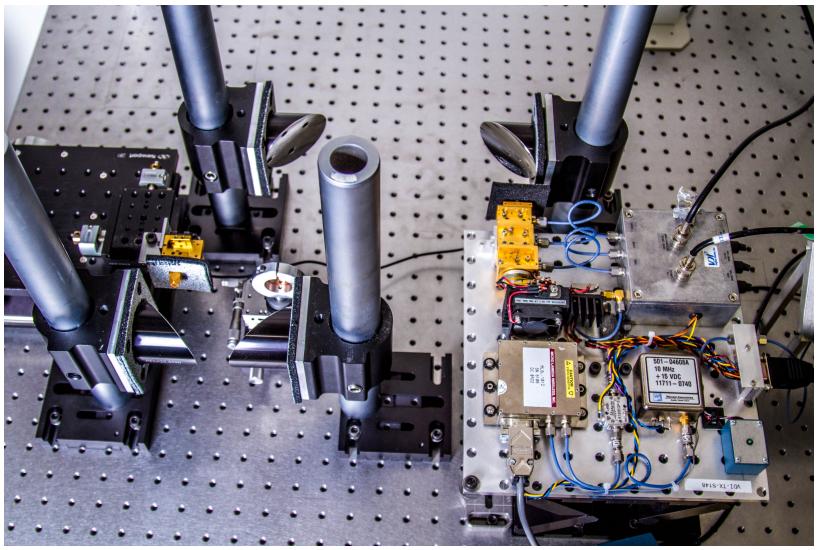

Figure 7.1: The testbed configuartion used to measure transmission through the bullseye lenses. The Gaussian source is collected and collimated by f/1 and f/3 mirrors, respectively. The bullseye device is placed at the location of the focus and the input rings are illuminated with a magnified beam waist of $w_0 \approx 5.1$ mm.

With a device placed at the focus, an alignment procedure was adopted to maximize the signal by iteratively adjusting the position in the z-direction, the position in xy-direction, and the rotation of the device. This was performed by carefully making adjustments and viewing the lock-in signal on an oscilloscope until no further improvements were observed. The shifts in the xy-direction aligned the aperture with the axis of the beam. Alignment errors in this direction are more forgiving; a 100 μm change in the transverse directions

lowered the measured signal by $\approx 7.5\%$. In the z-direction, it was noted that a shift of 10 μm also lowers the measured signal by $\approx 7.5\%$, showing the increased sensitivity when the cavity length is changed.

7.2 Subwavelength Apertures

Circular apertures with diameters from $200 - 800$ μm were milled in brass shims with measured thicknesses of 25 ± 1 μm and 51 ± 1 μm. An image of a typical aperture is shown in Figure 7.2. Diameters were measured by using imaging software to calculate the area of the circular aperture and subtracting the area of irregularities along the contour of the aperture [106]. An effective diameter was then calculated and scaled using a reference $\mu m \cdot px^{-1}$ measurement. Error in the aperture diameter was calculated assuming 2% error in the measured scale. A summary of the measured aperture dimensions are given in Table 7.1.

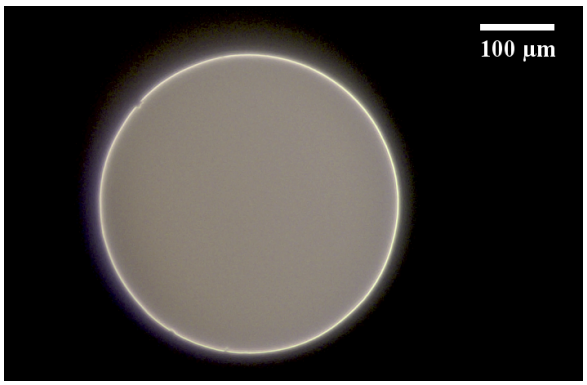

Figure 7.2: A $d = 398 \pm 11$ μm aperture milled in 25 ± 1 μm shim.

The optics of the THz testbed were configured to re-image the emitted THz beam with unit magnification. The source wavelength was set to $\lambda = 922$ μm. Knife-edge beam profiling measurements, as discussed in Section 6.3, determined the location of the focus and the waist size. The waist was measured to be 1.7 ± 0.2 mm, which is in excellent agreement with the predicted value of 1.682 mm. Individual apertures were then placed at the location of the focus and aligned as described in Section 7.1.

The transmitted signal was represented as the mean and standard deviation of a 10 s

Table 7.1: The measured diameters of circular apertures milled in brass shim.

Thickness $= 25 \pm 1$ μm	
Target Diameter (μm)	Measured Diameter (μm)
200	200 ± 6
300	299 ± 8
400	398 ± 11
500	497 ± 14
600	597 ± 17
700	695 ± 19
800	793 ± 22
Thickness $= 51 \pm 1$ μm	
Target Diameter (μm)	Measured Diameter (μm)
200	199 ± 6
300	294 ± 8
400	397 ± 11
500	495 ± 14
600	593 ± 17
700	697 ± 20
800	796 ± 22

measurement sampled at 1 kHz. As discussed in Section 4.2, the transmission efficiency, η, is defined as the ratio between the transmitted power, P_{out}, and the power incident on the aperture area, P_{in}. Since the absolute power from the source, P_0, is only known with an accuracy of 20%, measured transmission values were normalized by the fraction of the source power incident on the aperture, P_{in}/P_0, from Equation 4.19:

$$P_{out}\left(\frac{P_0}{P_{in}}\right) = P_0 \cdot \eta, \tag{7.1}$$

That is to say, the transmission efficiency was scaled by the source power. Scaled transmission efficiencies are plotted as a function of d/λ in Figure 7.3.

As can be seen, the transmission increases as the diameter becomes larger and begins to level off. For all measurements, thicker apertures attenuate the transmission. Furthermore, there is another dependency that is difficult to ascertain; as the aperture size increases, the surface area able to reflect light back into the cavity becomes less. Furthermore, wrinkles

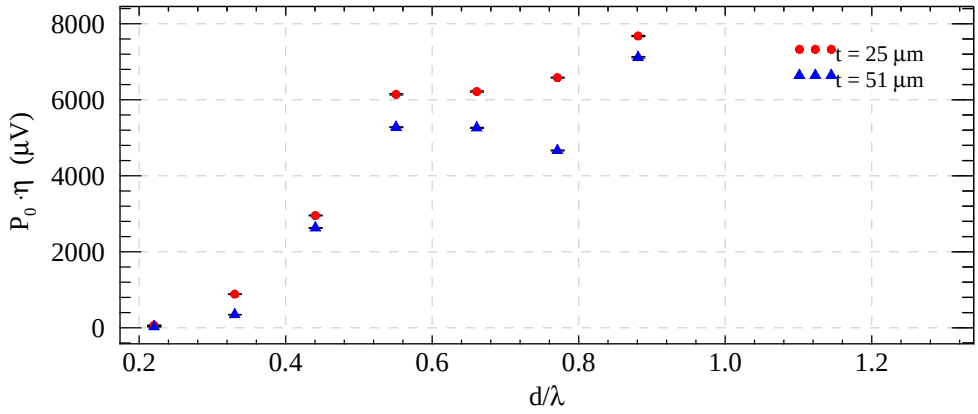

Figure 7.3: The measured transmission efficiency, η, scaled by the source power, P_0, through circular apertures milled in 25 μm and 51 μm shim (Table 7.1).

in the surface of these thin samples would further reduce the number of reflections. These results serve to show the general trends when performing aperture measurements. It is clear that the transmission depends on the diameter and thickness of the aperture.

7.3 Performance of Bullseye Plasmonic Lenses

Section 5.1 presented the simulated response of bullseye plasmonic lenses to incident Guassian beams of varying radii. Results showed that the transmission enhancement increased as an increasing number of ridges were illuminated. Given the limited choice of the off-axis parabolic mirrors available to us, the system was configured as shown in Figure 7.1 to illuminate 5 ridges (i.e., a waist of $w_0 \approx 5.1$ mm). The source wavelength was set to $\lambda = 922$ μm. The bullseye devices were then aligned at the location of the focus and the signal was optimized using the procedure given in Section 7.1.

As discussed in Section 5.4, in the final fabrication, two bullseye lenses were made: (1) a single-sided device with ridges on the input face and (2) a double-sided device with identical input ridges and radially-tuned output ridges. The transmission enhancement of these devices was calculated under the assumption that the transmission through the single-sided bullseye lens with the planar side facing the incident beam would be identical to that

of a hole in a thin aperture. However, it was noted that transmission through this reversed structure could be increased due to the beaming pattern produced by the input grooves on the reverse side, which may allow for more light to be collected within the acceptance angle of the collecting mirror.

The interpretation of the transmission measurements depends on the stability of the configuration. Despite the fact that Fabry-Perot cavities exist, which make the setup sensitive to vibrations, the system has proven to be extremely stable. Measurements of the source alone showed that the output power is stable to 1 part in 25 million.

By way of illustration, Figure 7.4 shows the signal recorded through the single-sided bullseye with ridges illuminated, from which a signal-to-noise ratio (SNR) of 1000 was derived. The digitization of the signal output from the digital-to-analogue converter is contained within the high-frequency hash. The large swings in the signal are believed to be due to variations in atmospheric transmission, such as changes in air currents, density, or water vapour content.

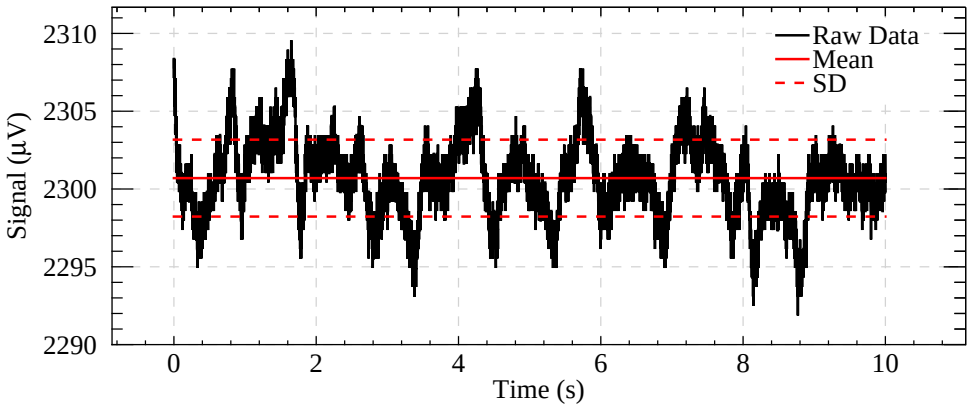

Figure 7.4: A 10 s measurement of the signal transmitted through the single-sided bullseye with input ridges illuminated (sampled at 1 kHz).

As discussed in Section 5.4, the transmission enhancement predicted from FDTD simulations was $G = 29 \pm 2$ at $\lambda = 922$ µm. Table 7.2 show the measured gain through the single-sided lens. We are realizing gains on the order of 20. While this is lower than the

Table 7.2: Transmission measurements of the single-sided bullseye in two configurations. P_{out} is the measured signal, ΔT is the measurement time, and f_s is the sampling rate. A $\lambda = 922$ μm incident Gaussian beam with a waist radius of approximately 5.1 mm was incident on the input ridge surface and the planar output surface. The transmission enhancement, G, was calculated with respect to the illumination of the planar side. In each case, the calculated error in G was approximately 1%, dominated by the SNR of the single-sided planar measurement.

Device	Side Illum.	P_{out} (μV)	ΔT (s)	f_s (kHz)	SNR	G
Single-sided	Planar	110 ± 1	20	1.0	200	–
Single-sided	Input	2300 ± 2	10	1.0	1000	21.0 ± 0.2
Single-sided	Input	2350 ± 4	20	1.0	600	21.4 ± 0.2

predicted value, it validates that a plasmonic lens has been built.

Table 7.3 summarizes transmission measurements through the double-sided bullseye. Although the transmission was enhanced, it was lower than the single sided device. It was noted that the surface of the lens around the rings was dimpled due to challenges in milling on both sides of the device. The output surface of the lens was clearly concave, as shown in Figure 7.5. Knowing that the surface was convex on the input side, it was hypothesized that the transmission could be increased by matching the wavefront to the curvature of input face of the lens. This required moving the bullseye out of focus, as shown in Figure 7.6.

Table 7.3: Transmission measurements of the radially tuned bullseye. Measurements were performed with the same source settings as described in Table 7.2. The signal of the radially-tuned device increased by a factor of approximately 2.3 when defocused to match the incident wavefront with the curvature of the surface.

Device	Side Illum.	P_{out} (μV)	ΔT (s)	f_s (kHz)	SNR	G
Single-sided	Planar	110 ± 1	20	1.0	200	–
Rad. Tuned	Input	1349 ± 2	10	1.0	600	12.3 ± 0.1
Rad. Tuned, Defocused	Input	3055 ± 2	1	0.1	1700	27.8 ± 0.3

The lens was then translated towards the source. Despite that the energy density on the aperture had been lowered as the lens is moved out of focus, the transmitted signal increased by a factor of approximately 2.3 and reached a maximum gain of 27.8 ± 0.3. This is in excellent agreement with the simulated $G = 29 \pm 2$, clearly demonstrating the designed

plasmonic effects.

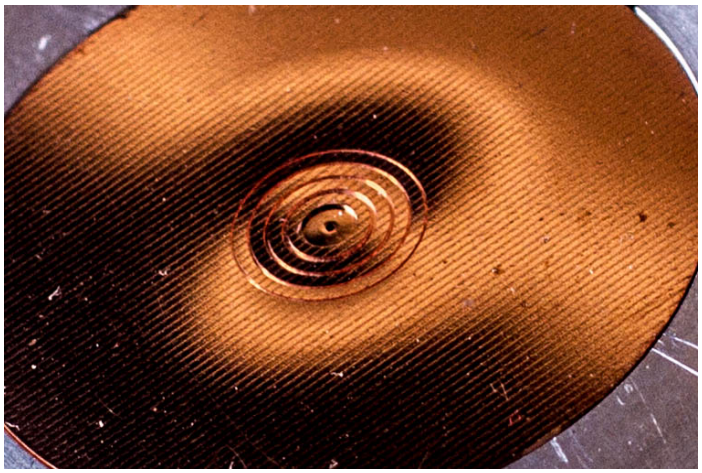

Figure 7.5: The output surface of the double-sided bullseye. It was noted that the output surface had concave curvature. I.e., the input surface would have convex curvature.

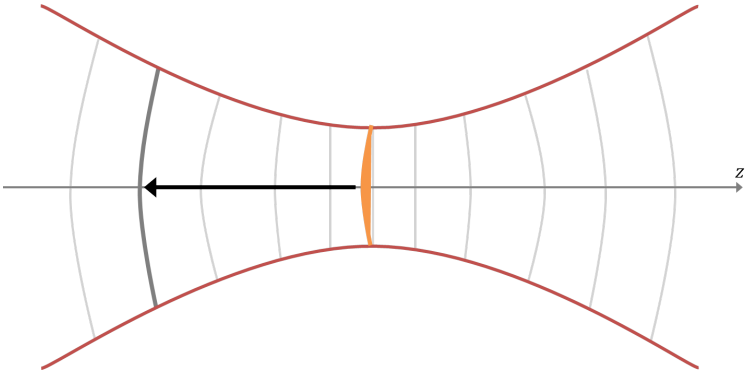

Figure 7.6: The convex input plane of the radially-tuned device was shifted from the location of a planar wavefront towards the source to match the curvature of the wavefront.

To examine this further, a wavelength sweep was performed over the region of the local fringe at 922 μm for all bullseye configurations, as shown in Figures 7.7. The in-focus double-sided bullseye (yellow) exhibited a wider fringe than the single-sided device (blue). This implies that double-sided device, in this configuration, is not matched with the planar wavefront due to its concave surface. This de-resonates the system and reduces the number of constructive reflections and therefore the sharpness of the fringe. When translated away from the focus, the curvature of double-sided bullseye roughly matches that of the incident wavefront and the width of the peak decreases.

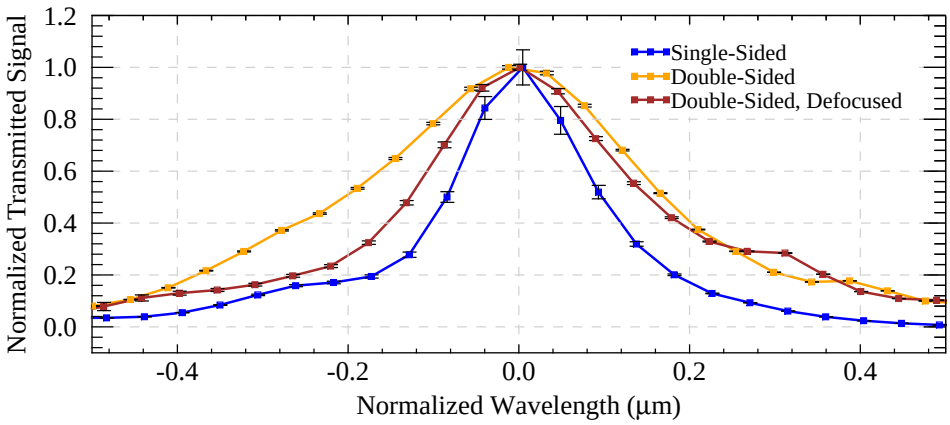

Figure 7.7: A wavelength sweep around resonant fringe where transmission measurements were performed. The transmitted signal has been normalized to unity and the wavelength scale has been normalized to the peak location.

The double-sided bullseye exhibited plasmonic effects, but the structuring of the surface on both sides evidently poses problems. In future devices, care will be taken to ensure that the surface of the lens is planar to maximize the cavity resonances. Despite this difficulty, the enhancement gain achieved agrees with that predicted by simulations confers a large system signal-to-noise .

Chapter 8

Conclusions

Plasmonics is an emerging field, one often made more difficult to understand due differences in terminology. The fundamental properties of SPPs can be described using electromagnetic theory. The majority of research is focused at visible frequencies, for reasons partially due to data storage applications driven by the entertainment industry, where devices are manufactured with nanofabication techniques. Fewer groups work at longer wavelengths. However, it has been shown that the optimum frequency for differentially diagnosing breast cancer occurs around 325 GHz (Chapter 1). At this frequency, the spatial resolution of conventional imaging configurations is on the order of 1 mm and could benefit from near-field imaging using subwavelength apertures. This thesis set out to show that we could design, fabricate, and evaluate a plasmonic lens that would provide enhanced transmission at THz frequencies to allow such measurements.

While much work is done at visible wavelengths, there is little data in the published literature for the material properties at THz frequencies. Fortunately, at these long wavelengths most metals behave as perfect electrical conductors, as established in Chapter 2 using Drude model parameters. A theoretical description of SPPs was given in Chapter 3 and a description of how the transmission through subwavelength circular apertures depends on the aperture diameter and thickness was given in Chapter 4. The design of bullseye lenses was systematically studied using FDTD techniques by adapting basic scale laws to perfect metals (Chapter 5).

A THz testbed was developed (Chapter 6) to measure the performance of the designed

devices. Initially, a prototype bullseye lens with surface grooves was fabricated. Results from this lens have not been reported here, as this model inherently has a thick aperture that leads to low power transmission. Nonetheless, it verified the working principle of the testbed and that thinner devices were required.

Subsequently, a ridge model was adopted, whose thickness was reduced to 50 μm. Designs and their experimental response were presented (Chapter 7). From the first results, it was clear that enhanced transmission had been achieved that could only be explained by the presence of surface plasmon polaritons. The theory showed estimated gains over an aperture with identical diameter and thickness of $G = 29 \pm 2$. With a single-sided lens, a gain of 21.4 ± 0.2 was observed. With a double-sided lens, a gain of 12.3 ± 0.1 was observed. Upon further inspection of the double sided device, the fabrication of both sides of the device resulted in a convex surface on the input side. To validate this argument, the double-sided device was moved out of focus in an attempt to roughly match the curvature of the lens to the curvature of the wavefront. The resulting signal increased to 27.8 ± 0.3. This marked increase, when the energy density on the aperture was decreasing, clearly showed that curvature of device was playing an important role.

More importantly, with the designed system a signal-to-noise ratio on the order of 1000 was achieved in a 20 second measurement. This time was chosen to because it represents the time it takes to scan a 1 cm by 1 cm biopsy sample in steps of 100 μm. In order to ascertain if this sensitivity was sufficient to differentiate cancer from non-cancerous material, attention must be turned to absorption spectroscopy. The attenuation of light travelling through a sample is described by the Beer-Lambert law to be $I = I_0\, e^{-\alpha x}$ ($\mathrm{W \cdot m^{-2}}$), where I_0 is the intensity of the incident radiation, α ($\mathrm{mm^{-1}}$) is the intensity attenuation coefficient and x (mm) is the distance the light travels through the material [107].

For the diagnosis of cancer, the imaging system must be able to distinguish the adsorption coefficients of cancerous tissue ($10.5\ \mathrm{mm^{-1}}$) from that of fibrous tissue ($8.25\ \mathrm{mm^{-1}}$) [39]. If a slide was cut with a thickness of 20 μm, 81% of the incident power is transmitted

through tumours and 85% transmission through fibrous tissue. These quantities are separated by approximately 4 parts in 80, requiring a minimum signal-to-noise ratio of approximately 20. The designed system surpasses this by nearly 2 orders of magnitude, allowing a difference of 0.08% to be measured.

This thesis has cumulated in the fabrication a bullseye plasmonic lens whose aperture diameter would confer a spatial resolution of 300 μm in a near-field imaging configuration. The device that shows a transmission enhancement of 27.8 ± 0.3, providing a sensitivity 50 times larger than required. The next immediate step is to migrate the plasmonic lens in a THz microscope in an attempt to measure breast cancer.

To our knowledge, this is the first time a plasmonic lens has been made using micromachining techniques. Several lessons were learned in the process. While the cost of these devices are not dissimilar from nanofabrication, nanofabrication lends itself to mass production. Additionally, a silicon wafer would maintain a planar surface.

This thesis has explored the new area of THz plasmonic devices. Theory has allowed us to not only confirm, but extend the rules of thumb for the design of lenses, such as the inclusion of Bragg reflectors for further enhancement and the tailoring of output ridges to produce a spatially confined output beam. It has been shown that devices can be fabricated using micromachining techniques. The lenses produced have been shown to agree well with the theoretical prediction and have set the stage for the subwavelength imaging of cancer.

During the course of this study, it was found that the system is currently limited by the digital-to-analogue converter that outputs the lock-in signal. Future work will be focused on the use of a higher resolution digital-to-analogue converter to further reduce the noise. The next round of fabrication will explore the use of a single-sided device with a smaller aperture and look at ways to maintain an even, planar surface.

Appendix A

Surface Plasmon Approximations at THz Frequencies

A.1 Propagation Length

Due to the large permittivity values of materials at THz frequencies, useful approximations can be made for the propagation length and skin depths of surface plasmons. The SP propagation constant given by Equation 3.16 can be simplified by first considering the quantity

$$\begin{aligned}\frac{\varepsilon_m\varepsilon_d}{\varepsilon_m+\varepsilon_d} &= \frac{\varepsilon'_m\varepsilon_d+i\varepsilon''_m\varepsilon_d}{(\varepsilon'_m+\varepsilon_d)+i\varepsilon''_m} \\ &= \frac{\varepsilon'_m\varepsilon_d+i\varepsilon''_m\varepsilon_d}{(\varepsilon'_m+\varepsilon_d)+i\varepsilon''_m}\times\frac{(\varepsilon'_m+\varepsilon_d)-i\varepsilon''_m}{(\varepsilon'_m+\varepsilon_d)-i\varepsilon''_m} \\ &= \frac{\varepsilon'^2_m\varepsilon_d+\varepsilon'_m\varepsilon_d^2+\varepsilon''_m\varepsilon_d}{(\varepsilon'_m+\varepsilon_d)^2+\varepsilon''^2_m}+i\frac{\varepsilon''_m\varepsilon_d^2}{(\varepsilon'_m+\varepsilon_d)^2+\varepsilon''^2_m}.\end{aligned} \tag{A.1}$$

For an air-metal interface at THz frequencies, $\varepsilon_d = 1$ and metallic permittivity values are on the order of 10^5 to 10^6 (Section 2.4) with $\varepsilon''_m > |\varepsilon'_m|$. The above can then be approximated as

$$\frac{\varepsilon_m\varepsilon_d}{\varepsilon_m+\varepsilon_d} \approx 1+\frac{i}{\varepsilon''_m}. \tag{A.2}$$

The square root in Equation 3.16 can then be approximated by making use of the Taylor expansion

$$\sqrt{1+x} = 1+\frac{x}{2}-\frac{x^2}{8}+\frac{x^3}{16}-\ldots \tag{A.3}$$

Letting $x = i\frac{1}{\varepsilon''^2_m}$ and taking only the first two terms leaves

$$k_x = k_0\sqrt{\frac{\varepsilon_d\varepsilon_m}{\varepsilon_d+\varepsilon_m}}$$
$$\approx k_0 + i\frac{k_0}{2\varepsilon_m''}. \tag{A.4}$$

At these long wavelengths, the real part of k_x approaches the free space wave vector, as can also be seen by the dispersion relation plotted in Figure 3.2. The imaginary part can then be used to approximate the propagation length as

$$L = \frac{1}{2k_x''} \approx \frac{\varepsilon_m''}{k_0}. \tag{A.5}$$

A.2 Metallic Skin Depth

The metallic skin depth can be approximated by taking Equation 3.15a (using the appropriate subscript $m = 1$) and noting that the $k_x^2 \approx k_0^2$:

$$k_{zm}^2 = k_0^2\varepsilon_m - k_x^2$$
$$\approx k_0^2(\varepsilon_m - 1). \tag{A.6}$$

Noting that $\varepsilon_m' \ll -1$,

$$k_{zm} = k_0\sqrt{\varepsilon_m} \tag{A.7}$$
$$= k_0\sqrt{\varepsilon_m' + i\varepsilon_m''}. \tag{A.8}$$

The square root of ε_m can be re-written as

$$\sqrt{\varepsilon_m} = \sqrt{\frac{\sqrt{\varepsilon_m'^2+\varepsilon_m''^2}+\varepsilon_m''}{2}} + \frac{\varepsilon_m''}{|\varepsilon_m''|}\sqrt{\frac{\sqrt{\varepsilon_m'^2+\varepsilon_m''^2}-\varepsilon_m''}{2}}. \tag{A.9}$$

Making use of the fact that $\varepsilon_m'' > |\varepsilon_m'|$, the imaginary part of k_{zm} is approximated as

$$k_{zm}'' \approx k_0\sqrt{\frac{\varepsilon_m''}{2}}. \tag{A.10}$$

The metallic skin depth is then

$$\delta_m \approx \frac{1}{k_0}\sqrt{\frac{2}{\varepsilon_m''}}. \tag{A.11}$$

Appendix B

Finite-Difference Time-Domain Simulations

Predicting the behaviour of light in the presence of complicated boundaries is challenging and, in general, analytically solutions to Maxwell's equations do not exist. The finite-difference time-domain (FDTD) method is a state-of-the-art numerical technique used to compute the electromagnetic response of a device with complex geometry by solving Maxwell's equations on a discrete spatial and temporal rectangular grid [57]. The simulations presented in this were accomplished using Lumerical FDTD Solutions [52].

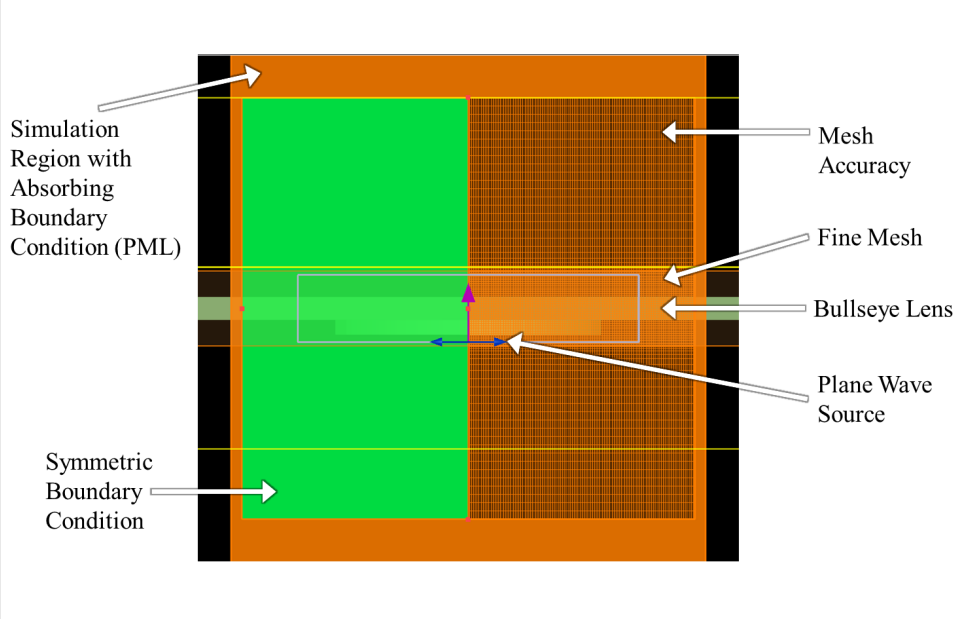

Figure B.1: The FDTD Solutions simulation region (orange) containing a bullseye lens with input grooves (dark green). A plane wave source (grey box) illuminates the bullseye lens, which is surrounded by a fine mesh region (centre).

I developed a fully parametrized bullseye lens model within FDTD Solutions that can be used to sweep the geometric parameters of the lens and simulation settings in a consistent manner. This model has the ability to simulate a single aperture surrounded by a combination of input/output grooves/ridges. Custom scripts were written to automate parameter sweeps and export relevant power, electric field, and phase data. To illustrate the

use of FDTD Solutions, Figure B.1 shows a cross section of the simulation region. Located at the centre is a bullseye lens with input grooves. The simulation methodology can be complicated and may lead to mistakes in the setup of the simulation itself and in the interpretation of results. Important considerations are: the simulation meshing, boundary conditions, electromagnetic sources, simulation monitors, and material properties. These individual issues are discussed in Section B.1. Convergence testing by systematically varying each parameter is essential to ensure that the simulation produces meaningful results. An example of convergence testing is presented in Section B.2. Lastly, a complete table of all simulations performed for this thesis is given in Section B.4 and includes the design of the simulated structure and simulation settings. For more information regarding the use of FDTD Solutions, the reader is directed to the Lumerical Knowledge Base [52].

B.1 Simulation Considerations

Meshing

A small spatial mesh allows for a more accurate calculation of the electromagnetic fields at the cost of increased simulation times and memory requirements. Since the mesh size is a measure of the precision of the geometric features, the precision of the manufacturing process places a pragmatic limit on the minimum mesh size (e.g., on the order of 10 nm for visible applications and 10 μm for THz applications).

FDTD Solutions generates an automatic, non-uniform mesh in the FDTD region (the orange grid shown in Figure B.1) based on the simulation wavelength, structure geometry, and material properties. This can be controlled by assigning a mesh accuracy value, which is related to the number of mesh points per wavelength. Different mesh refinement methods can be selected, including a staircased regular grid and conformal variants (which can resolve sub-mesh cell features). Conformal variants, however, can lead to numerical problems with coarse meshes. Early simulations showed predictable results with a staircase mesh. An additional mesh override region with a user defined mesh size was placed around the structure with features that must be resolved.

Boundary Conditions

The boundary of the simulation region was set to absorb all outgoing incident light from the simulation region so that reflected waves would not affect the computation. This is achieved by using a perfect matched layer (PML) boundary condition (shown in Figure B.1 as the thick, outer orange region). The PML effectively absorbs light at normal incident with a small, non-zero amount of reflection. This reflection increases for larger angles of incidence. Large reflections can reduce the accuracy of simulated power values. Therefore, it is crucial to ensure that reflections from the PML are low and that sources and structures are placed correctly within the simulation region. It is recommended that the PML boundary is at least half a wavelength away from the structure in either direction and that structures are extended through the PML boundary. Additional PML layers can be added, which aids in reducing reflections with the trade off of increased simulation time.

To reduce simulation times and memory requirements, symmetric boundary conditions (the light green region in Figure B.1) can be chosen, which allows the bullseye model to

simulate 4 times faster compared to a simulation without symmetric boundary conditions.

Plane Wave Sources

FDTD Solutions can inject plane waves and Gaussian beams into the simulation region. The use of these sources are subject to certain restrictions depending on the boundary conditions used at the edge of the simulation region. For example, a simple plane wave source injects a uniform electromagnetic field across the entire simulation region. When truncated at PML boundaries, this source exhibits diffraction effects analogous to a plane wave passing through an aperture. A total-field scattered-field source (TFSF), shown as a grey box in Figure B.1, addresses this by separating the field into two regions. Within the TFSF boundary is the total field, which includes incident wave plus the scattered wave, and outside is the scattered field.

Gaussian Sources

FDTD Solution has a Gaussian source that allows the user to specify either the beam waist radius, w_0, and distance, d, from the injection plane to the waist or by providing the beam radius, w_z, at the injection plane and the divergence half-angle, θ (Figure B.2). The values w_0 and d are internally converted to w_z and θ, and vice-versa, allowing the user to specify the pair that best describes the optical system. $d > 0$ corresponds to a diverging beam, i.e., the beam waist is behind the injection plane, and that $d < 0$ corresponds to a converging beam, i.e., the beam waist is ahead of the injection plane.

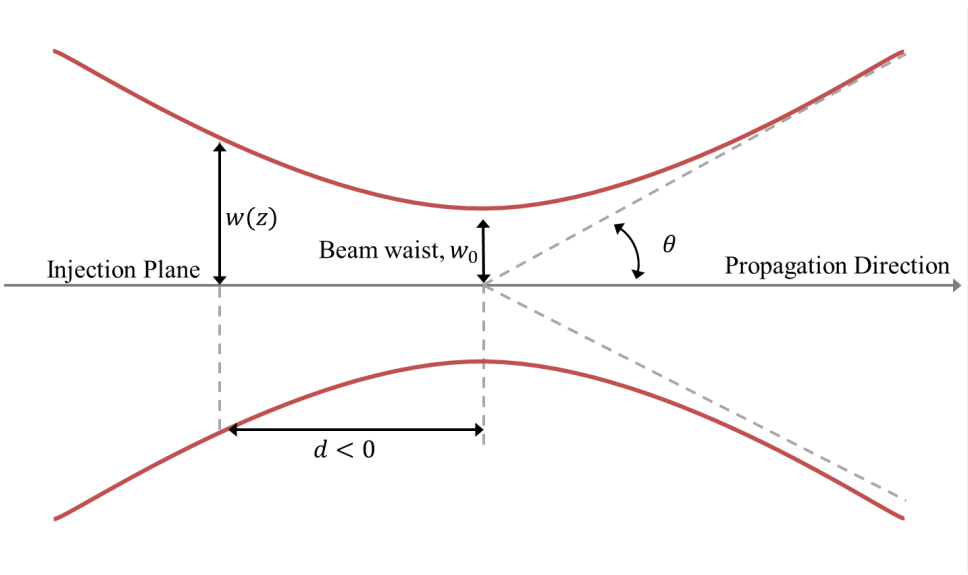

Figure B.2: The parameters used to specify a Gaussian beam in FDTD Solutions.

For example, to produce an Gaussian beam with beam waist incident at a desired location, the injection plane of the Gaussian source is placed at an arbitrary distance behind the aperture and d is chosen to be negative with an absolute value that is equal to the distance from the plane containing the beam waist. For a plane aperture or bullseye with input grooves, this plane is at the front of the aperture. For ridge designs, the waist is placed at

the plane defined by the top of the ridge. When comparing the transmission of Gaussian beams of different waist sizes, the amplitude of electric field must be normalized by $1/w_0$ to ensure that the output power of each source is the same.

Power Monitors

A frequency-domain field and power monitor is placed entirely in the scattered field region. To record all of the transmitted power, the collection angle of the monitor is increased by placing the monitor as close to the aperture as the simulation will allow. Monitors can be extended past the edge of the simulation boundary, in which case the software automatically truncates the monitor to the appropriate size.

While not immediately apparent, the TFSF source injects a plane wave into the entire simulation region. The absolute transmission value measured by power monitors only accounts for the power injected in primary injection plane, i.e., the size of the TFSF, not the total injected power. Care must be taken when calculating transmission efficiency described in Section 4.2.1 by normalizing the absolute transmission using the area of TFSF source.

Material Properties

FDTD Solutions includes a material database that can be fit with a proprietary multi-coefficient function or material models such as the Drude model. Since the primary usage of FDTD Solutions is for optical applications, the frequency dependent permittivity data that is included with the software, taken from public literature, falls outside of the simulation bandwidth required for THz applications. Since the properties of metals approaches that of a perfect electrical conductor at THz frequencies (Section 2.4), all simulated structures were assumed to be perfect metals. The surrounding medium was chosen to be vacuum.

Far-Field Projections

FDTD Solutions can perform post-simulation calculations that projects recorded near-field electromagnetic fields to the far-field. By recording the electromagnetic fields everywhere on a plane placed in a homogeneous material, the far-field projection calculates the field anywhere beyond the surface. This allows for the straightforward calculation of beam profiles at any distance beyond the aperture. This calculation was used to generate the beam profiles presented in this thesis.

B.2 Convergence Testing

The main parameters that contribute to simulation errors are the proximity of the PML boundary conditions, the allowed reflectivity of the PML boundary, the number of PML layers, the mesh-points per wavelength of the auto non-uniform mesh, and the grid size of the refined, uniform mesh. Each of these parameters were systematically varied over for a series of values. To quantify the convergence of the simulation when a given parameter was stepped from $i = 1, \ldots, N$, where i is the current step and N is the final step, the difference in the recorded transmission across the simulation bandwidth $T_i(\lambda)$ was compared to the transmission at the previous step using

$$\Delta T_i = \sqrt{\frac{\int [T_i(\lambda) - T_{i-1}(\lambda)]^2 \, d\lambda}{\int T_i(\lambda) \, d\lambda}}. \tag{B.1}$$

The quantity ΔT approaches zero as the model becomes converged or oscillates if another parameter is primary responsible for the error. If it is assumed that $T_N(\lambda)$ is close to the exact solution, and we are at the current step $i \ll N$, the error can be estimated as

$$\Delta T_n = \sqrt{\frac{\int [T_i(\lambda) - T_N(\lambda)]^2 \, d\lambda}{\int T_i(\lambda) \, d\lambda}}, \tag{B.2}$$

but is underestimated as $i \sim N$. Individual simulation parameters are examined in the following sections, the results of which are summarized in Table B.3.

PML Proximity

The span of the FDTD region in the z- and xy-directions were increased independently. By default, the parametrized bullseye design sets the span in the z-direction equal to the longest simulated wavelength and sets the xy-span to be 2.5 grating periods from the last groove. The parameters PML z-padding and PML xy-padding were introduced to increase the simulation span in either direction by a value in millimetres. A final value of 2 mm was chosen, contributing less than 0.01% error. In both directions, the PML distance was not a significant source of simulation error.

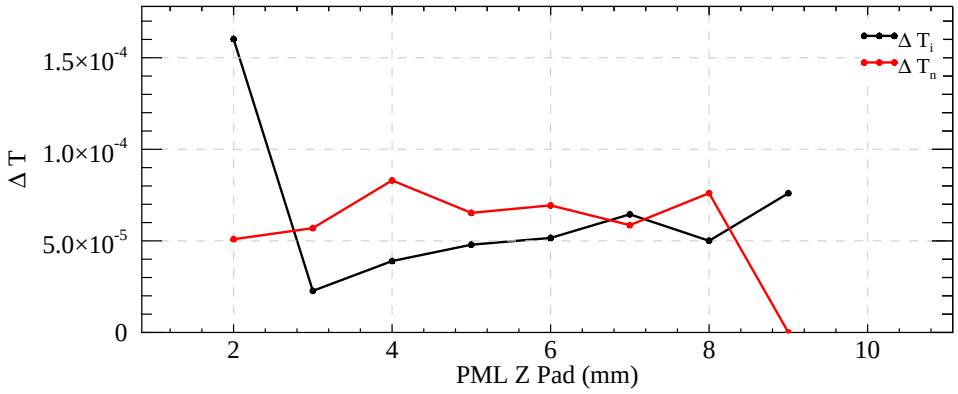

Figure B.3: Convergence test of the proximity to the PML boundaries in z-direction.

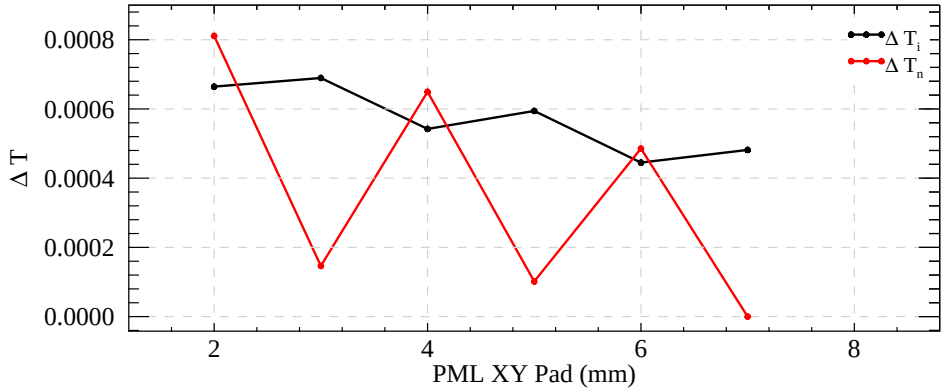

Figure B.4: Convergence test of the proximity to the PML boundaries in the xy-direction.

PML Reflectivity and Minimum Layers

As previously discussed, the PML boundary in Lumerical FDTD has non-zero reflectivity. If the amplitude of the reflected wave is non-negligible, reflections can re-interfere with the source or scattered fields, leading to incorrect transmission measurements and incorrect power normalization. The accepted reflectivity was swept on a log-scale and was shown not to be a significant source of error (Figure B.5), contributing approximately 0.01% error for a reflectivity of 1×10^{-10}.

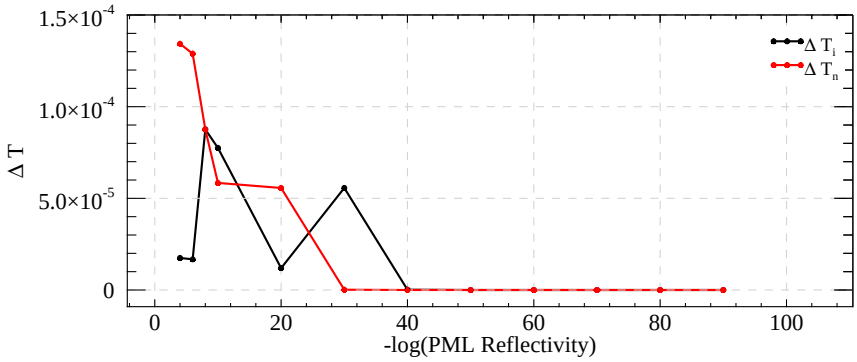

Figure B.5: Convergence test of the allowed PML reflectivity.

Likewise, the number of PML layers is not a significant parameter (Figure B.6). 12 PML layers contributes 0.01% error.

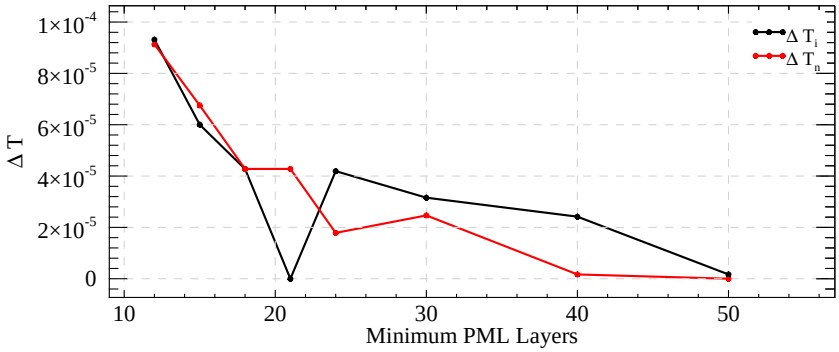

Figure B.6: Convergence test of the minimum number of PML layers.

Auto-Non Uniform Mesh Accuracy

The accuracy of the auto-non uniform mesh governs the number of points-per-wavelength (ppw) in the simulation region (excluding the refined mesh). A mesh accuracy of 1 corresponds to 6 ppw, an accuracy of 2 corresponds to 10 ppw, and onwards in steps of 4 ppw. It was not expected that this parameter would significantly contribute to the simulation error, as a refined mesh is placed around the structure of interest. A mesh accuracy of 2 was chosen, contributing an error of approximately 0.02%.

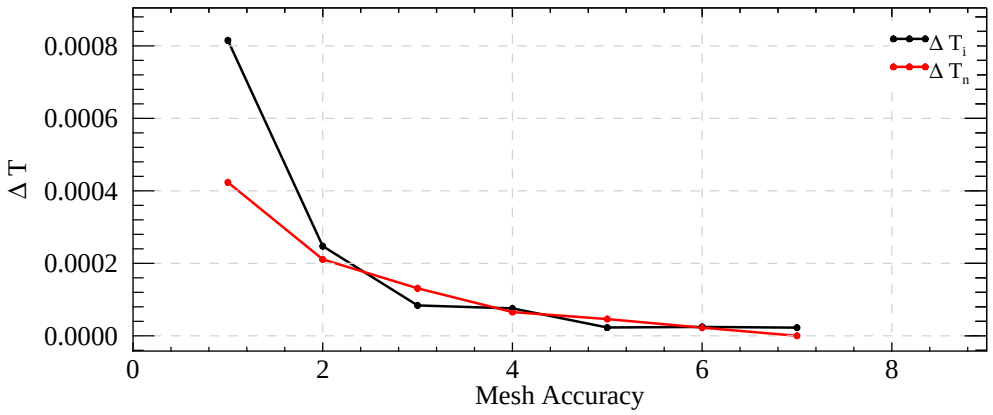

Figure B.7: Convergence test of the mesh ppw via the mesh accuracy setting.

Mesh Size

Intuitively a large source source of error, the size of the finite sized simulation mesh must be small enough to resolve the geometric features of the simulated structures. The peak of the resonance is shifted to lower wavelengths until the z-mesh size is reduced to 4 µm. Furthermore, absolute transmission values for coarser meshes, while qualitatively approximately the correct resonant behaviour, are over estimated. For mesh sizes below 4 µm, the absolute transmission oscillates around a mean value of $T = 8.7 \times 10^{-4}$ with 2% error. With this mesh size, smallest simulated surface feature in the xy-direction is sampled with ≈ 16 mesh points.

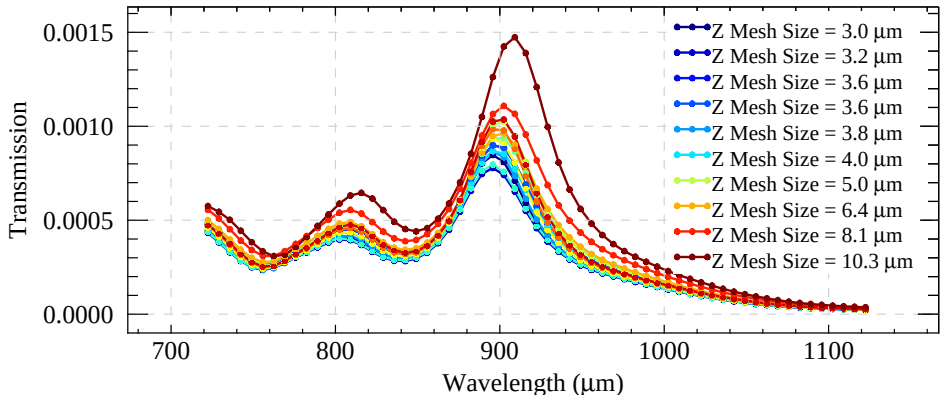

(a)

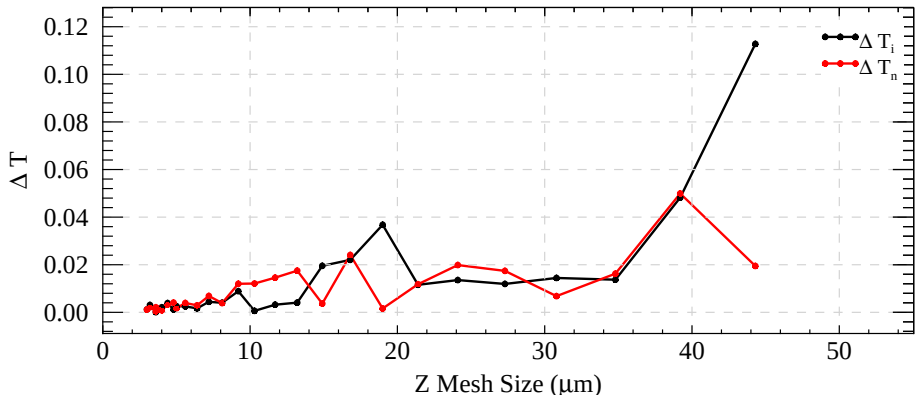

(b)

Figure B.8: Convergence test of the mesh size in the z-direction.

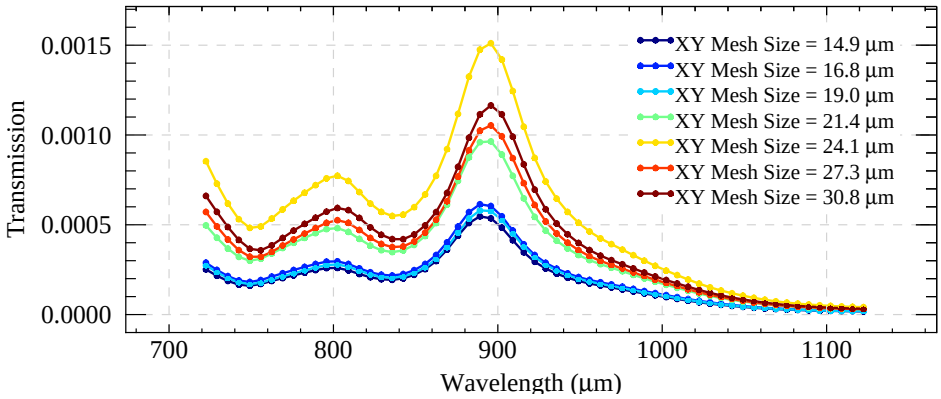

(a)

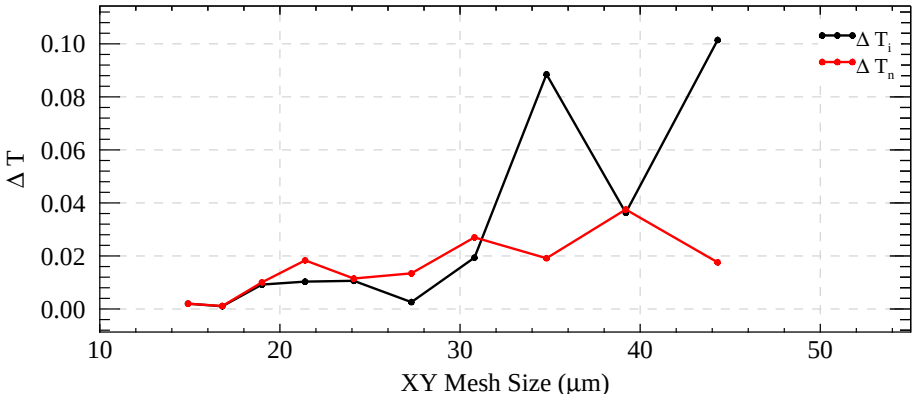

(b)

Figure B.9: Convergence test of the mesh size in the *xy*-direction.

A similar shift in the peak wavelength and in the converging of transmission values also is evident when the mesh size in the *xy*-direction is reduced to 19 µm, corresponding to 40 mesh points in smallest feature in the *z*-direction. The mean absolute transmission for mesh sizes smaller than 19 µm was $T = 5.8 \times 10^{-4}$ with 6% error.

B.3 Converged Parameters, Estimated Error, and Simulation Time

The results of each convergence test are summarized in Table B.3. The highlighted cells give the converged parameter values used in final simulations. The chosen converged simulation parameters each contributed approximately 0.01% to the total simulation error when simulating the absolute transmission across the entire bandwidth of 722 µm to 1122 µm. However, as noted when testing the effect of the mesh size in the *xy*-direction, the transmission at the resonant wavelength fluctuated with approximately 6% error. Since this simulation was performed with the other simulation parameters set at values that do not significantly contribute to the simulation error, this 6% error was assumed to be a best estimate of approximate of the error in the simulated transmission. Since the transmission

enhancement G is the ratio of the transmission efficiency of two simulations, the 6% error was used in error propagation to give an 8% error in G.

Table B.1: Converged simulation parameters of the simulated bullseye lens. Highlighted values were chosen for final simulations.

		Z-Pad	XY-Pad	PML Reflec.	ΔZ	ΔXY	Acc.	PML Min.
Mesh Size XY (μm)	Δxy	40	40	40	40	19	39	39
Mesh Size Z (μm)	Δz	40	40	40	4	4	5	7
Mesh Acc.		2	2	2	2	2	2	2
XY-Pad (mm)	–	3	2	2	2	2	2	2
Z-Pad (mm)	–	2	2	2	2	2	2	2
PML Min.	–	64	64	12	12	64	12	12
PML Reflec.	–	1×10^{-4}	1×10^{-4}	1×10^{-10}	1×10^{-10}	1×10^{-30}	1×10^{-10}	1×10^{-10}
Error Contribution		0.01%	0.01%	0.01%	0.01%	0.01%	0.02%	0.01%

Simulations presented for this thesis were performed with a Linux machine with 50 GB of RAM and an Intel Xeon X5680 64-Bit, 3.33 GHz processor with 24 cores. FDTD Solutions splits a single simulation into multiple independent computations across all processor cores, thereby reducing the simulation time. The desired mesh size and the required RAM and simulation time is the primary tradeoff that must be made. For example, the time to perform each simulation when convergence testing the xy-mesh size for a constant Δz of 4 μm is shown in Figure B.10. The simulation time varies as $1/(\Delta xy)^2$ dependence. At a value of $\Delta\, xy =$ 38 μm, the simulation was completed after approximately 40 minutes, increasing to about 1 hour and 30 minutes for the converged value of 19 μm.

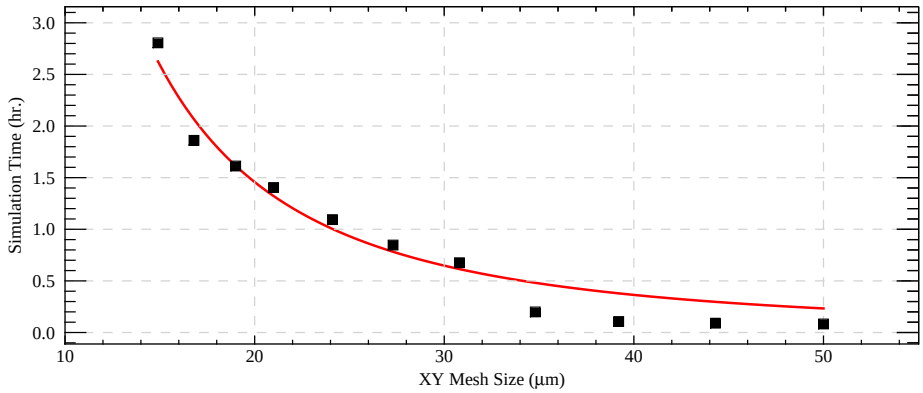

Figure B.10: The time taken to simulate each parameter step in the convergence testing of Δxy (Figure B.9).

The long simulation times needed for small meshes requires that mesh sizes are often chosen to be larger than optimal. Therefore, it difficult to assign a margin of error to the simulated transmission. To address this, the enhancement ratio G, is calculated with identical simulation settings. While the value of G does not give an absolute power measurement,

it is emphasizes the enhancement due to plasmonic effects and can be experimentally measured, as discussed in Chapter 6.

B.4 Table of Simulations

The following table summarizes the settings used in the simulations discussed in Chapter 5. The ridge optimization settings were used to optimizing the initial ridge distance, to simulate the Bragg grating, and to simulate the effect of different Gaussian illuminations. The fabricated double-sided settings were also used in the single-sided simulation with a planar output face.

		Groove Opt.	**Ridge Opt.**	**Phase Tuning**	**Convergence**	**Double-Sided**
Aperture						
Diameter	d	419 µm	150 µm	200 µm	300 µm	300 µm
Thickness	t	1000 µm	200 µm	50 µm	200 µm	50 µm
Input Face						
Type	–	Grooves	Ridge	Planar	Ridges	Ridge
Number of Features	N	6	6	–	6	6
Initial Distance	a	839 µm	1332 µm	Varied	860 µm	1332 µm
Period	p	839 µm	888 µm	–	860 µm	888 µm
Width	w	419 µm	445 µm	Varied	445 µm	445 µm
Depth	s	168 µm	130 µm	100 µm	130 µm	130 µm
Output Face						
Type	–	Mirrored	Planar	Ridge	Planar	Radius Tuned
Tuned Value 1	–	–	–	–	–	1134 µm
Tuned Value 2	–	–	–	–	–	1777 µm
Tuned Value 3	–	–	–	–	–	2367 µm
Tuned Value 4	–	–	–	–	–	2923 µm
Tuned Value 5	–	–	–	–	–	3457 µm
Tuned Value 6	–	–	–	–	–	3976 µm
Bragg Reflector					–	
Type	–	None	Input	None	None	Input
Number of Features	N_r	–	3	–	–	3
Initial Distance	a_r	–	444 µm	–	–	444 µm
Period	p_r	–	444 µm	–	–	444 µm
Width	w_r	–	222 µm	–	–	222 µm
Depth	s_r	–	65 µm	–	–	65 µm
Illumination						
Type	–	TFSF	TFSF	TFSF	Gaussian	Gaussian
Polarization	–	Linear	Linear	Linear	Linear	Linear
Waist Radius	w_0	–	–	–	5000 µm	5100 µm
Focus Location	–	–	–	–	In Focus	In Focus
Wavelength Start	λ_i	722 µm	722 µm	922 µm	722 µm	722 µm
Wavelength End	λ_f	1122 µm	1122 µm	922 µm	1122 µm	1122 µm
# of Wavelengths	n	31	61	1	61	61
Simulation						
Mesh Type	–	Staircase	Staircase	Staircase	Staircase	Staircase
Mesh Size XY	Δxy	10 µm	32 µm	10 µm	19 µm	19 µm
Mesh Size Z	Δz	10 µm	8 µm	10 µm	4 µm	4 µm
Mesh Accuracy		2	2	3	2	2
PML Padding XY	–	0	2	0	2	2
PML Padding Z	–	0	2	0	2	2
PML Min. Layers	–	12	12	12	12	12
PML Reflectivity	–	1×10^{-20}	1×10^{-20}	1×10^{-4}	1×10^{-4}	1×10^{-4}

Appendix C

Fabrication of Bullseye Lenses

Enhanced transmission and beam confinement using bullseye plasmonic lenses at THz frequencies

Tanner J. Heggie[a], David A. Naylor[a], Brad G. Gom[a], Evgueni V. Bordatchev[b]
[a]Department of Physics & Astronomy, University of Lethbridge, Lethbridge, Alberta, Canada;
[b]National Research Council of Canada, Automotive & Surface Transportation, London, Ontario

ABSTRACT

A major limitation in terahertz (THz) imaging applications is the relatively poor diffraction limited spatial resolution. A common approach to achieve subwavelength resolution is near-field imaging using a subwavelength aperture, but the low transmission efficiency through the aperture limits the sensitivity of this method. Bullseye structures, consisting of a single subwavelength circular aperture surrounded by concentric periodic corrugations, have been shown to enhance transmission through subwavelength apertures. At optical wavelengths, the fabrication of bullseye structures has been traditionally achieved by lithographic or chemical processes. Since the scale of plasmonic structures depends on the incident wavelength, precision micromilling techniques are well suited for THz applications. In this paper we describe a diamond micromilling process for the fabrication a plasmonic lenses operating at 325 GHz. Theoretical simulations are obtained using an FDTD solver and the performance of the lens is measured using a customized THz test bed.

Keywords: Plasmonics, bullseye lens, terahertz, micromilling, subwavelength imaging, surface plasmons

1. INTRODUCTION

In recent years, terahertz (THz) radiation has been shown to be a useful differential diagnostic for breast cancer detection around 325 GHz ($\lambda = 922$ μm)[1]. In classical optics, the spatial resolution as expressed by the Rayleigh criterion is on the order of the wavelength of the incident radiation, in this case around a millimeter. For edge detection of cancer cells a resolution of ~ 100 μm is required, which is subwavelength at THz frequencies. Initial attempts at near field imaging at these long wavelengths using subwavelength apertures resulted in poor transmission efficency[2]. For an infinitesimally thin perfect electrical conductor (PEC) in the extreme subwavelength regime $k_0 r \ll 1$, the transmitted power through the hole scales as r^6/λ^4, where $k_0 = 2\pi/\lambda$, r is the radius of the aperture, and λ the wavelength of light[3]. For films of finite thickness and larger apertures the relationship is more complex[4]. In either case, the low transmission efficiency combined with weak THz sources limits the utility of THz subwavelength imaging unless cryogenic detector systems are used.

The discovery of extraordinary transmission (EOT) of light through subwavelength hole arrays by Ebbesen[5] stimulated a dramatic increase in research in the field of plasmonics. The vast majority of this research has occurred at visible wavelengths to enhance the transmission through subwavelength metallic hole arrays, slits, and bullseye lenses[6-9]. The bullseye consists of concentric corrugations on both the input and outputs sides of the lens, at the center of which is a small aperture. The mechanism that leads to EOT has been attributed to the presence of surface plasmon polaritons (SPPs) that are resonantly excited by periodic corrugations on the input side of the surface of the metal[8,10]. Corrugations on the output side serve to couple SPPs back to the radiation field. Phase delays induced by the structure lead to interference effects that can be used to control the propagation direction of the output beam[6-9]. Plasmonic devices have also been designed for long wavelength radiation, where metals begin to behave as perfect electrical conductors (PECs) and the structural parameters scale with the wavelength[1,11-13]. In this paper, we present the design, fabrication, and initial performance of a plasmonic lens operating at a frequency of 325 GHz.

1.1 Terahertz plasmonics

Surface plasmon polaritons are solutions to Maxwell's equations solved at the interface of metal and a dielectric, occurring when incident electromagnetic waves couple to the oscillation of free charge carriers near the surface of a conductor[10]. The excited electromagnetic surface wave propagates along the interface and decays evanescently into both media. The characteristic length scales of SPPs are derived from the components of the SPP wave vector, namely the propagation constant

$$k_x = k_x' + ik_x'' = k_0\sqrt{\frac{\varepsilon_d\varepsilon_m}{\varepsilon_d + \varepsilon_m}}, \tag{1}$$

where k_0 is the free space wave vector, ε_d is the permittivity of the dielectric, and $\varepsilon_m = \varepsilon_m{}' + i\varepsilon_m''$ is the complex permittivity of the metal, defines the propagation length L of SPPs along the interface. This distance, where intensity of the wave drops to $1/\mathrm{e}$ its maximum value, is given by

$$L = \frac{1}{2k_x''}. \tag{2}$$

The z-component of the wave vector into the metal k_{zm} is

$$k_{zm} = k_{zm}' + ik_{zm}'' = \sqrt{\varepsilon_m\frac{\omega^2}{c^2} - k_x^2} \tag{3}$$

and defines the skin depth of the surface wave as the point where the field amplitude decreases to a factor of $1/\mathrm{e}$,

$$\delta_m = \frac{1}{k_{zm}''}. \tag{4}$$

A matching equation for the SPP skin depth in the dielectric δ_d is found by replacing ε_m with ε_d in Equation 3 and k_{zm} with k_{zd}. By way of illustration, for noble metals at visible wavelengths, SPPs are characterized by strong confinement of their electromagnetic field near the interface. Using permittivity data for Au given by Johnson and Christy[14] fit using Lumerical's[15] multi-coefficient model, the permittivity of Au at $\lambda = 632.8$ nm is $\varepsilon_m = -11.7 + 1.2i$. At this wavelength, the SPP penetrates $\delta_m \approx 30$ nm ($\sim 10^{-2}\,\lambda$) and $\delta_d \approx 300$ nm ($\sim 0.5\lambda$) into the metal and dielectric, respectively, and has a decay length of $L \approx 10$ μm ($\sim 16\lambda$).

The principle difference at THz wavelengths lies in the fact that the properties of metals differ significantly at these low frequencies. The complex permittivity of metals is orders of magnitude greater at THz wavelengths than in the visible, tending to that of a PEC. The Drude model has been shown to be a good fit to the experimental THz response of free charge carriers to an applied electric field in terms of the plasma frequency, $\omega_p = \sqrt{(n_e e^2/m^*\varepsilon_0)}$, where n_e is the free electron density, e is the elementary charge, m^* is the effective electron mass, and ε_0 is the free space permittivity, and the electron damping frequency ω_τ[16]:

$$\varepsilon_m = \varepsilon_{m,r} + i\varepsilon_{m,i} = \varepsilon_\infty - \frac{\omega_p^2}{\omega^2 + i\,\omega\omega_\tau}. \tag{4}$$

Using the values $\varepsilon_\infty = 1$, $\omega_p/2\pi = 2.17 \times 10^3$ THz, and $\omega_\tau/2\pi = 6.48$ THz from Ordal[16], the Drude permittivity of Au at $\lambda = 922$ μm is calculated to be: $\varepsilon_m = -1.12 \times 10^5 + 2.24 \times 10^6 i$. The resulting SPP is characterized by weak confinement to the surface with relatively small extent into the metal $\delta_m \approx 135$ nm ($\sim 10^{-4}\,\lambda$), larger extent into the dielectric $\delta_d \approx 30$ cm ($\sim 10^2\,\lambda$), and a long propagation length $L \approx 330$ m ($\sim 10^5\,\lambda$).

Since only the material properties within approximately one skin depth contribute to the operation of a plasmonic device, the above numbers show that at THz frequencies such devices can be made thin compared to the wavelength. While THz bullseye devices have been made using nano-techniques, this requires access to a nano-fabrication facility. In addition, the metallic deposition depths required are large compared to typical applications at optical wavelengths. Since the required precision of a THz plasmonic lens scales with wavelength and is thus relatively low when compared to an optical equivalent, it should be possible to achieve the same relative accuracy at THz wavelengths using a micro-machining approach.

2. BULLSEYE PLASMONIC LENS

2.1 Lens design

Bullseye plasmonic lens designs for both visible and THz applications typically have surface structures that are either grooves (indentations) or ridges (protrusions) along the input and/or output faces of the lens[11,12]. Thin, asymmetric designs have also been fabricated[13]. Our design uses annular ridge structures with a rectangular cross-section centered on

a thin 50 μm central aperture of 300 μm diameter. The ridge structure allows the thickness of the aperture to be dictated by the machining capabilities, whereas for a groove structure the depth of the corrugations limits the minimum thickness. Since transmission through a subwavelength aperture is attenuated with increasing thickness, the substrate thickness must be minimized[7].

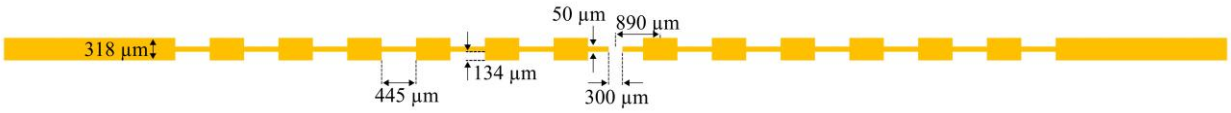

Figure 1. Cross-section of the bullseye plasmonic lens (not to scale).

A cross-sectional view of our lens design is shown in Figure 1. The geometrical parameters of the ridges were chosen to maximize the coupling of the incident radiation into SPPs via appropriate input corrugations. Parameters were selected during simulation to maximize the enhanced transmission at $\lambda = 922$ μm for plane wave illumination. The central aperture is surrounded by 6 concentric grooves with a periodicity of 890 μm, width of 445 μm, and depth of 134 μm. The full diameter of the lens is 25 mm. An integral outer support ring was fabricated for structural integrity during machining and is used to mount the lens.

The beam exiting the aperture is diffracted in all directions with a range of near-field wave vectors. Wave vectors that match Au-Air SPPs couple to the interface and propagate radially outward, scattering from the surface corrugations. By varying the geometrical parameters of the ridge, a phenomenological phase modulation model can be developed that describes the relative phase difference between photons travelling through the central aperture and those scattered from the ridge wall[9]. In principle, the output groove structure can be tuned by varying the groove spacing, width, and/or depth to modify the focal length of the lens. For simplicity, in our initial design we adopted the same output pattern as the input side of the device. The theoretical response of this lens is shown in the next section.

2.2 Simulated response

Since analytical solutions to Maxwell's equations do not exist for complicated interfaces, Lumerical FDTD Solutions, a commercial-grade simulator based on the finite-difference time-domain method, was used to find solutions to these equations[15].

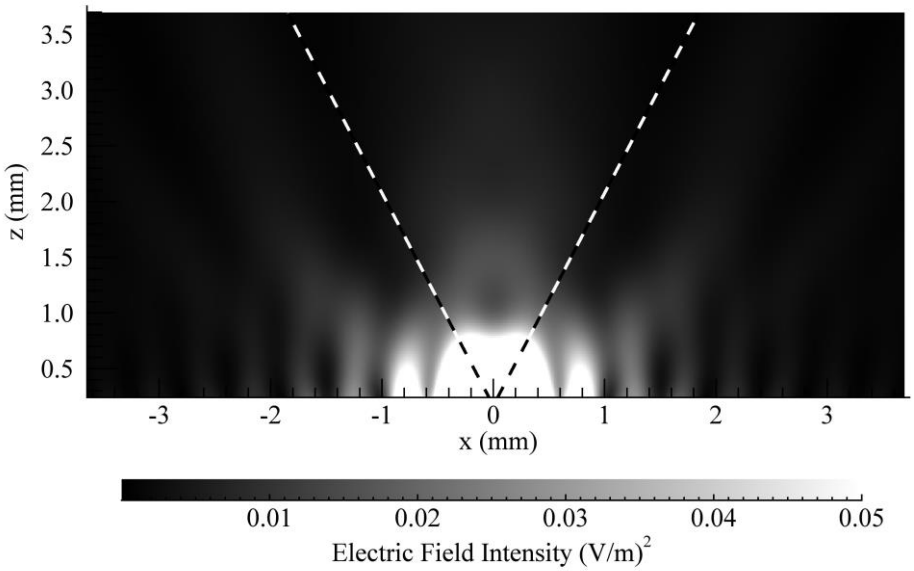

Figure 2. Simulated beam profile of the bullseye lens. Dashed white lines indicate the acceptance angle of the focusing optics (Section 4).

The simulated beam profile of the fabricated plasmonic lens (Section 3) illuminated by a circularly polarized Gaussian beam with a waist radius of 0.56 mm is shown in Figure 2. Since the lens has axial symmetry, the use of circularly polarized light leads to an axially symmetric spot[9]. The beam is shaped by the output corrugations.

3. FABRICATION OF PLASMONIC LENS

Fabrication of the bullseye plasmonic lens was performed on a modular multi-functional Kugler Microgantry nano5X micromachining system. This system integrates several micromachining technologies along with measurement instrumentation. The Microgantry nano5X and its components are shown in Figure 3.

Three micromachining technologies are used: fly cutting with a 2,000 rpm spindle, micromilling with an 180,000 rpm spindle, and micromachining with a picosecond laser. A Renishaw touch probe with a measurement accuracy of ±500 nm is used for measuring workpiece geometry before and after machining and during alignment. The system is also equipped with a Blum laser tool setting sensor for measuring cutting tool geometry (e.g. diameter and overhang length) having a measurement repeatability (2σ) of 100 nm. Motion stages in this system are composed of air bearings with a position measuring resolution of 10 nm and a positioning accuracy within ±250 nm in XY-direction and ±500 nm in Z-direction. Straightness is within ±800 nm per 100 mm travel for all linear axes. The system is also equipped with an automatic tool changer able to accommodate up to 60 cutting tools.

In general, micromachining technologies, such as fly cutting, micromilling, and laser micromachining bring significant benefits to the fabrication of micro/nano-scale optical parts, structures and geometries. These benefits range from fabricating functional part prototypes and tooling (e.g. inserts, molds, dies, stamps, electrodes, etc.) with optical surface quality (Ra < 10 nm), high aspect ratio components (e.g. 1:280 between wall width and height[17]), and advanced micromachining processes (e.g. picosecond laser polishing[18]).

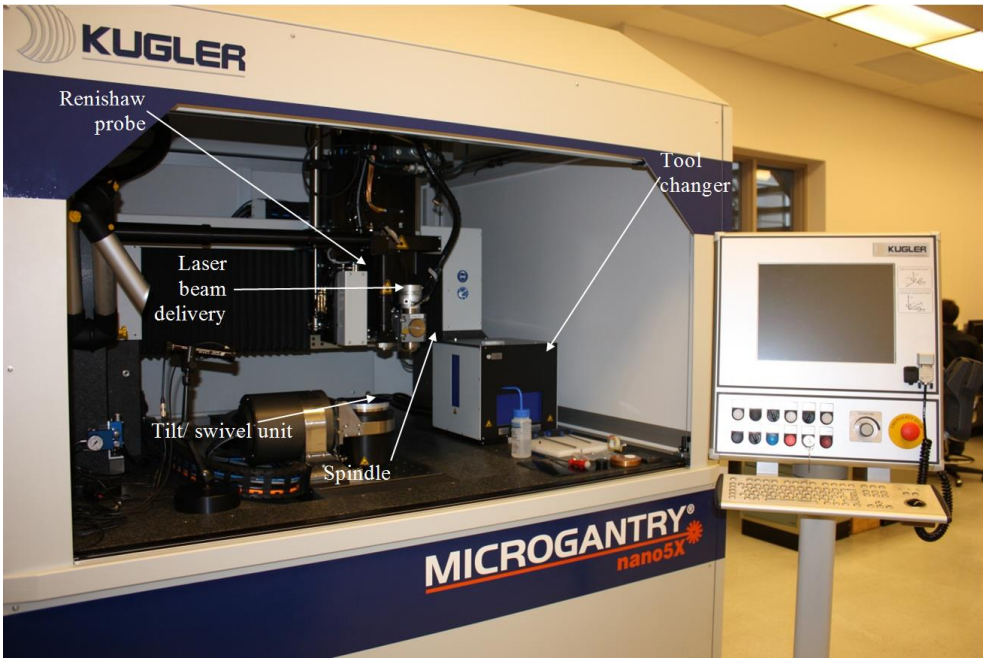

Figure 3. The modular, multi-functional micromaching system Microgantry nano5X and its components.

The design of the plasmonic lens is presented in Figure 1. The device poses three main challenges for fabrication. Firstly, accuracy on all dimensions of ±10 μm. Secondly, precise axial alignment between inner and outer faces is required. The

third and most challenging aspect was to keep the thickness at the center of the lens as thin as possible to enhanced throughput while maintaining structural integrity[4].

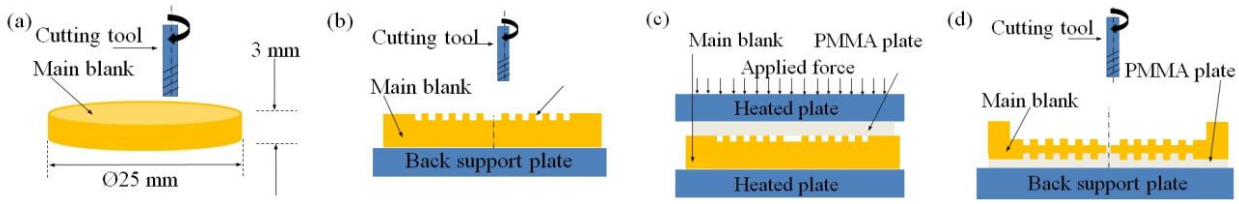

Figure 4. Steps in fabricating the bullseye plasmonic lens (not to scale). (a) Fabrication of a main blank; (b) fabrication of an outer lens; (c) fabrication of a support structure; (d) fabrication of an inner lens.

The process flow diagram for the fabrication of the plasmonic lens is shown in Figure 4. The first step involved fabricating a copper main blank of diameter 25 mm and thickness 3 mm. The main challenge here was to achieve a plane, parallel device. This step was performed through micromilling using a diamond flat cutter with a diameter of 2 mm, rotational speed of 30,000 rpm, and a feed rate of 240 mm/min, which achieved a thickness deviation better than ±5 µm. Greater precision is possible with the micromill, but was not required. The flatness achieved allowed the center of the blank to be determined precisely and ensured axial alignment in all further micromachining operations.

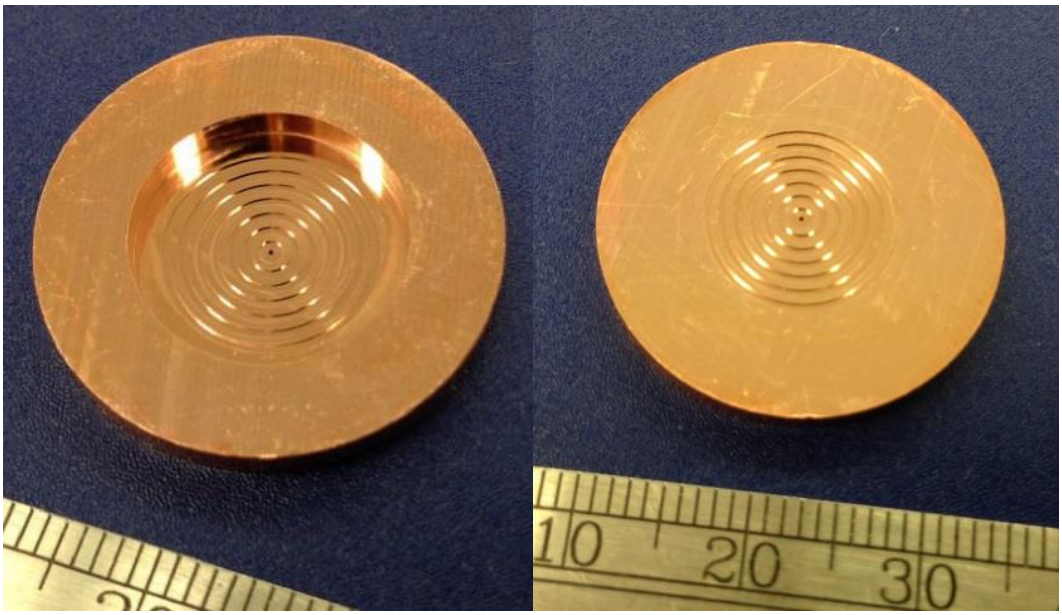

Figure 5. Photographs of the inner (a) and outer (b) faces of the fabricated bullseye plasmonic lens.

In the next step, shown in Figure 4b, the main blank was fixed and circular channels with a rectangular cross-section were micromilled with a flat end diamond cutter having a diameter of 300 µm. Micromilling was performed with a rotational speed of 30 000 rpm and a feed rate of 120 mm/min removing 20 µm depth for each cutting path within a channel. Before the input surface of the lens could be machined, the output surface was filled with PMMA acrylic, fabricated using a hot embossing process, to provide structural integrity. A Chrystal Digital Load Cell E-Z Press equipped with temperature controlled heated platens and a controlled applied force was used in this embossing process, as shown in Figure 4c. During this step, a 1 mm thick PMMA plate was placed between a one-side fabricated plasmonic lens (used as a die) and platens that were heated above PMMA glass transition temperature (e.g. 107°C). The back

supporting plate was made under 300 N force applied for a period of 10 minutes to ensure an accurate match with lens geometry. In the final step, the inner lens was micromilled as it shown in Figure 4d using the same cutting parameters and machining strategy as during micromilling of outer lens. The plasmonic lens prototype is shown in Figure 5. The accuracy of geometrical features of the output surface is shown in Figure 6. Metrology measurements were obtained using Veeco WYKO NT1100 Optical Profilometer with a resolution of 0.1 nm.

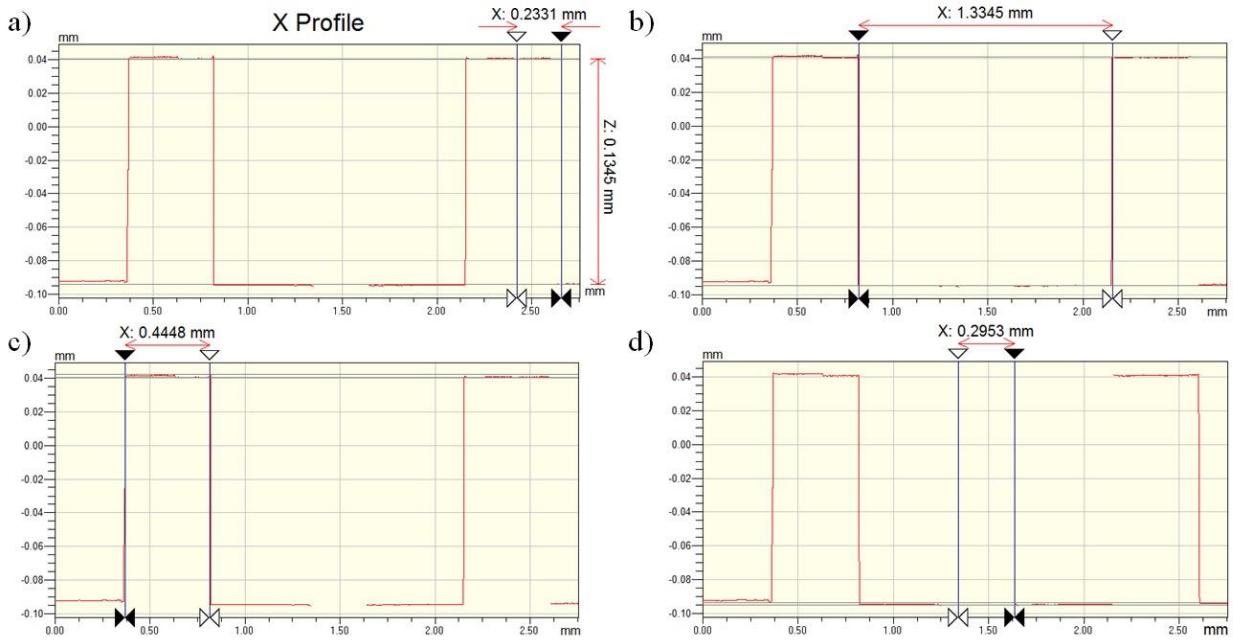

Figure 6. Examples of achieved accuracy of geometric features on the output lens face: (a) channel depth, (b) diameter of the first circular cavity, (c) width of the first circular wall, and (d) diameter of the central hole.

Circular channels were fabricated with an measured depth of 134.5 µm versus a design depth of 134.0 µm (see Figure 6a), a variance of 0.5 µm; the measured diameter of first circular cavity was 13 345 µm versus a design diameter of 13 350 µm (see Figure 6b); the measured width of the wall separating inner cavity and first circular channel was measured as 444.8 µm versus a design width of 445.0 µm (see Figure 6c) corresponding to a variance of ±1 µm. Finally, the diameter of the central hole was measured to be 295.3 µm versus a design diameter of 300.0 µm (see Figure 6d).

The final geometric feature in the lens design was the residual metal thickness at the center of the lens. The design thickness was 50 µm, however in this prototype fabrication we took a conservative approach to prevent potential damage. As a result, the estimated thickness was determined to be 66 µm. After milling, a 1 µm thick Au coating (~$10\delta_m$), was electroplated on the copper surface to prevent oxidation. These results show that micromaching techniques are capable of fabricating THz plasmonic devices to the required accuracy.

4. EXPERIMENTAL PROCEDURE

To measure the performance of the plasmonic lens at THz wavelengths, a test bed was setup as shown in Figure 7. The THz signal is produced by a Virginia Diodes, Inc. (VDI) line source transmitter with an operating range of 320-330 GHz[19]. The operating frequency was set to 325 GHz and has a maximum-power output of ~10 mW. The THz source makes use of a split-block diagonal horn that emits a Gauss-Hermite beam with approximately 84.3% of its power in the fundamental Gaussian mode[20]. The Gaussian beam at this frequency has a waist radius of 1.68 mm located 6.04 mm inside of the horn.

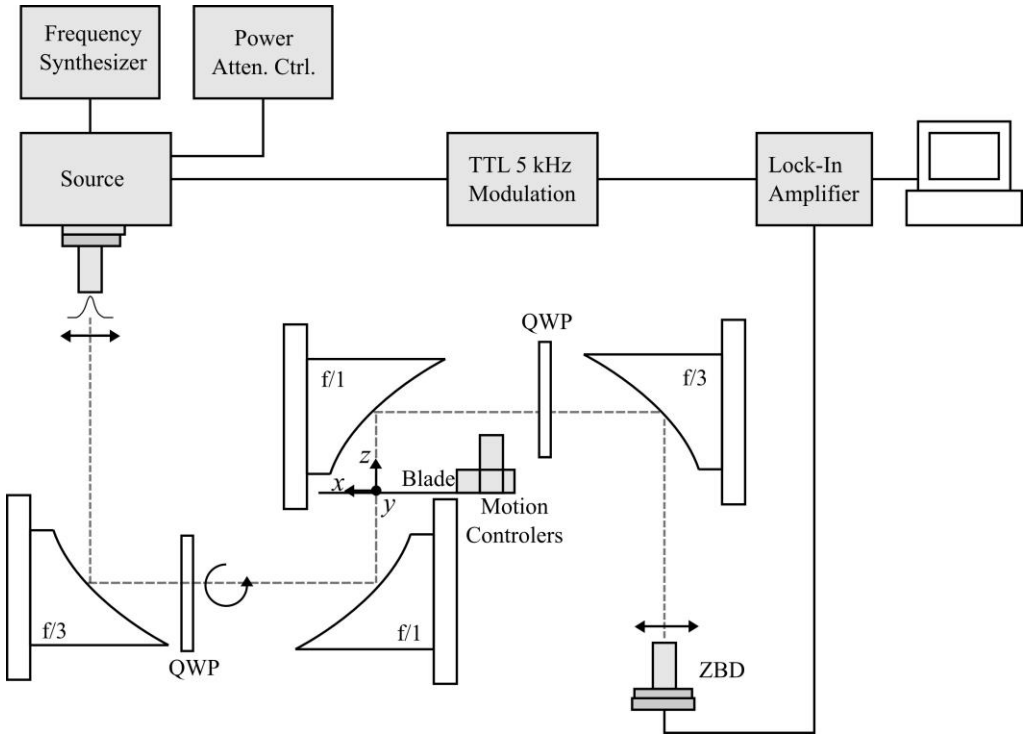

Figure 7. Schematic diagram of the THz knife-edge measurement system. A predominantly Gaussian THz beam is produced by a line source that is optically isolated using a QWP. The beam is collected by the input optics (f/3 and f/1 90° OAP mirrors) and produces a focus with a waist of $w_0 = 0.57$ mm at the location of the knife. The output optics (f/1 and f/3 90° OPA mirrors) carry the beam through an identical QWP and polarizer arrangement before detection by the ZBD.

A quartz quarter-wave plate (QWP) was placed in the collimated beam creating a circularly polarized beam to optically isolate the source from unwanted reflections. Four 50.8 mm diameter aluminum 90° off-axis parabolic (OAP) mirrors were configured in a telescope arrangement to provide an intermediate image. The OAPs were orientated such that rays from a single field point strike identical coordinates on each parabolic mirror (i.e. in a "tip-to-tip" fashion) to avoid a tilted image plane. The beam passes through a second QWP to restore linear polarization and power is measured by a VDI zero bias detector with a diagonal horn identical to that of the source[19]. Standard lock-in techniques were applied using a lock-in amplifier to extract the THz signal referenced against the 5 kHz modulation frequency.

The spatial profile of the THz beam was characterized by knife-edge measurements using a three-axis piezo CONEX-AGP Agilis-P Controller with Encoder Feedback placed near the focus. The three-axis stage allows the knife to be moved with a minimum incremental motion of 0.2 μm. The blade was translated vertically (y) and successively blocked the beam. A control and data-acquisition program was written that recorded the output DC voltage as a function of position of the knife was moved across the aperture. In theory, the signal measured as a function of the knife-edge position takes the form of a typical S-curve error function[21],

$$P = \frac{P_T}{2}\left(1 - \mathrm{erf}\left(\frac{\sqrt{2}(y - y_0)}{\omega_0}\right)\right), \tag{4}$$

which corresponds to the integrated beam intensity profile of the Gaussian beam. Error functions were fitted to the S-curves with a fixed total power P_T to obtain the Gaussian beam waist ω_0 and the optical axis y_0.

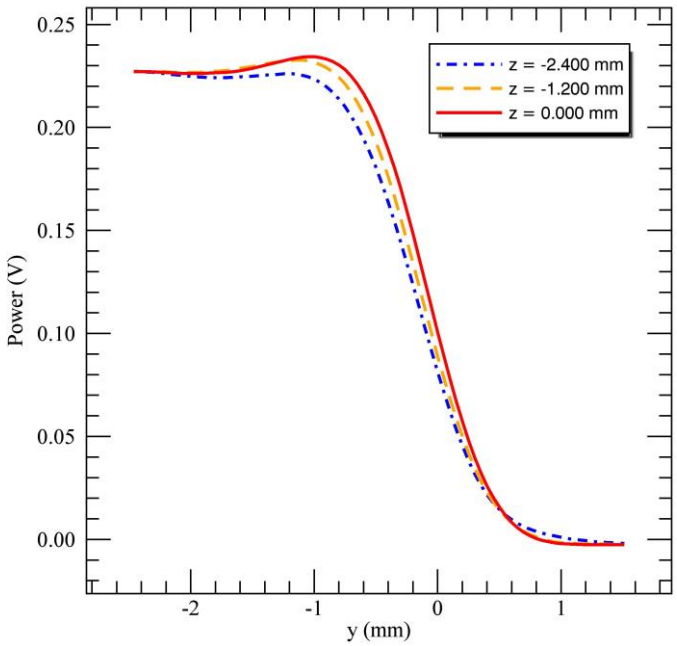

Figure 8. Knife-edge measurements as a function of knife position (y) for cuts along the axis of propagation (z) leading to the focus at z = 0 mm.

An example of measured S-curves in the absence of a plasmonic lens is shown in Figure 8. Beam profiles were measured along the axis of transmission (z). The focus was defined by the position of minimum fitted beam waist and maximum beam intensity, as plotted in Figure 9, and a minimum fitted beam waist of w_0= 0.77 mm was compared to that found using the 90%-10% criterion, w_0= 0.74 mm, and the 80%-20% criterion, w_0= 0.72 mm. The measured and fitted S-curve and intensity profile at the location of the focal point can be found in Figure 10.

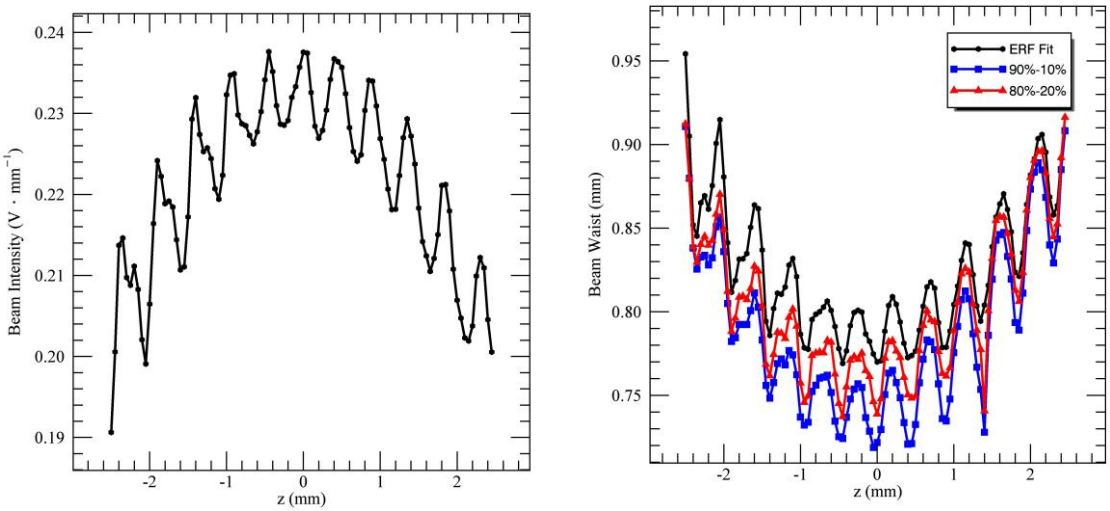

Figure 9. Maximum Gaussian beam intensity (left) and beam waist radius (right) from corresponding error function fits (black, dotted) along the propagation axis (z). The waist radius was also calculated using a 90%-10% (blue, squares) and 80%-20% (red, triangles) analysis. The oscillations seen are due to resonant cavities formed by the QWPs in the optical system. We are in the process of antireflection coating the QWP to minimize these effects.

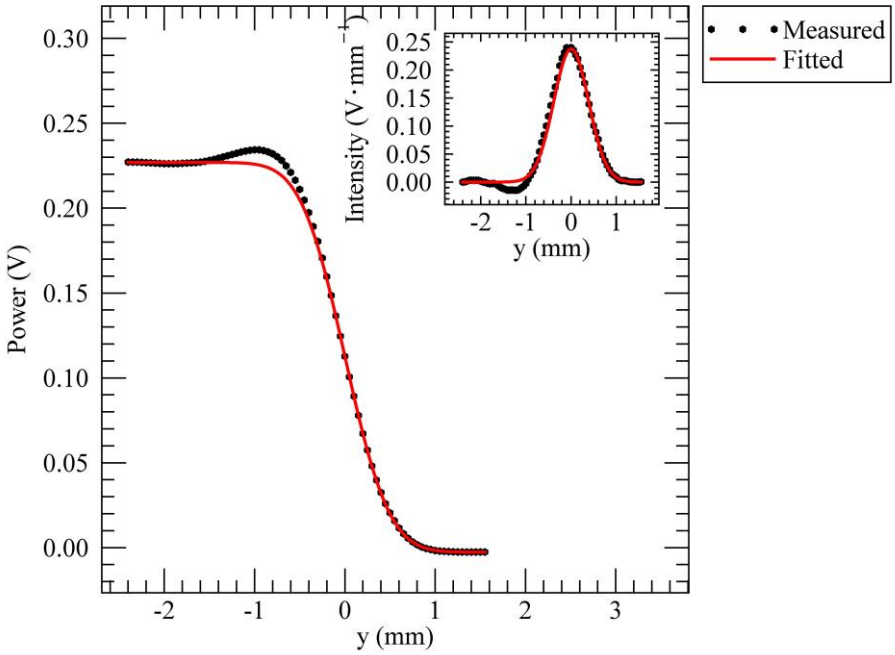

Figure 10. Measured (black, dotted) S-curve with an error function fit (red, solid) at the focus of the Gaussian beam. Inset: the corresponding Gaussian beam profile overlaid with the derivative of the error function fit.

5. RESULTS AND DISCUSSION

The performance of the plasmonic lens was measured by placing the midpoint of the lens aperture at the location of the focus (z = 0 mm), as determined by the above procedure. The knife-edge was brought to 50 μm in front of the output face and translated vertically across the transmitted beam at various distances along the optical axis. Beam intensity functions were fit to a Gaussian distribution, and the resulting FWHM was plotted as a function of translated distance. Similar measurements were made for a single aperture with a diameter of 300 μm and thickness of 50 μm, illuminated by linearly polarized light and are compared with the plasmonic lens in Figure 10. Although the results are preliminary they clearly show that the transmitted beam from the plasmonic lens remains close to the design width of 300 μm out to a distance of ~600 μm. By comparison, the beam from the single aperture of the same diameter is more than twice as large.

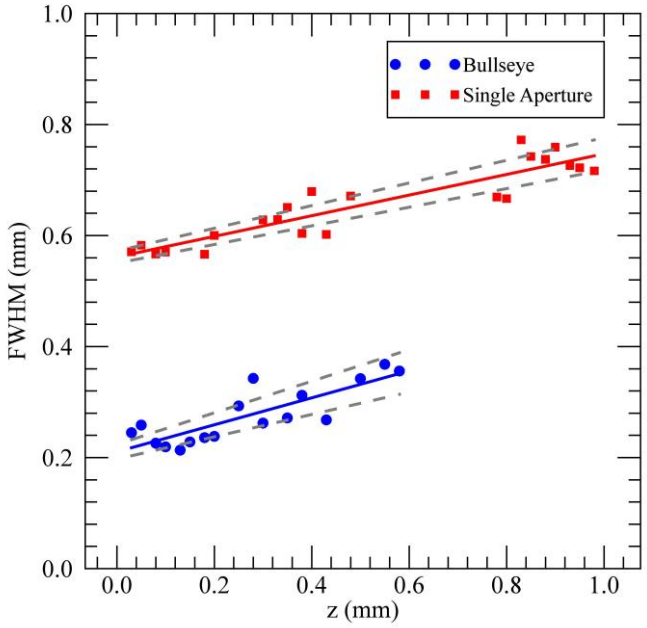

Figure 11. Fitted FWHM of the measured beam transmitted through the bullseye lens and through a comparable single aperture (d = 300 μm, t = 50 μm).

6. CONCLUSIONS

In this paper, we describe a method to fabricate a plasmonic lens optimized for THz wavelengths using precise micromachining techniques. Our fabrication technique allows for precision geometrical features at the level of ±1 μm (~10^{-3} λ). A THz test bed has been developed that produces the well-defined and stable beam necessary to characterize the performance of plasmonic lenses. Preliminary measurements of the fabricated bullseye structure show evidence of subwavelength beaming compared to a single aperture. Measurements of the increased transmission expected from the plasmonic lens have been hampered by the uncertainties of the residual thickness at the center of the plasmonic lens. We are currently exploring ways to optimize the design of the lens by precise tuning of the surface structures, to focus THz radiation several wavelengths from the output surface. Adjusting the geometrical parameters of the output face (by tuning the ring spacing, width and depth) confers tunable focusing. Parameters can be chosen to produce a more robust lens with a thinner central aperture.

ACKNOWLEDGEMENTS

The authors acknowledge support from CMC, NRC and NSERC.

REFERENCES

[1] Chiu, C., Chen, H., Huang, Y., Hwang, Y., Lee, W., Huang H. and Sun C., "All-terahertz fiber-scanning near-field microscopy," Opt. Lett. 34(7), 1084-1086 (2009).
[2] Hunsche, S., Koch, M., Brener, I. and Nuss, M. C., "THz near-field imaging," Opt. Comm. 150, 22-26 (1998).
[3] Bethe, H. A., "Theory of Diffraction by Small Holes," Phys. Rev. 66, 163-182 (1944).
[4] Roberts, A., "Electromagnetic theory of diffraction by a circular aperture in a thick, perfectly conducting screen," J. Opt. Soc. Am. A 4(10), 1970-1983 (1987).

[5] Ebbesen, T. W., Lezec, H. J., Ghaemi, H. F., Thio, T. and Wolff, P. A., "Extraordinary optical transmission through subwavelength hole arrays," Nature 391, 667-669 (1998).
[6] Lezec, H. J., Degiron, A., Devaux, E., Linke, R. A., Martin-Moreno, L., Garcia-Vidal, F. J. and Ebbesen, T.W., "Beaming light from a subwavelength aperture," Science 297, 820-822 (2002).
[7] Martin-Moreno, L., Garcia-Vidal, F. J., Lezec, H. J., Degiron, A. and Ebbesen, T. W., "Theory of highly directional emission from a single subwavelength aperture surrounded by surface corrugations, " Phys. Rev. Lett. 90(16), 167401 (2003).
[8] Degiron, A. and Ebbesen, T. W., "Analysis of the transmission process through single apertures surrounded by periodic corrugations," Opt. Soc. Am. 12(16), 3694-3700 (2004).
[9] Hao, F., Wang, R. and Wang, J., "A design method for a micron-focusing plasmonic lens based on phase modulation," Plasmonics 5(4), 405-409 (2010).
[10] Raether, H., [Surface plasmons on smooth and rough surfaces and on gratings], Springer Tracts in Modern Physics 11, (1998).
[11] Ishihara, K., Hatakoshi, G., Ikari, T., Minamide, H., Ito, H. and Ohashi, K., "Terahertz wave enhanced transmission through a single subwavelength aperture with periodic surface structures," Jpn. J. Appl. Phys. 44, 1005-1007 (2005).
[12] Gallant, A. J., Levitt, J. A., Kaliteevski, M., Wood, D., Petty, M. C., Abram, R. A., Brand, S. and Chamberlain, J. M., "Enhanced THz transmission apertures through sub-wavelength annular apertures," Proc. SPIE 6323, 632316 (2010).
[13] Baragwanath, A. J., Freeman, J. R., Gallant, A. J., Zeitler, J. A., Beere, E. H., Ritchie, D. A. and Chamberlain, J. M., "Terahertz near-field imaging using subwavelength plasmonic apertures and a quantum cascade laser source," Opt. Lett. 36(13), 2393-2395 (2011).
[14] Johnson, P. B. and Christy, R. W., "Optical constants of the noble metals," Phys. Rev. B 6(12), 4370-4379 (1972).
[15] FDTD Solutions (8.6.2), Lumerical Solutions, Inc. http://www.lumerical.com/tcad-products/fdtd/.
[16] Ordal, M. A., Long, L. L., Bell, R. J., Bell, S. E., Bell, R. R., Alexander, R. W. and Ward, C. A., "Optical properties of the metals Al, Co, Cu, Au, Fe, Pb, Ni, Pd, Pt, Ag, Ti, and W in the infrared and far infrared," Appl. Opt. 22(7), 1099-1120 (1983).
[17] Bordatchev, E. V., Tauhiduzzaman, M., Kugler, T., Katz, A. and Bohr, R., "Demonstration of advanced capabilities of 5-axis micromilling: geometries with high-aspect ratio and/or optical surface quality," Proc. of the 8th ICOMM, 357-362 (2013).
[18] Hafiz, A, M. K., Bordatchev, E. V. and Tutunea-Fatan, R. O., "Experimental analysis of applicability of a picosecond laser for micro-polishing of micromilled Inconel 718 superalloy," Int. J. Adv. Manuf. Technol., 1-16 (2013).
[19] Virginia Diodes, Inc. http://vadiodes.com/.
[20] Johansson, J. F. and Whyborn, N. D., "The diagonal horn as a sub-millimeter wave antenna," IEEE Trans. Microw. Theory Techn. 40(5), 63-81 (1992).
[21] Dobroiu, A., Yamashita, M., Ohshima, Y. N., Morita, Y., Otani, C. and Kawase, K., "Terahertz imaging system based on a backward-wave oscillator," Appl. Opt. 43(30), 5637-5646 (2004).

Fabricated Plasmonic Lens (design #1): Overall view

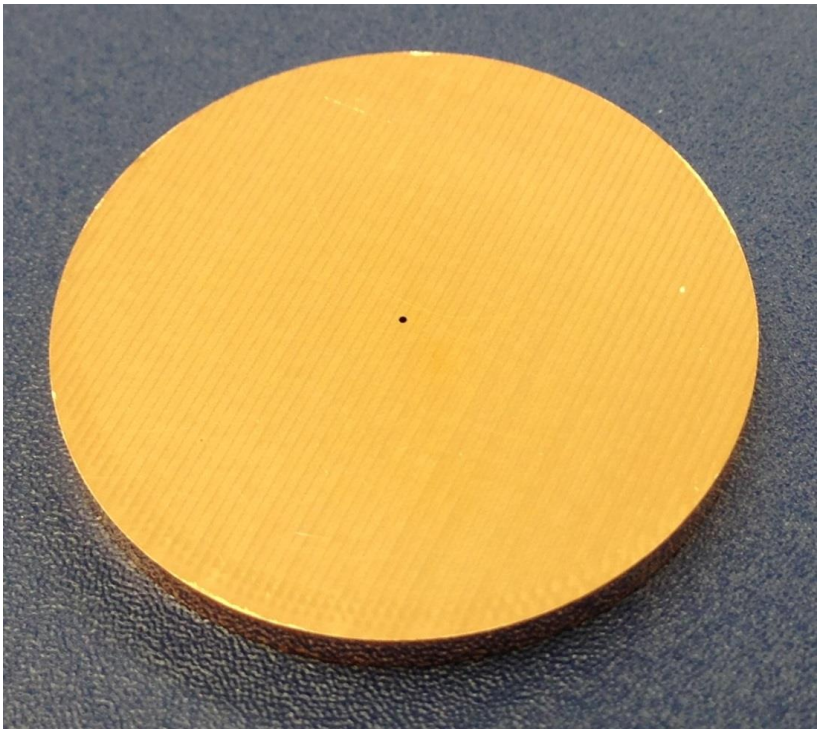

front side

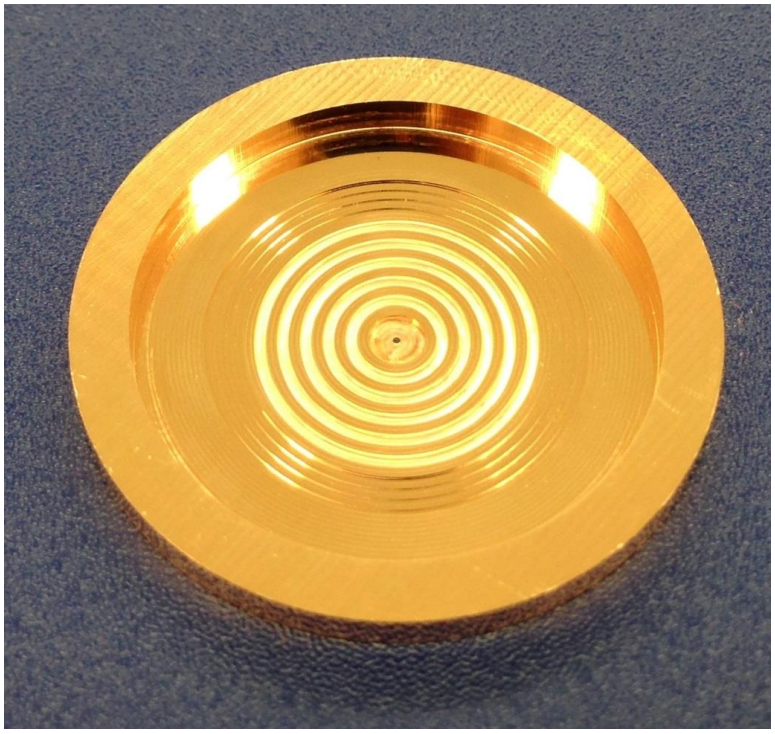

back side

Fabricated Plasmonic Lens (design #1): Critical dimensions

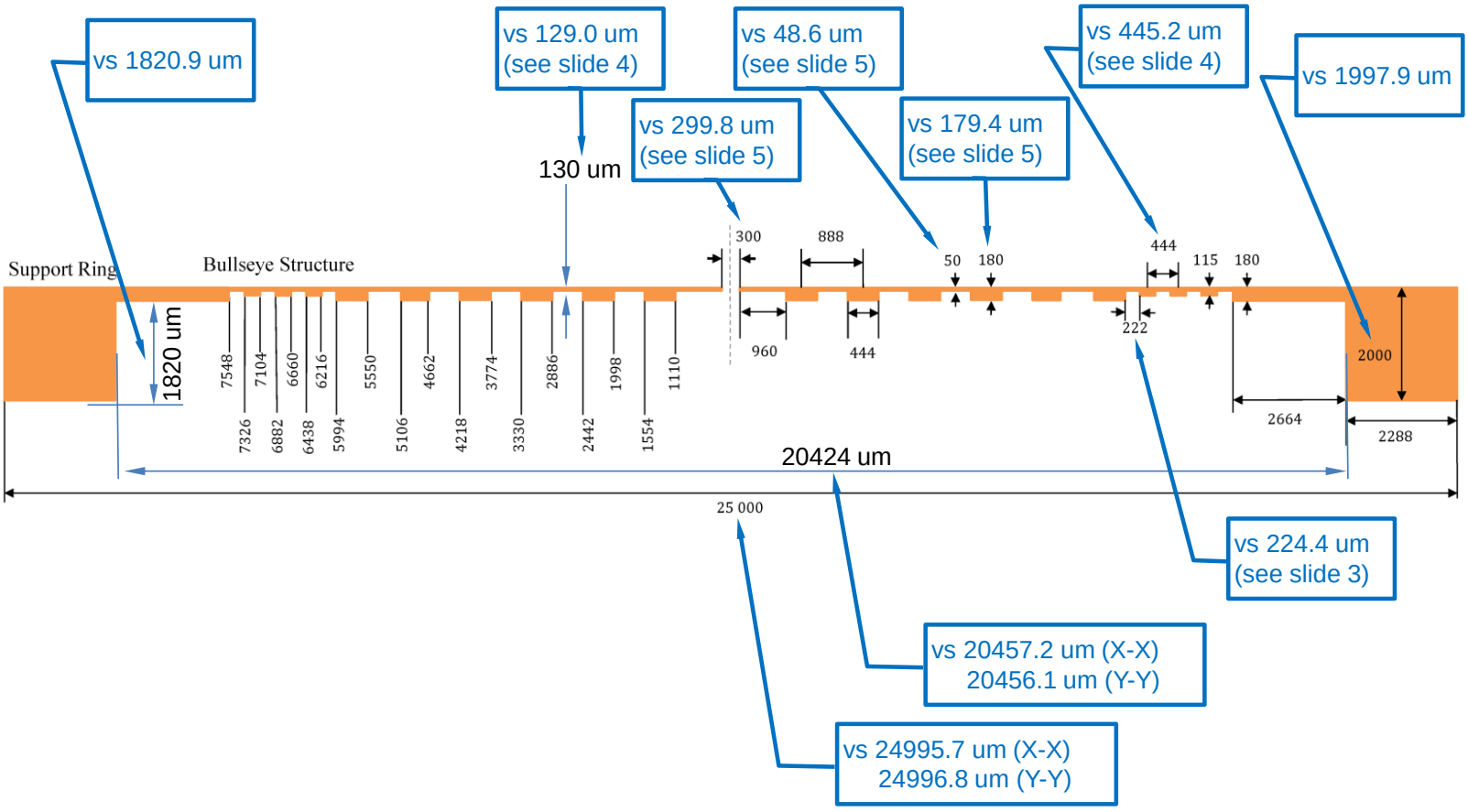

Fabricated Plasmonic Lens (design #1): Some critical dimensions – 222 um rings

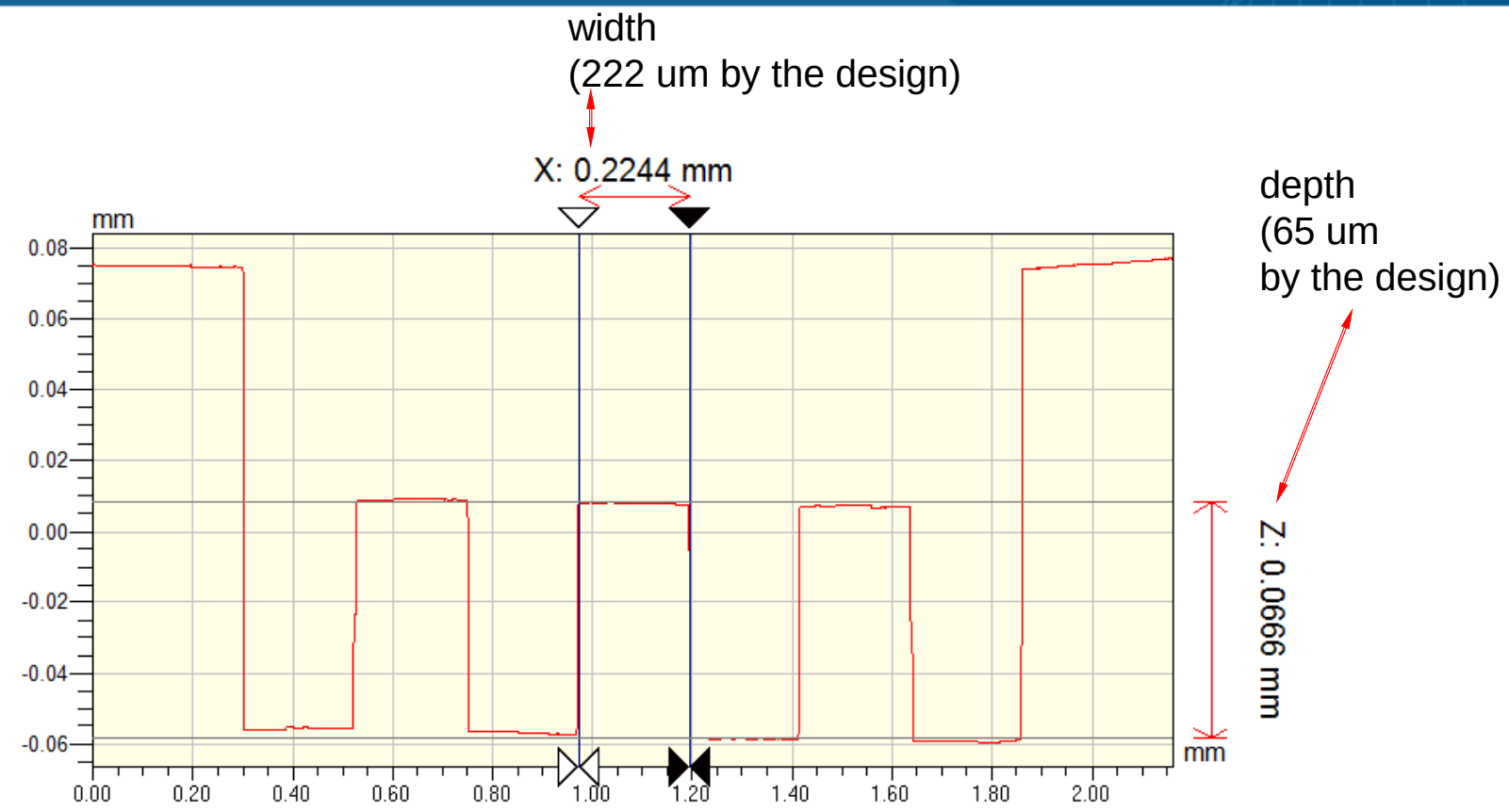

Fabricated Plasmonic Lens (design #1): Some critical dimensions – 444 um rings

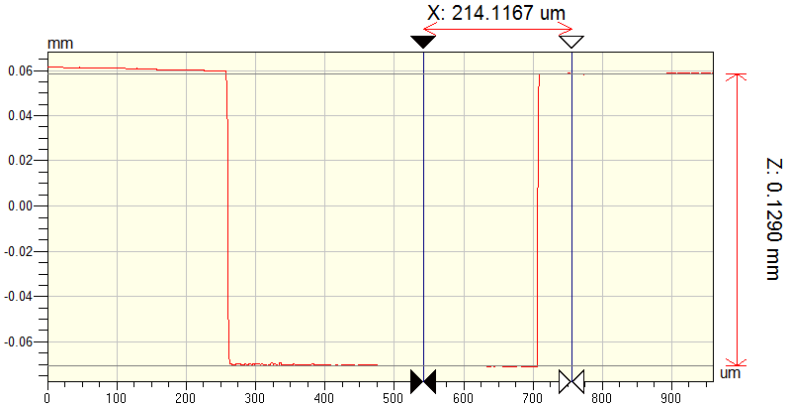

depth
(130 um by the design)

width
(444.0 um by the design)

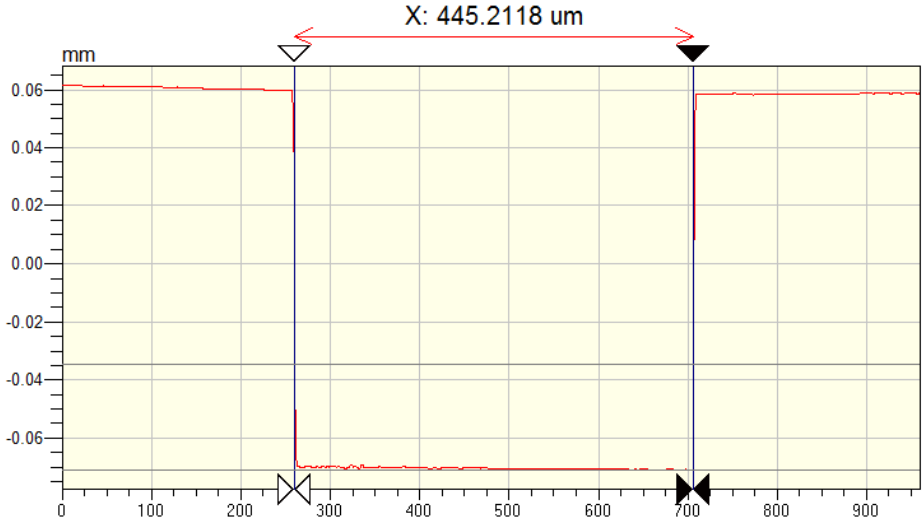

Fabricated Plasmonic Lens (design #1): Some critical dimensions – central hole

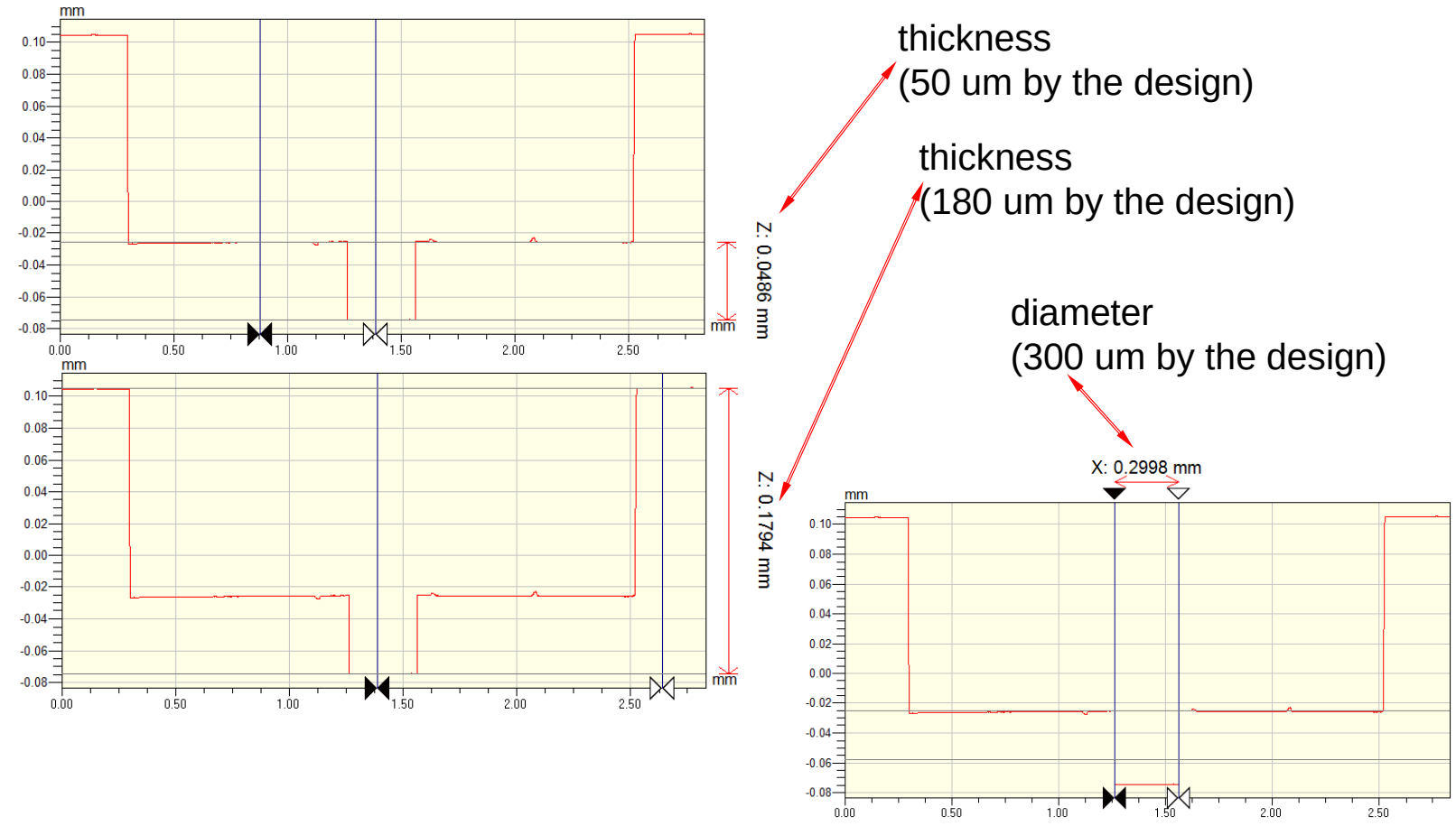

Bibliography

[1] M. A. Ordal, L. L. Long, R. J. Bell, S. E. Bell, R. R. Bell, R. W. Alexander, and C. A. Ward, "Optical properties of the metals Al, Co, Cu, Au, Fe, Pb, Ni, Pd, Pt, Ag, Ti, and W in the infrared and far infrared," *Appl. Opt.*, vol. 22, no. 7, pp. 1099–1120, 1983.

[2] Sakurambo, "Airy Pattern." `http://commons.wikimedia.org/wiki/File:Airy-pattern.svg`, Oct. 2014.

[3] H. J. Lezec, A. Degiron, E. Devaux, R. A. Linke, L. Martin-Moreno, F. J. Garcia-Vidal, and T. W. Ebbesen, "Beaming light from a subwavelength aperture," *Science*, vol. 297, pp. 820–822, Jun. 2002.

[4] S. Aurantiaca, "A FabryPérot Etalon. Light Enters the Etalon and Undergoes Multiple Internal Reflections." `http://en.wikipedia.org/wiki/File:Etalon-2.svg`, Apr. 2014.

[5] DrBob, "Etalon Transmission Plot." `http://en.wikipedia.org/wiki/File:Etalon-2.png`, Nov. 2014.

[6] E. Hecht, *Optics*. Addison-Wesley, 4th ed., 2001.

[7] A. J. Gallant, J. A. Levitt, M. Kaliteevski, D. Wood, M. C. Petty, R. A. Abram, S. Brand, and J. M. Chamberlain, "Enhanced THz transmission apertures through sub-wavelength annular apertures," *Proc. SPIE*, vol. 6323, p. 632316, 2006.

[8] X.-C. Zhang, "Terahertz wave imaging: horizons and hurdles," *Phys. Med. Biol.*, vol. 47, no. 21, p. 3667, 2002.

[9] E. Pickwell and V. P. Wallace, "Biomedical applications of terahertz technology," *J. Phys. D*, vol. 39, no. 17, p. R301, 2006.

[10] J. F. Federici, B. Schulkin, F. Huang, D. Gary, R. Barat, F. Oliveira, and D. Zimdars, "THz imaging and sensing for security applications explosives, weapons and drugs," *Semicond. Sci. Technol.*, vol. 20, no. 7, p. S266, 2005.

[11] D. J. Griffiths, *Introduction to Quantum Mechanics*. Pearson Prentice Hall, 2005.

[12] G. B. Airy, "On the diffraction of an object-glass with circular aperture," *Trans. Cambridge Philosoph. Soc.*, vol. 5, pp. 283–291, 1835.

[13] S. Hunsche, M. Koch, I. Brener, and M. Nuss, "THz near-field imaging," *Opt. Commun.*, vol. 150, no. 1-6, pp. 22 – 26, 1998.

[14] E. Betzig, A. Harootunian, A. Lewis, and M. Isaacson, "Near-field diffraction by a slit: implications for superresolution microscopy," *Appl. Opt.*, vol. 25, pp. 1890–1900, Jun. 1986.

[15] F. Keilmann, "FIR microscopy," *Infrared Phys. & Technol.*, vol. 36, no. 1, pp. 217–224, 1995. Proceedings of the Sixth International Conference on Infrared Physics.

[16] H. A. Bethe, "Theory of diffraction by small holes," *Phys. Rev.*, vol. 66, pp. 163–182, Oct. 1944.

[17] T. W. Ebbesen, H. J. Lezec, H. F. Ghaemi, T. Thio, and P. A. Wolff, "Extraordinary optical transmission through sub-wavelength hole arrays," *Nature*, vol. 391, pp. 667–669, 1998.

[18] A. D. William L. Barnes and T. W. Ebbesen, "Surface plasmon subwavelength optics," *Nature*, vol. 424, pp. 824–830, 2003.

[19] Y. Fu and X. Zhou, "Plasmonic lenses: a review," *Plasmonics*, vol. 5, no. 3, pp. 287–310, 2010.

[20] T. Thio, K. M. Pellerin, R. A. Linke, H. J. Lezec, and T. W. Ebbesen, "Enhanced light transmission through a single subwavelength aperture," *Opt. Lett.*, vol. 26, pp. 1972–1974, Dec. 2001.

[21] T. Thio, H. J. Lezec, T. W. Ebbesen, K. M. Pellerin, G. D. Lewen, A. Nahata, and R. A. Linke, "Giant optical transmission of sub-wavelength apertures: physics and applications," *Nanotechnology*, vol. 13, no. 3, p. 429, 2002.

[22] A. Degiron and T. Ebbesen, "Analysis of the transmission process through single apertures surrounded by periodic corrugations," *Opt. Express*, vol. 12, pp. 3694–3700, Aug. 2004.

[23] H. Caglayan, I. Bulu, and E. Ozbay, "Beaming of electromagnetic waves emitted through a subwavelength annular aperture," *J. Opt. Soc. Am. B*, vol. 23, pp. 419–422, Mar. 2006.

[24] F. Hao, R. Wang, and J. Wang, "A design method for a micron-focusing plasmonic lens based on phase modulation," *Plasmonics*, vol. 5, no. 4, pp. 405–409, 2010.

[25] H. Bennett, "DVD-ROM And CD-R," *Emedia Professional*, vol. 11, no. 3, p. 56, 1998.

[26] N. Singla and J. O'Sullivan, "Influence of pit-shape variation on the decoding performance for two-dimensional optical storage (TwoDOS)," in *IEEE 62nd Int. Conf. on Commun.*, vol. 7, pp. 3185–3190, June 2006.

[27] C. Genet and T. W. Ebbesen, "Light in tiny holes," *Nature*, vol. 445, pp. 39–46, Jan. 2007.

[28] K. Pellerin, H. Lezec, T. Ebbesen, R. Linke, and T. Thio, "Giant optical transmission of subwavelength apertures for NSOM and data storage," in *Proc. of the 1st IEEE Conf. on Nanotechnology*, pp. 293–298, 2001.

[29] M. Mansuripur, A. R. Zakharian, A. Lesuffleur, S.-H. Oh, R. J. Jones, N. C. Lindquist, H. Im, A. Kobyakov, and J. V. Moloney, "Plasmonic nano-structures for optical data storage," *Opt. Express*, vol. 17, pp. 14001–14014, Aug. 2009.

[30] K. Ishihara, G. ichi Hatakoshi, T. Ikari, H. Minamide, H. Ito, and K. Ohashi, "Terahertz wave enhanced transmission through a single subwavelength aperture with periodic surface structures," *Jpn. J. Appl. Phys.*, vol. 44, pp. L1005–L1007, 2005.

[31] K. Ishihara, K. Ohashi, T. Ikari, H. Minamide, H. Yokoyama, J.-i. Shikata, and H. Ito, "Terahertz-wave near-field imaging with subwavelength resolution using surface-wave-assisted bow-tie aperture," *Appl. Phys. Lett.*, vol. 89, no. 20, p. 201120, 2006.

[32] A. Agrawal, H. Cao, and A. Nahata, "Time-domain analysis of enhanced transmission through a single subwavelength aperture," *Opt. Express*, vol. 13, pp. 3535–3542, May 2005.

[33] M. J. Lockyear, A. P. Hibbins, J. R. Sambles, and C. R. Lawrence, "Enhanced microwave transmission through a single subwavelength aperture surrounded by concentric grooves," *J. Opt. A*, vol. 7, no. 2, p. S152, 2005.

[34] A. Baragwanath, J. Freeman, A. Gallant, J. Zeitler, H. Beere, D. Ritchie, and M. Chamberlain, "Plasmonic apertures for THz QCL near-field imaging," in *35th Int. Conf. on Infrared Millimeter and Terahertz Waves*, pp. 1 –2, Sept. 2010.

[35] H. Caglayan, I. Bulu, and E. Ozbay, "Extraordinary grating-coupled microwave transmission through a subwavelength annular aperture," *Opt. Express*, vol. 13, pp. 1666–1671, Mar. 2005.

[36] K. Y. Park, C. Meierbachtol, N. Wiwatcharagoses, and P. Chahal, "Surface plasmon-assisted terahertz imaging array," in *IEEE Electron. Componen. and Technol. Conf.*, pp. 1846–1851, May 2012.

[37] C. S. Meierbachtol and P. Chahal, "A novel subwavelength microbolometer for terahertz sensing," *Int. J. of High Speed Electron. and Syst.*, vol. 20, no. 03, pp. 611–619, 2011.

[38] C.-M. Chiu, H.-W. Chen, Y.-R. Huang, Y.-J. Hwang, W.-J. Lee, H.-Y. Huang, and C.-K. Sun, "All-terahertz fiber-scanning near-field microscopy," *Opt. Lett.*, vol. 34, pp. 1084–1086, Apr. 2009.

[39] H. Chen, W.-J. Lee, H.-Y. Huang, C.-M. Chiu, Y.-F. Tsai, T.-F. Tseng, J.-T. Lu, W.-L. Lai, and C.-K. Sun, "Performance of THz fiber-scanning near-field microscopy to diagnose breast tumors," *Opt. Express*, vol. 19, pp. 19523–19531, Sep. 2011.

[40] S. Freeman, J. C. Sharp, and M. Harrington, *Biological Science*. Pearson Benjamin Cummings, 2011.

[41] H. Richter, A. D. Semenov, S. G. Pavlov, L. Mahler, A. Tredicucci, H. E. Beere, D. A. Ritchie, K. S. Il'in, M. Siegel, and H.-W. Hübers, "Terahertz heterodyne receiver with quantum cascade laser and hot electron bolometer mixer in a pulse tube cooler," *Appl. Phys. Lett.*, vol. 93, no. 14, 2008.

[42] B. S. Spectroscopy, "Blue Sky Spectroscopy Inc. - Custom Far-IR/THz Instrumentation and Fourier Transform Spectrometers." `http://blueskyspectroscopy.com/`, Nov. 2014.

[43] R. Golsteyn, "Cancer Cell Laboratory." `http://people.uleth.ca/~roy.golsteyn/`, Oct. 2014.

[44] J. F. Dunn, "Experimental Imaging Centre." `http://www.ucalgary.ca/eic/jeff_bio/`, Oct. 2014.

[45] E. C. L. Ru and P. G. Etchegoin, *Principles of Surface-Enhanced Raman Spectroscopy*. Elsevier, 2009.

[46] D. A. Fleisch, *A Student's Guide to Maxwell's equations*. Cambridge University Press, 2008.

[47] D. J. Griffiths, *Introduction to Electrodynamics*. Prentice Hall, 1999.

[48] J.-M. Lourtioz, H. Benisty, V. Berger, J.-M. Gerard, D. Maystre, and A. Tchelnokov, *Photonic Crystals: Towards Nanoscale Photonic Devices*. Springer, 2008.

[49] N. W. Ashcroft and N. D. Mermin, *Solid State Physics*. Holt, Rinehart and Winston, 1976.

[50] S. A. Maier, *Plasmonics: Fundamentals and Applications*. Springer, 2007.

[51] P. B. Johnson and R. W. Christy, "Optical constants of the noble metals," *Phys. Rev. B*, vol. 6, pp. 4370–4379, Dec. 1972.

[52] Lumerical, "Reference Guide for FDTD Solutions." `http://www.lumerical.com/fdtd/`, Nov. 2014.

[53] D. Saeedkia, *Handbook of Terahertz Technology for Imaging, Sensing and Communications*. WP Woodhead Publishing, 2013.

[54] A. K. Azad and W. Zhang, "Resonant terahertz transmission in subwavelength metallic hole arrays of sub-skin-depth thickness," *Opt. Lett.*, vol. 30, pp. 2945–2947, Nov. 2005.

[55] R. Singh, A. K. Azad, J. F. O'Hara, A. J. Taylor, and W. Zhang, "Effect of metal permittivity on resonant properties of terahertz metamaterials," *Opt. Lett.*, vol. 33, pp. 1506–1508, Jul. 2008.

[56] J. Gómez Rivas and A. Berrier, "Terahertz plasmonics with semiconductor surfaces and antennas," in *Asia Pacific Microwave Conf.*, pp. 1293–1296, Dec. 2009.

[57] D. Sarid and W. A. Challener, *Modern Introduction to Surface Plasmons*. Cambridge University Press, 2010.

[58] H. Raether, *Surface Plasmons on Smooth and Rough Surfaces and on Gratings*. Springer Berlin Heidelberg, 1988.

[59] J. M. Pitarke, V. M. Silkin, E. V. Chulkov, and P. M. Echenique, "Theory of surface plasmons and surface-plasmon polaritons," *Rep. Prog. Phys.*, vol. 70, pp. 1–87, 2007.

[60] J. Homola and M. Piliarik, "Surface plasmon resonance (SPR) sensors," in *Surface Plasmon Resonance Based Sensors* (J. Homola, ed.), vol. 4 of *Springer Series on Chemical Sensors and Biosensors*, pp. 45–67, Springer Berlin Heidelberg, 2006.

[61] W. Knoll, "Interfaces and thin films as seen by bound electromagnetic waves," *Annu. Rev. Phys. Chem.*, vol. 49, pp. 569–638, 1998.

[62] B. Lee, S. Kim, H. Kim, and Y. Lim, "The use of plasmonics in light beaming and focusing," *Prog. in Quant. Electron.*, vol. 34, pp. 47–87, 2010.

[63] J. Weiner, "The physics of light transmission through subwavelength apertures and aperture arrays," *Rep. Prog. Phys.*, vol. 72, p. 064401, 2009.

[64] M. Dragoman and D. Dragoman, "Plasmonics: Applications to nanoscale terahertz and optical devices," *Prog. in Quant. Electron.*, vol. 32, pp. 1–41, Jan. 2008.

[65] F. M. Grimaldi, *Physico-Mathesis De Lumine, Coloribus, Et Iride, Aliisque Annexis*. 1665.

[66] R. Wannemacher, "Plasmon-supported transmission of light through nanometric holes in metallic thin films," *Opt. Commun.*, vol. 195, pp. 107 – 118, 2001.

[67] F. G. de Abajo, "Light transmission through a single cylindrical hole in a metallic film," *Opt. Express*, vol. 10, pp. 1475–1484, Dec. 2002.

[68] F. Przybilla, A. Degiron, C. Genet, T. Ebbesen, F. de Léon-Pérez, J. Bravo-Abad, F. J. García-Vidal, and L. Martín-Moreno, "Efficiency and finite size effects in enhanced transmission through subwavelength apertures," *Opt. Express*, vol. 16, pp. 9571–9579, Jun. 2008.

[69] J. D. Jackson, *Classical Electrodynamics*. Wiley, 1962.

[70] C. J. Bouwkamp, "On Bethes theory of diffraction by small holes," *Philips Res. Rep.*, vol. 5, no. 5, pp. 321–332, 1950.

[71] B. E. A. Saleh and M. C. Teich, *Fundamentals of Photonics*. Wiley-Interscience, 2 ed., 2007.

[72] J. D. Kraus and K. R. Carver, *Electromagnetics*. McGraw-Hill, 2 ed., 1973.

[73] A. Roberts, "Electromagnetic theory of diffraction by a circular aperture in a thick, perfectly conducting screen," *J. Opt. Soc. Am. A*, vol. 4, pp. 1970–1983, Oct. 1987.

[74] F. J. Garcia-Vidal, L. Martin-Moreno, T. W. Ebbesen, and L. Kuipers, "Light passing through subwavelength apertures," *Rev. Mod. Phys.*, vol. 82, pp. 729–787, Mar. 2010.

[75] J.-M. Yi, A. Cuche, F. de Leon-Perez, A. Degiron, E. Laux, E. Devaux, C. Genet, J. Alegret, L. Martin-Moreno, and T. W. Ebbesen, "Diffraction regimes of single holes," *Phys. Rev. Lett.*, vol. 109, p. 023901, Jul. 2012.

[76] Y. Takakura, "Optical resonance in a narrow slit in a thick metallic screen," *Phys. Rev. Lett.*, vol. 86, pp. 5601–5603, Jun. 2001.

[77] F. Yang and J. R. Sambles, "Resonant transmission of microwaves through a narrow metallic slit," *Phys. Rev. Lett.*, vol. 89, p. 063901, Jul. 2002.

[78] B. Hou, J. Mei, M. Ke, W. Wen, Z. Liu, J. Shi, and P. Sheng, "Tuning Fabry-Perot resonances via diffraction evanescent waves," *Phys. Rev. B*, vol. 76, p. 054303, Aug. 2007.

[79] H. F. Ghaemi, T. Thio, D. E. Grupp, T. W. Ebbesen, and H. J. Lezec, "Surface plasmons enhance optical transmission through subwavelength holes," *Phys. Rev. B*, vol. 58, pp. 6779–6782, Sep. 1998.

[80] D. E. Grupp, H. J. Lezec, T. Thio, and T. W. Ebbesen, "Beyond the Bethe limit: tunable enhanced light transmission through a single sub-wavelength aperture," *Adv. Mater.*, vol. 11, no. 10, pp. 860–862, 1999.

[81] L. Martín-Moreno, F. J. García-Vidal, H. J. Lezec, K. M. Pellerin, T. Thio, J. B. Pendry, and T. W. Ebbesen, "Theory of extraordinary optical transmission through subwavelength hole arrays," *Phys. Rev. Lett.*, vol. 86, pp. 1114–1117, Feb. 2001.

[82] J. Wang and W. Zhou, "An annular plasmonic lens under illumination of circularly polarized light," *Plasmonics*, vol. 4, pp. 231–235, Sep. 2009.

[83] F. J. García-Vidal, L. Martín-Moreno, H. J. Lezec, and T. W. Ebbesen, "Focusing light with a single subwavelength aperture flanked by surface corrugations," *Appl. Phys. Lett.*, vol. 83, no. 22, pp. 4500–4502, 2003.

[84] J. Wang and W. Zhou, "Subwavelength beaming using depth-tuned annular nanostructures," *J. Modern Opt.*, vol. 56, pp. 919–926, Apr. 2009.

[85] A. Giannattasio, I. R. Hooper, and W. L. Barnes, "Dependence on surface profile in grating-assisted coupling of light to surface plasmon-polaritons," *Opt. Commun.*, vol. 261, no. 2, pp. 291 – 295, 2006.

[86] G. Lávâque and O. J. F. Martin, "Optimization of finite diffraction gratings for the excitation of surface plasmons," *J. Appl. Phys.*, vol. 100, no. 12, pp. –, 2006.

[87] F. Villate-Guío, F. López-Tejeira, F. J. García-Vidal, L. Martín-Moreno, and F. de León-Pérez, "Optimal light harvesting structures at optical and infrared frequencies," *Opt. Express*, vol. 20, pp. 25441–25453, Nov. 2012.

[88] O. Mahboub, S. C. Palacios, C. Genet, F. J. Garcia-Vidal, S. G. Rodrigo, L. Martin-Moreno, and T. W. Ebbesen, "Optimization of bull's eye structures for transmission enhancement," *Opt. Express*, vol. 18, pp. 11292–11299, May 2010.

[89] S. Kim, Y. Lim, H. Kim, J. Park, and B. Lee, "Optical beam focusing by a single subwavelength metal slit surrounded by chirped dielectric surface gratings," *Appl. Phys. Lett.*, vol. 92, no. 1, pp. 1–3, 2008.

[90] B. Jia, H. Shi, J. Li, Y. Fu, C. Du, and M. Gu, "Near-field visualization of focal depth modulation by step corrugated plasmonic slits," *Appl. Phys. Lett.*, vol. 94, no. 15, 2009.

[91] R. G. Mote, W. Zhou, and Y. Fu, "Beaming of light through depth-tuned plasmonic nanostructures," *Optik*, vol. 121, pp. 1962–1965, Nov. 2010.

[92] H. Shi, C. Du, and X. Luo, "Focal length modulation based on a metallic slit surrounded with grooves in curved depths," *Appl. Phys. Lett.*, vol. 91, no. 9, pp. –, 2007.

[93] F. Hao, R. Wang, and J. Wang, "A novel design method of focusing-control device by modulating SPPs Scattering," *Plasmonics*, vol. 5, no. 1, pp. 45–49, 2010.

[94] X. Zhou, W. Zhong, Y. Fu, and C. Hu, "Tailoring focal length of plasmonic lenses by phase modulation of emitted light," *J. Comput. Theor. Nanos.*, vol. 8, no. 7, pp. 1242–1246, 2011.

[95] "NRC Automotive and Surface Transportation." `http://www.nrc-cnrc.gc.ca/eng/rd/ast/index.html`, Nov. 2014.

[96] "Virginia Diodes." `http://vadiodes.com/`, Oct. 2014.

[97] K.-E. Peiponen, J. A. Zeitler, and M. Kuwata-Gonokami, *Terahertz Spectroscopy and Imaging*. Springer, 2013.

[98] J. F. Johansson and N. D. Whyborn, "The diagonal horn as a sub-millimeter wave antenna," *IEEE Trans. on Microw. Theory and Techn.*, vol. 40, pp. 63–81, May 1991.

[99] "Newport Corporation." `http://www.newport.com/`, Oct. 2014.

[100] R. M. Malone, S. A. Becker, D. H. Dolan, R. G. Hacking, R. J. Hickman, M. I. Kaufman, G. D. Stevens, and W. D. Turley, "Design of a thermal imaging diagnostic using 90-degree off-axis parabolic mirrors," *Proc. SPIE*, vol. 6288, pp. 62880Z–62880Z–9, 2006.

[101] "Stanford Research Systems." `http://www.thinksrs.com/`, Apr. 2014.

[102] "Tektronix Test and Measurement Equipment." http://www.tek.com/, Apr. 2014.

[103] "Data Translation." http://www.datatranslation.com/, Nov. 2014.

[104] "Exelis Visual Information Solutions." http://www.exelisvis.com/ProductsServices/IDL.aspx, Nov. 2014.

[105] "Edmund Optics." http://www.edmundoptics.com/, Oct. 2014.

[106] "ImageJ." http://imagej.nih.gov/ij/, Apr. 2014.

[107] "IUPAC Gold Book: The Beer-Lambert Law." http://goldbook.iupac.org/B00626.html, Nov. 2014.